GEOLOGY OF THE INTERMOUNTAIN WEST
an open-access journal of the Utah Geological Association
ISSN 2380-7601

Volume 13 ***2026***

STRUCTURAL AND STRATIGRAPHIC CONTROLS ON THE DIAGENETIC EVOLUTION OF THE CRETACEOUS BASELINE SANDSTONE, SOUTHERN NEVADA, U.S.A.

Casey J. Duncan and Marjorie A. Chan

GEOLOGY OF THE INTERMOUNTAIN WEST

an open-access journal of the Utah Geological Association

ISSN 2380-7601

Volume 13 ***2026***

Editors

Production

Cover Design and Desktop Publishing
Douglas A. Sprinkel

Cover

Views of the coloration facies of the white and red sandstone members of the Baseline Sandstone in the Muddy Mountains area, Nevada. Top left: purple coloration patterns found along soft-sediment deformation surfaces in the lower red sandstone member. Top right: intensely concentrated red and purple coloration in the red sandstone member. Bottom: outcrop panorama showing the range in coloration of the white sandstone member and its typical diffuse expressions (scale bar indicates stratigraphic thicknesses of lowest beds).

2025–2026 UGA Board

President	Rob Buehring	robbuehring@yahoo.com	713.412.9269
President-Elect	Trae Boman	traebgeologist@gmail.com	801.648.5206
Program Chair	Mike Arnoff	marnoff@utah.gov	385.303.0431
Treasurer	Will Hurlbut	wdhurlbut@gmail.com	860.733.3190
Secretary	Kylie Arcaris	kaarcaris@gmail.com	801.628.6731
Past President	Keilee Higgs	keileeann@utah.gov	801.678.3683

UGA Committees

Environmental Affairs	Seeking a Volunteer		
Geologic Road Sign	Greg Gavin	greggavin@gmail.com	513.509.1509
Historian	Paul Anderson	paul@pbageo.com	801.364.6613
Outreach	Greg Nielsen	gnielsen@weber.edu	801.626.6394
Public Education	Zach Anderson	zanderson@utah.gov	801.537.3300
	Matt Affolter	gfl247@yahoo.com	
Publications	Paul Inkenbrandt	paulinkenbrandt@utah.gov	801.537.3361
Publicity	Paul Inkenbrandt	paulinkenbrandt@utah.gov	801.537.3361
Social/Recreation	Roger Bon	rogerbon@xmission.com	801.580.1331

AAPG House of Delegates

2023–2026 Term	David A. Wavrek	dwavrek@petroleumsystems.com	801.322.2915

State Mapping Advisory Committee

UGA Representative	Bill Loughlin	bill@loughlinwater.com	435.649.4005

Earthquake Safety Committee

Chair	Seeking a Volunteer		

UGA Website — www.utahgeology.org

Webmaster	Paul Inkenbrandt	paulinkenbrandt@utah.gov	801.537.3361

Scholarship Golf Tournament

Co-Chair	Rick Ford	rford@weber.edu	801.915.3188
Co-Chair	John South	jsouth@utah.gov	385.266.2113

UGA Newsletter

Newsletter Editor	Mike Barber	uga.newsletter@gmail.com	435.640.1382

Become a member of the UGA to help support the work of the Association and receive notices for monthly meetings, annual field conferences, and new publications. Annual membership is $30 and annual student membership is only $5. Visit the UGA website at www.utahgeology.org for information and membership application.

The UGA board is elected annually by a voting process through UGA members. However, the UGA is a volunteer-driven organization, and we welcome your voluntary service. If you would like to participate please contact the current president or committee member corresponding with the area in which you would like to volunteer.

Utah Geological Association formed in 1970 from a merger of the Utah Geological Society, founded in 1946, and the Intermountain Association of Geologists, founded in 1949. Affiliated with the American Association of Petroleum Geologists.

GEOLOGY OF THE INTERMOUNTAIN WEST
an open-access journal of the Utah Geological Association
Volume 13 ***2026***

Structural and Stratigraphic Controls on the Diagenetic Evolution of the Cretaceous Baseline Sandstone, Southern Nevada, U.S.A.

Casey J. Duncan[1] and Marjorie A. Chan[2]
[1]Independent, Cortez, CO 81321 USA; casey.j.duncan@gmail.com
[2]Department of Geology and Geophysics, University of Utah, Salt Lake City, UT 84112 USA; marjorie.chan@utah.edu

ABSTRACT

The Cretaceous Baseline Sandstone of southern Nevada is an alluvial to fluvial continental siliciclastic deposit formed in response to activity of the Summit-Willow Tank thrust. An integrated multi-scale and multi-method approach was used to characterize the diagenetic mineralogy of the formation, including traditional field mapping and description; Landsat multispectral mineral mapping; in situ reflectance spectroscopy; thin section petrography; clay fraction x-ray diffraction, x-ray fluorescence, and inductively coupled plasma mass spectrometry; and (U-Th)/He geochronology. The formation contains a wide array of iron oxide-dominant diagenetic features grouped as coloration and cementation facies. Coloration varies in hue (stark white, white/tan/gray, yellow/yellow-brown to brown, red, and purple), expression (diffuse/pastel, intense, variegated), and intensity (e.g., light to deep), which relate primarily to crystal size, mineralogy, and abundance of iron oxide grain coats (goethite vs hematite) and cement. Cementation facies vary in mineralogy with iron oxide generally prevalent, and carbonate abundant only in the upper red sandstone member. Rare silica-replaced fragments of the tree fern *Tempskya*(?) occur in the upper white sandstone to lower red sandstone members. Iron oxide cementation facies consist of ironstone horizon and concretionary types, which vary widely in size and morphology.

Integration of data across spatial scales indicates that coloration and iron oxide cementation patterns formed within three diagenetic stages. The eogenetic stage was influenced by surface processes related to the depositional environment along with basin-scale fluid flow from the Sevier orogeny. The mesogenetic stage followed by additional remobilization of iron during shallow to moderate burial. A late phase of telogenetic fluid flow, likely of meteoric infiltration origin, resulted in intense localized alteration along the Miocene-aged Baseline fault with latest-stage carbonate mineralization occurring along joints and as pendant cements.

INTRODUCTION

Continental siliciclastic deposits provide opportunities to examine diagenetic attributes indicative of past fluid flow episodes and determine controls on paragenetic evolution, including their relation to sedimentary textures, fabrics, and structural features. To unravel such complex diagenetic tales, the integration of data sets across spatial scales is often required. Traditional field methods provide a 'ground-truth' view of the rocks, although they can be time consuming and inadequate to objectively document diagenetic patterns due to inac-

Citation for this article.
Duncan, C.J., and Chan, M.A., 2026, Structural and stratigraphic controls on the diagenetic evolution of the Cretaceous Baseline Sandstone, southern Nevada, U.S.A.: Geology of the Intermountain West, v. 13, p. 53–94, 1 appendix, https://doi.org/10.31711/giw.v13.pp53-94.

cessibility or ruggedness of the field area. Conversely, remote sensing methods, such as multispectral and hyperspectral imaging, are very useful for objectively mapping diagenetic mineral patterns but are limited by surface rock exposure and input data constraints, among others. Laboratory analyses, while very powerful, also require full contextual information to be of most use. This study focuses on the distribution and relations of diagenetic attributes of the Cretaceous (Albian-Cenomanian) Baseline Sandstone (a well-exposed foreland basin deposit in southeastern Nevada), through the integration of traditional field methods with remote sensing data and laboratory analyses, to bridge the gaps in scale and uncertainties to decipher the formation's complex diagenetic history. This integrated research attempts to answer the following questions:

1. What diagenetic mineral products are preserved in the Baseline Sandstone and how are those products distributed spatially and stratigraphically?

2. To what extent did structural features and stratigraphic architecture, along with the distribution of deposited lithologies/textural heterogeneities, influence fluid flow and diagenetic evolution?

3. What eogenetic, mesogenetic, and telogenetic stages are represented by the diagenetic products, and how can that paragenetic framework inform the timing and drivers of basin-scale fluid flow processes?

The large variety of diagenetic mineral products observed within the Baseline Sandstone presents an opportunity to explore controls on diagenesis, and how the diagenetic evolution relates to the regional depositional and structural history.

FIELD AREA AND GEOLOGIC SETTING

The Baseline Sandstone is exposed in southern Nevada, U.S.A., about 70 km northeast of Las Vegas, Nevada, adjacent to and within Valley of Fire State Park and near the Overton Arm of Lake Mead (Figure 1A). Regionally, the stratigraphy of the field area relates to the long evolution of the western margin of North America from breakup of Rodinia (Li et al., 2008), through passive continental margin sedimentation of the miogeocline (Crafford, 2008), to exotic terrane accretion and formation of multiple fold and thrust belts and resultant foreland basins (Crafford, 2007, 2008), to sedimentation contemporaneous with large-magnitude extension in the Basin and Range Province (Bohannon, 1984; Lamb et al., 2018). Locally, Upper Paleozoic to Mesozoic sedimentary rocks present in the autochthonous Sevier orogenic thrust sheets (Bohannon, 1992) were weathered and eroded during uplift and unroofing (Aschoff and Schmitt, 2008; McNamara, 2010). These sedimentary units include Upper Paleozoic carbonate to clastic units (Pennsylvanian Bird Spring Formation, Permian Pakoon Limestone, Permian red beds, and Permian Kaibab/Toroweap Formations) and Triassic to Lower Jurassic tidal, fluvial, to eolian clastic units (Moenkopi, Chinle, Moenave/Kayenta, and Aztec Formations; see stratigraphic column on Figure 1B; Bohannon, 1992; Beard et al., 2007; Muntean, 2013). Cretaceous units comprise the foreland basin sediments deposited concomitant with Sevier thrusting (including the Willow Tank Formation and Baseline Sandstone) and are capped along an unconformity by pre- and syn-extensional deposits of the Upper Oligocene-Lower Miocene Rainbow Gardens Member of the Horse Spring Formation and younger deposits (Bohannon, 1983, 1984; Lamb et al., 2018).

The Baseline Sandstone is a about 1-km-thick alluvial and fluvial fan to fluvial siliciclastic unit that was deposited along the easternmost edge of the Sevier fold and thrust belt contemporaneous with active thrusting along the Muddy Mountains and Summit-Willow Tank thrusts (Longwell, 1949; Bohannon, 1983; Carpenter, 1989; Aschoff and Schmitt, 2008; McNamara, 2010). Locally, the Baseline Sandstone is composed of three informal members and one formal member. They are, in ascending stratigraphic order, the basal conglomerate, the white sandstone, and the coeval/interfingering red sandstone members, and the capping Overton Conglomerate Member (Bohannon, 1983; Beard et al., 2007).The basal conglomerate is not present in the field area, and the Overton Conglomerate occurs only in the north side of the field area, therefore only the white

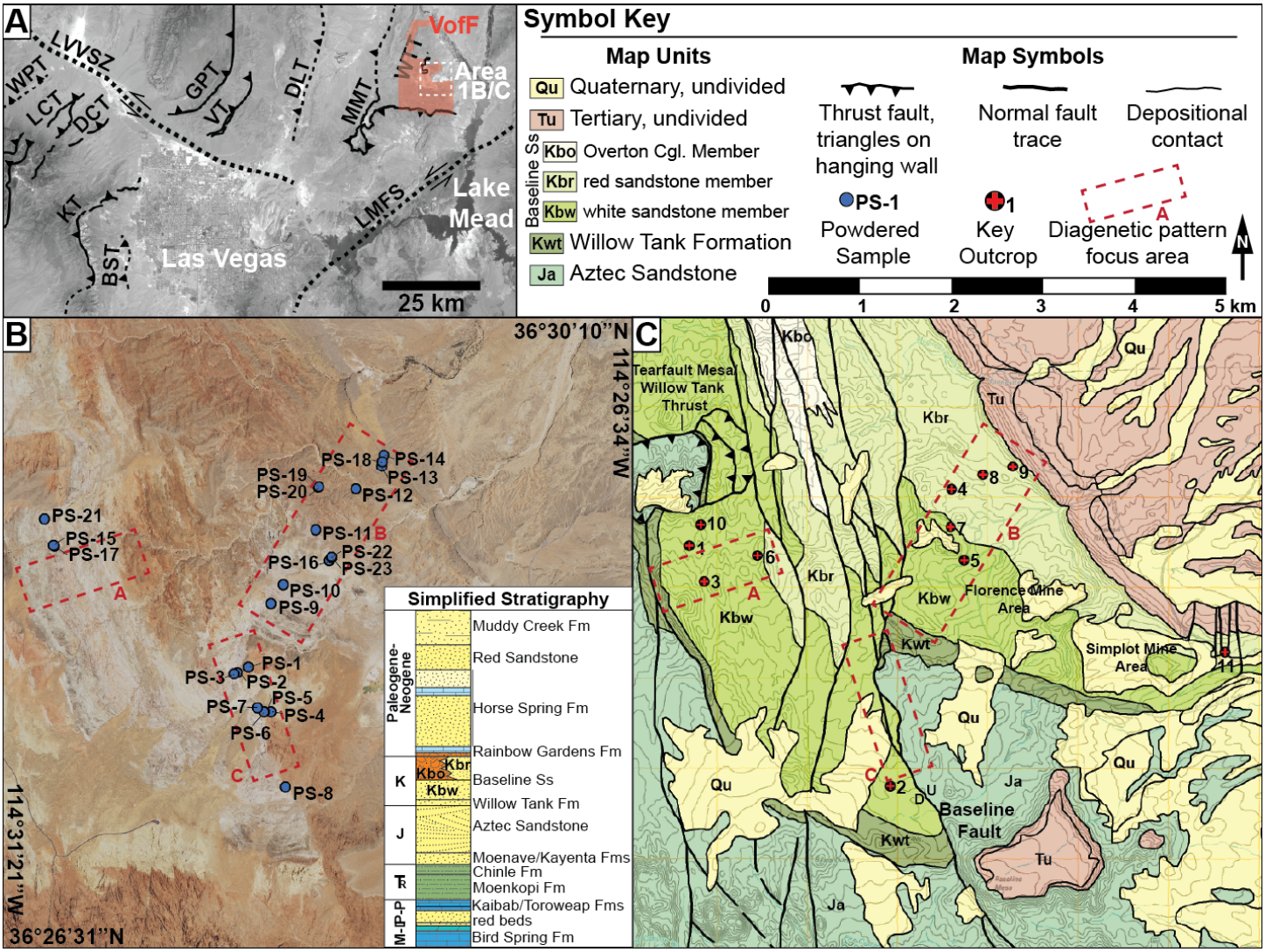

Figure 1. Regional and geological context of the Baseline Sandstone. (A) Satellite image with major structural features surrounding Las Vegas, Nevada. Thrusts: WPT = Wheeler Pass thrust, LCT = Lee Canyon thrust, DCT = Deer Creek thrust, KT = Keystone thrust, BST = Bird Springs thrust, GPT = Gass Peak thrust, VT = Valley thrust and Valley anticline, DLT = Dry Lake thrust, MMT = Muddy Mountain thrust, WTT = Willow Tank thrust, LVVSZ = Las Vegas Valley Shear Zone, LMFS = Lake Mead fault system (data from Bohannon, 1992; Page et al., 2005; Aschoff and Schmitt, 2008; Felger and Beard, 2010); VofF = Valley of Fire State Park approximate area. Background image from Landsat 8 Scene LC08_L1TP_039035_20170526_20170615_01_T1_B3, courtesy of the U.S. Geological Survey. (B) Composite NAIP image of the field area and Valley of Fire State Park area, with the sample locations of powders subject to laboratory analyses and simplified regional stratigraphic column with data from Bohannon (1983, 1984), Bohannon et al. (1993), Beard et al. (2007), Dickinson et al. (2014), Lamb et al. (2015); abbreviations are same as in symbol key at top. (C) Simplified geologic map of the field area showing the locations of diagenetic pattern focus areas and key outcrops examined for this study, D = downdropped and U = upthrown blocks of the Baseline fault (data from Bohannon, 1983, 1992; Beard et al., 2007; Muntean, 2013).

sandstone and red sandstone members were encountered in the focus areas A, B, and C within the field area (red dotted boxes in Figures 1B and 1C).

The Baseline Sandstone was deposited in the foredeep then wedge-top depozones (Bohannon, 1983; Roddaz et al., 2010; DeCelles, 2012) as the fold and thrust belt migrated eastward. The Willow Tank Formation lies unconformably atop the Jurassic Aztec Sandstone, a thick eolianite unit that is thought to be roughly correlative to the Navajo and Nugget Sandstones that extend eastward through Utah and into eastern Idaho/western Wyoming (Fillmore, 2011). The striking coloration changes of the Aztec, and which give the Valley of Fire its characteristic multi-colored hues, were formed by basinal fluid flow contemporaneous with, and causally related to, thrust activity and thickening of the fold and thrust belt (Eichhubl et al., 2004).

Deposition of the Baseline Sandstone ceased about 90 Ma (Carpenter, 1989) and the area remained either a zone of sediment bypass, or non-deposition until the early Neogene Period (Eichhubl et al., 2004). Regionally, Laramide orogenic activity folded and tilted the deposits in the area during the formation of the Kingman arch in the Tertiary (Lamb et al., 2015). The deposits of the Baseline in the field area may have been affected by this deformation, as evidenced by the change of strike of the formation toward the southeast, but large uncertainties remain. Basin and Range extensional tectonics initiated about 18 to 15 Ma (Wernicke et al., 1988; Lamb et al., 2015) and resulted in further tilting/rotation of the foreland basin deposits along north-south-trending normal faults. These normal faults provided additional conduits for fluid flow, and in some cases resulted in solution collapse and dissolution of carbonate rocks such as in the nearby Mormon Mountains and Tule Springs Hills (Diehl et al., 2010).

METHODS

The scale of the field area, the about 1 km stratigraphic thickness of the Baseline Sandstone, and a wide diversity in observed diagenetic mineral products, necessitated a multi-scale and multi-method approach. A combination of field-, remote sensing-, and laboratory-based analyses were used to document the range in diagenetic product types and morphology, their geochemical attributes, overall distribution, and any crosscutting relations with structural and stratigraphic features. Generalized descriptions of methods are provided below, and additional details are provided in the Appendix.

In situ field characterization of diagenetic mineral products involved categorization and characterization of diagenetic mineral types, morphologies, and geometries. Characterization was focused in three areas, A, B, and C of Figure 1C, that each are roughly about 0.5 to 1 km by about 1.5 to 2.5 km in width/length. The stratigraphic distribution of diagenetic minerals was described and interpreted from formation- to bed-scales along stratigraphic transects in two focus areas (A and B of Figure 1C). Diagenetic mineral distribution was explored in association with Miocene normal faults in focus area C (Figure 1C). A portable reflectance spectrometer was used to measure reflectance spectra of samples throughout the field area in the 350 to 2500 nm wavelength range to determine diagenetic mineralogy, principally to differentiate the iron oxide phases and identify clay minerals present, and further inform their stratigraphic and spatial distribution. Each spectroscopic measurement included location, lithofacies context, diagenetic coloration or cementation context, and photographs.

A Landsat 8 OLI/TIRS multispectral scene was processed in ENVI and ArcGIS to visualize the diagenetic, mineral occurrence more objectively, and stratigraphic distribution through surface reflectance mapping (Sabins, 1999; Knepper, 2010; Pour and Hashim, 2015; Ducart et al., 2016). Band ratios were calculated and thresholded using ENVI to map the distribution of specific diagenetic mineralogy and identify the band ratios most useful for image compositing. We used the ratios 4/2 (red/blue), 5/6 (near infrared/short-wave infrared 1), and 6/7 (short-wave infrared 1/short-wave infrared 2) for subsequent compositing and classification (see Appendix, Table A2; see Roy et al. [2014] for Landsat band designations). Band ratio composite images were first masked for pixels containing vegetation, water, or shadows, then classified in ArcMap. Classification was done using a supervised classification based on nine principal training classes and unsupervised classification with twelve classes.

We used six laboratory methods to further analyze representative field samples. First, transmitted- and reflected-light thin section petrography (general observations for 104 thin sections, detailed characterization of 9 thin sections) to characterize grain/pore-scale attributes of framework grains, authigenic grain coats and cements, and micro-crosscutting relations and geometries. Second, reflectance spectroscopy on fresh and weathered rock surfaces allowed the identification of iron oxide, carbonate, and clay minerals (for a total of 787 spectral profiles between field and laboratory samples). Third, scanning electron microscope (SEM) imaging of 21 samples for characterization of micron-scale mineralogical attributes. Fourth, we examined 23 ground/powdered samples with x-ray fluorescence (XRF) analysis, 20 of which were analyzed using inductively coupled plasma mass spectrometry (ICP-MS), all to explore bulk chemical attributes focusing on redox sensitive elements. Fifth, we identified clay minerals and clay-sized minerals using x-ray diffraction (XRD) in 11 of the powdered samples. Sixth, we analyzed five iron oxide-cemented samples for (U-Th)/He ratios to provide absolute age-dating of the iron oxide cements. Detailed sample preparation steps and instrument settings are provided in the Appendix.

RESULTS AND INTERPRETATION

Diagenetic Features

Diagenetic mineral products can be grouped in two principal diagenetic feature categories: coloration facies and cementation facies (Figure 2). These are recognized by their general color (which relates to principal mineralogy), geometry, and relations to primary depositional structures and textures. The coloration facies (Appendix, Table A1) are differentiated based on variation in overall color hue (e.g., red, yellow), expression (e.g., solid, concentrated, variegated, diffuse, pastel), and intensity (e.g., light to deep). This coloration categorization is based upon the Munsell color system (which uses hue, value, and chroma; see Deaton, 1987) but modified to capture the range of coloration facies observed in the field. Cementation facies (Appendix, Tables A2 through A4) form well-indurated sandstone and are further subdivided into ironstone horizon types (if laterally continuous and bedding-parallel), and concretionary types (if discrete mineral masses that crosscut depositional textures). Concretionary types occur in three principal mineralogical groups: iron oxides, carbonate, and silica. Both coloration and cementation facies are essentially on a spectrum of diagenetic mineral concentration, with no clear, definable boundary between them. Therefore, whether there was sufficient concentration of the diagenetic mineral to produce differential erosion was used as a rule in the field to differentiate between the two facies. Key attributes of the diagenetic facies are summarized below and in Tables 1 through 4, with additional detail available in the Appendix.

Coloration Facies

Coloration facies range in generalized hues from stark white, white/tan/gray, yellow/yellow-brown to brown, red, and purple, with expression varying due to iron oxide mineral concentration as solid, pastel/diffuse, or variegated/concentrated (Figures 3 through 5; see Munsell color codes in Appendix, Table A1). These facies occur on the order of decimeters to hundreds of meters vertically and laterally, depending on stratigraphic context (i.e., member, depositional environment, sedimentary heterogeneities) and proximity to structures. Coloration intensity typically changes most dramatically near the upper surfaces of beds (e.g., Figure 3B). In general, the coloration facies range from white (bleached) corresponding with very little iron oxide of about 0.05 weight percent (wt%), to deeper hues of reds reflecting more diagenetic iron oxide cement of about 0.5 wt%, with purple sandstone containing up to about 3.5 wt% based on ICP-MS results.

Reflectance spectroscopy, SEM, and thin section petrography reveal mineralogical attributes that determine coloration hue and intensity, as follows. The coloration of the yellow to yellow brown/brown facies is related to the presence of grain-coating platy goethite crystals up to about 1 μm across, with more intense coloration exhibiting isopachous grain coating goethite. Red coloration contains platy (up to about 1 μm across) to possibly rhombohedral (up to about 10 μm across) grain-coating to pore-filling hematite crystals. The

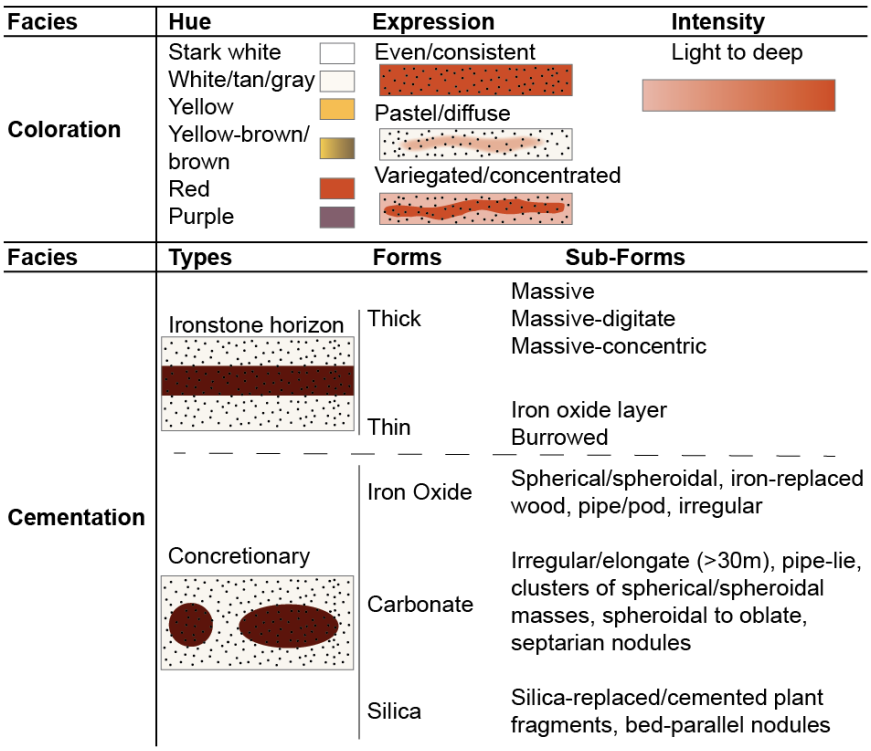

Figure 2. Diagenetic feature categorization schema used to organize the wide variety of observed diagenetic attributes of the Baseline Sandstone.

intensity of red coloration again relates to the overall concentration of the mineral, typically up to about 0.5 wt%, with more intense coloration exhibiting a greater concentration of grain-coating hematite. Purple hues, including dusky gray to dark-gray purple hues, contain hematite that occurs as spherules about 5 μm in diameter. The coloration intensity is again determined by overall concentration, with the deepest colors containing the greatest concentration of the spheroids (up to about 3.5 wt% of the rock).

Cementation Facies

Ironstone horizon types are those cementation facies that are parallel to and occur along bedding or bounding surfaces (Figure 6 and Appendix, Table 2). Generally, horizons extend laterally on the meter- to decameter-scale with thicknesses up to about 10 cm. Based on typical thickness, the ironstone horizons are divided into 'thick' (greater than 5 cm) and 'thin' (less than 5 cm) forms. These forms are further subdivided based on their textural characteristics and macroscale structures into five sub-forms. The thick forms comprise the massive, massive-digitate, and massive-concentric sub-forms, and the thin forms comprise the iron oxide layer and burrowed sub-forms. Ironstone horizons are typically associated with intense coloration hues, most commonly dark yellow-brown, dark red, and purple hues. Reflectance spectra and thin section petrography indicate that the horizons typically consist of a mix of pore-filling hematite and goethite with iron oxide crystal size and morphology similar to those of the coloration facies. The iron oxide layer sub-form consists of a massive/structureless layer up to about 2 to 3 cm thick, composed almost entirely of hematite spherules (similar in size, morphology, and composition to the purple coloration facies) mixed with very few (less than 5%) sand grains.

Iron oxide concretionary forms are the most common cementation facies type throughout the field area. The range in morphology/texture includes the spherical/spheroidal, rod-like, pipe/pod, irregular, and iron-replaced fossil wood sub-forms (Figure 7 and Table 3). Concretions vary in size from mm- to dm- scale (generally less than 20 cm, Figures 7A through 7C), but exceptional spherical concretions from the middle red sandstone member range up to about 1 m in diameter (Figure 7D), and irregular concretions range up to about 2 m in length (Figure 7H). Iron oxide concretions generally exhibit dark brown-dark purple and

Table 1. Coloration facies attributes.

Hue	Munsell Color Code(s)	Preferred Hue Associations	FeO Mineralogy (phase, crystal size, relative amount)[a]	Clay Minerals[b]	Key Relative Bulk Elemental Abundances[c]
Stark White	N9	n/a	Not present	Interlayered illite/smectite, kaolinite	Generally lower abundances than other samples
White/Tan/Gray	N9, N8, 5YR8/1, 10YR8/2, 10R8/2	All other hues	Not present	Illite, kaolinite	Generally lower abundances than other samples
Yellow	2.5Y(7 to 8)/(4 to 8), 5Y6/4, 10YR(5 to 8)/(4 to 8)	White/tan/gray, yellow-brown/brown, purple	Acicular to platy goethite, up to 1 µm, low to moderate concentration as grain coats	Illite, kaolinite	Depleted in Mg, Mn, Fe, relative to red coloration
Yellow-Brown/Brown	5YR2/2, 5YR3/(3 to 4), 5YR4/(4 to 6), 10YR(4 to 6)/(4 to 8)	White/tan/gray, yellow, purple	Acicular to platy goethite, up to 1 µm, moderate concentration as isopachous grain coats ~3 µm thick	Illite, kaolinite	Depleted in Mg, Mn, Fe, relative to red coloration
Red	5R(3 to 6)/(4 to 6), 10R(5 to 6)/(4 to 6), 10R4/6, 5YR6/4, 10YR7/4	White/tan/gray, purple	Platy hematite, up to 1 µm, low to moderate concentration as grain coats	Illite, kaolinite; rare smectite	Enriched in Mn, Fe relative to yellow coloration
Purple	5P(6 to 2)/2, 5R(2.5 to 5)/(2 to 4), 10R3/4	All other hues	Hematite spherules, ~5 µm max diameter, low concentration in purple-gray to high concentration in dark purple	Illite, kaolinite; rare chlorite and alunite	Greatest abundance of Fe (up to ~3.5 wt%) of coloration

[a]Method: Thin section petrography, SEM, VNIR spectroscopy

[b]Method: Clay-fraction XRD, SEM, VNIR spectroscopy

[c]Method: ICP-MS, XRF

red-brown to red coloration on fresh (broken) internal rock faces. Reflectance spectra, thin section petrography, and SEM results show that these colors are related to the dominant mineralogy of the concretion (see Figures 8A through 8E). Iron oxides consist of mixtures of pore-filling platy hematite and acicular to platy goethite (ferrihydrite) to hematite dominant. In most cases, the pore-filling iron oxides appear to support a wide grain spacing, indicating their formation occurred early after deposition, prior to compaction.

Some iron oxide concretions from the white sandstone member preserve fossil wood grain texture or replace woody materials, possibly of unknown conifer(?) or deciduous(?) trees (Mustoe, 2018; Figures 9A and 9B). Other small spherical/spheroidal concretions contain mineralized fossil wood fragments at their core and are surrounded by concentric layering with pyrite in the center and a mixture of hematite and goethite in the outer layer with a thin layer of jarosite in between (Figure 9C).

Carbonate concretionary forms occur in various sizes and morphologies. They typically only occur in the upper parts of the red sandstone member, or the Aztec Sandstone in the footwall of the Baseline fault (Table 4). The morphology ranges from irregular/elongate subforms that are up to about 30 m in length and 2 to 3 m across found in the lower red sandstone in diagenetic focus area A (Figure 10A), pipe-like (Figure 10B), clus-

Table 2. Ironstone horizon attributes.

Type	Field Attributes			FeO Mineralogy (phase, crystal size, relative amount)[a]	Clay Minerals[b]
	Lateral Extent	Thickness	Key Structures		
Thick Form					
Massive	~75 m, possibly up to ~250 m	Up to ~10 cm	Structureless internal textures	Mixed hematite + goethite, large amount, occludes pore spaces	Kaolinite
Massive-Concentric	Up to ~25 m	Up to ~5-15 cm	Concentric interal texture	Goethite(?)	No data
Massive-Digitate	Up to ~5 m	Up to ~10 cm	Upward oriented digitate structures on top surface, ~1-5 cm tall	Pore-filling goethite in digitate structure, narrow bands of hematite in horizon	Kaolinite
Thin Form					
Iron Oxide Layer	Up to ~20 m	Iron oxide layer up to ~3 cm, dark color below layer typically 1-5 cm	Progressively darker red/purple coloration and cementation towards layer, capped by distinct layer of iron oxide with no sand content	Hematite spherules, ~5 μm diameter, makes up nearly the entire volume of the layer	Kaolinite
Burrowed	Up to ~20-25 m	Up to ~3-5 cm	Iron-cemented horizontal, single-shaft, straight to low sinuosity burrows with simple fill	Platy hematite (possible mixture with goethite)	Vermiform kaolinite

[a]Method: Thin section petrography, SEM, VNIR spectroscopy

[b]Method: SEM, VNIR spectroscopy

ters of spherical/spheroidal masses (individually up to about 5 cm in diameter) that commonly exhibit internal concentric brown coloration banding (Figure 10C) or, in the case of Aztec examples, occur as compound conjoined groupings of two to four spheres with smaller spheres (less than about 1 cm in diameter) superimposed on their outer surface (Figure 10D), spheroidal to oblate sub-forms up to about 30 cm in diameter (Figure 10E), and septarian nodules up to about 20 cm in diameter (Figure 10F). Carbonate concretions commonly exhibit solid medium to light red coloration, with some pipe-like examples containing a red exterior with a reddish-yellow interior. Silica concretionary forms occur as silica-replaced/cemented plant fragments, tentatively identified as false-trunk pieces of the tree-like fern *Tempskya*(?) (Tidwell and Hebbert, 1992), and bed-parallel nodules about 10 to 20 cm thick and up to about 2 m in lateral extent composed of silica-cemented sandstone.

Analyses of representative powdered samples (ICP-MS, XRF, and XRD; see Table A4) reveal distinct or overlapping patterns in bulk chemical and mineralogical attributes of cementation, coloration, and Baseline fault transects (BFT) sample groups. Samples exhibit the most significant enrichment of redox-sensitive elements in cementation facies and intense coloration facies (Table 5), with relative enrichment dependent on overall mineralogy and group to which the sample belongs (Figure 11). When U/Th, V/Cr, and Fe/Mn are plotted, the three sample groups plot in consistent regions within the plot area, with overlap between coloration/BFT and coloration/cementation but no overlap between BFT/cementation (Figures 11A through 11C), even when normalized to the iron abundance to account for concentration effects (Figures 11D through 11F). This likely suggests differing composition of the fluids responsible for formation of the stratigraphy-re-

Table 3. Iron oxide concretion attributes.

Type	Field Attributes		FeO Mineralogy (phase, crystal size, relative amount)[b]	Clay Minerals[c]
	Morphology and Texture	Size[a]		
Spherical/ Spheroidal	Spherical - approximately equal x-, y-, z-axis lengths; spheroidal - one axis longer than the other two, typically parallel to bedding; surface textures variable from smooth to knobbly	Commonly less than ~20 cm diameter, limited examples up to ~1 m diameter (spherical) and 2 m max axis length (spheroidal)	Mixture of pore-filling platy hematite and goethite (rare rhombohedral(?)), hematite most common with goethite dominant in concretions associate with wood fragments	Kaolinite, Illite
Iron-Replaced Wood	Exhibits woody surface texture and morphology of wood fragments; irregular where FeO extends into surrounding sandstone	Variable: 2-3 cm up to ~30 cm length, wood fragments up to ~5-10 cm width, growth into surrounding sandstone ~5 cm	Primarily acicular goethite (0.5-1 μm length, 0.05-0.1 μm width), pyrite-replaced in some spheroidal masses that is oxidized to hematite/ goethite (with other oxyhydroxides?) with intermediate jarosite(?), minor/ rare rhombohedral hematite(?)	No data
Rod Like	Cylindrical (circular to slightly oval in cross section), straight to slightly tapered, smooth-sided, occasional bulbous external growths	Broken lengths typically ~10-20 cm, diameters up to 2-3 cm	Goethite, with other oxyhydroxides	Illite
Pipe/Pod	Spheroidal to elongate/pipe-like shell that surrounds poorly cemented interior; digitate structures on interior surface oriented radially inward	Typically ~10 to ~20 cm long-axis length	Mixed oxyhydroxides, goethite, thin concentric layers of hematite; digitate structures primarilly goethite	Kaolinite(?), Illite(?)
Irregular	Irregular, nodular, all axes of unequal lengths; smooth surfaces typical	Highly variable: cm-scale where multiple smaller concretions have merged, up to ~2 m length for individual irregular nodules	Mixed oxyhydroxides(?) and goethite(?)	No data

[a]Size range/generalized scale of concretion size, not specific measurements

[b]Method: Thin section petrography, SEM, VNIR spectroscopy

[c]Method: Clay-fraction XRD, SEM, VNIR spectroscopy

[d]Method: ICP-MS, XRF

lated cementation facies versus the fault-related cementation facies. XRD shows that the most common clay minerals are kaolinite and illite (Table 6), with chlorite and alunite present in stratigraphically lowest samples (PS-9) or smectite in the uppermost red sandstone member (PS-14).

Diagenetic Mineral Distribution

The distribution of coloration and cementation facies throughout the Baseline Sandstone is not random and the bulk of the patterns are parallel to stratigraphy, particularly contributing to the namesake coloration of the white sandstone and red sandstone members. Stratigraphic patterns show preferential relations of diagenetic mineral combinations and primary textures imparted from the original depositional environment. Coloration and cementation facies distributed stratigraphically through the hanging wall block of the Baseline fault near Tearfault Mesa (diagenetic focus area A of Figures 1B and 1C) are similar in categories observed, but distinctly different, than those in the footwall block of the Baseline fault near Florence mine (diagenetic focus area

Table 4. Non-iron oxide concretion attributes.

Type	Field Attributes		Mineralogy (phase, crystal size, relative amount)[b]	Clay Minerals[c]
	Morphology and Texture	Size[a]		
Carbonate				
Irregular/Pillow-Like/Elongate	Elongate (high length to diameter ratio), lenticular; internal structure typically contains amlgamated masses of spherical carbonate concretions	Up to ~10-20 m length, 2-3 m across	Calcite(?)	Kaolinite, illite
Pipe-Like	Elongate, pipe-like of uniform cross-sectional dimension; massive/structureless internal texture	Up to ~20-30 cm across, unknown length	Calcite(?), hematite grain coats around pipe wall, goethite grain coats in interior	Illite
Spherical/ Spheroidal Cluster Mass	Amalgamated mass of spherical/spheroidal (x-, y-, z-axes or equal length or one axis of unequal length); masses typically parallel bedding	Individual concretions ~3-5 cm in diameter, masses up to ~2-3 m thick and laterally continuous for up to ~5 m	Calcite(?)	Kaolinite(?), illite(?)
Spheroidal to Oblate	Individual mass with one axis of unequal length to the other two (x-, y-, z-axes)	Up to ~50 cm in diameter/ longest dimension	Calcite	No data
Septarian Nodules	Oblate spheroid along one axis (typically parallel to bedding); polygonal ridges ~1 cm tall on outside surface; mineral-filled cracking to massive/structureless interior	Up to ~20-30 cm in longest dimension, up to ~15-20 in shortest dimension	Calcite(?)	No data
Silica				
Silica-Replaced Plant Fragments with Overgrowths	Silica-replaced fragments in float occur as pieces of various shapes, but largely parallel curvature/texture of false-trunk of the original plant; in situ irregular to nodular with long axis parallel to bedding	Plant fragments in float up to ~1-2 m in length, ~10 cm across; in situ nodules ~10-20 cm thick, ~1-2 m lateral extent	Quartz(?)	Illite

[a]Size range/generalized scale of concretion size, not specific measurements

[b]Method: Thin section petrography, SEM, VNIR spectroscopy

[c]Method: Clay-fraction XRD, SEM, VNIR spectroscopy

[d]Method: ICP-MS, XRF

B of Figure 1C). Diagenetic mineral distribution seems to depart from stratigraphic control along the trace of the Baseline fault in the middle to southern part of the field area, where distribution is in close relation to the fault trace (diagenetic focus area C of Figures 1B and 1C).

Stratigraphic Distribution

Diagenetic mineral product distribution in focus area A (Figure 1C) along a stratigraphic transect from the base of the white sandstone member to the lowermost red sandstone member (including attributes observed laterally from the transect) shows a close relation to the lithologies and depositional environment recorded in each member (Figure 12). The stratigraphic attributes of this focus area were only generally described, but overall lithologies and depositional environments are consistent with nearby measured sections of Aschoff and Schmitt (2008). In general, the finer-grained inter-

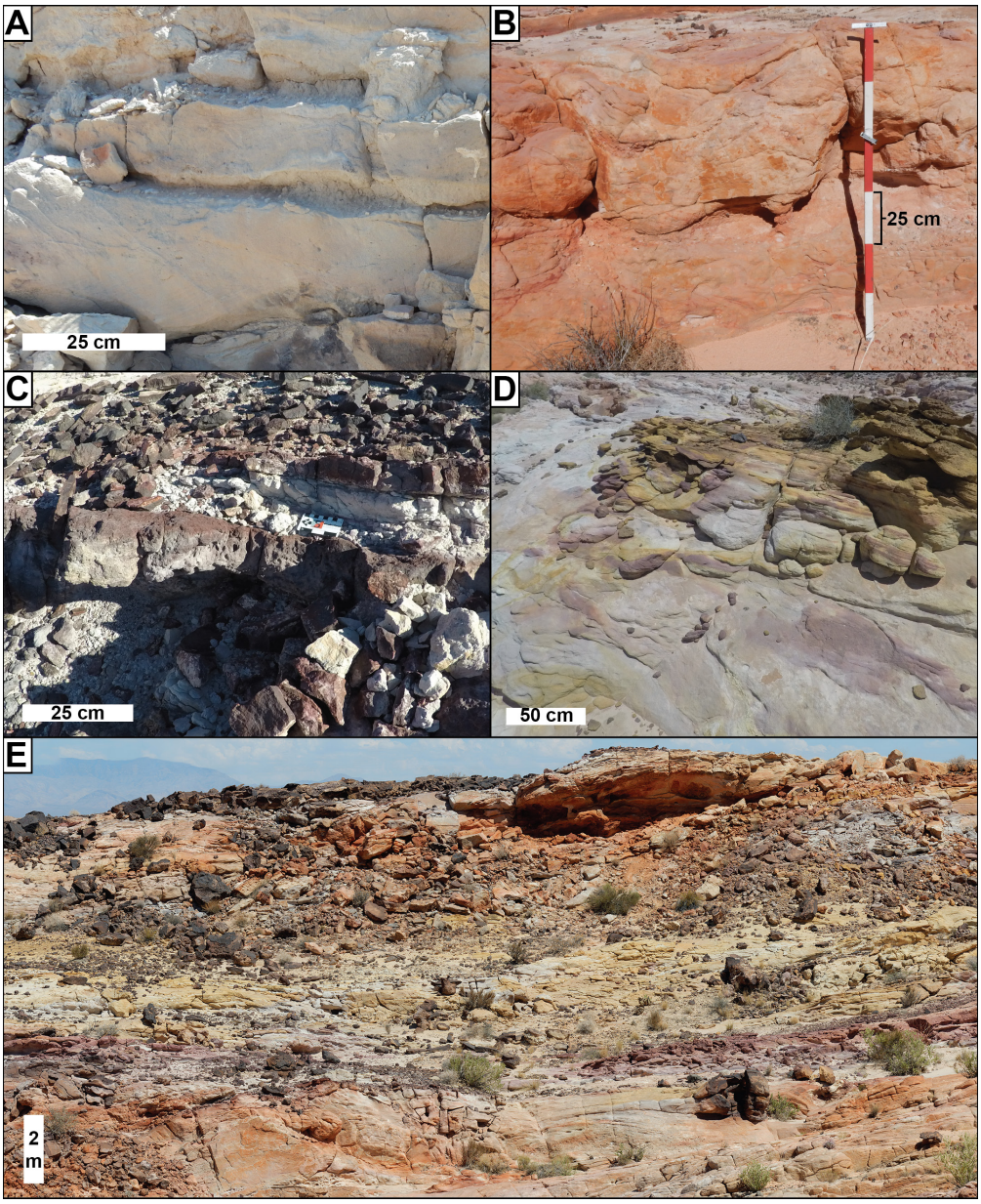

Figure 3. Coloration facies of the white sandstone member (Kbw): (A) Most common is white to tan coloration. (B) Red to brick-red coloration. (C) Stark white siltstone/sandstone grades upward through purple coloration to capping brick red cementation horizons. (D) Dark yellow/yellow-brown sandstone and purple coloration. (E) Outcrop panorama from a location about 200 m south-southwest of key outcrop 1 showing the range in coloration of the white sandstone member and its typical diffuse expressions (scale bar indicates stratigraphic thicknesses of lowest beds).

vals likely represent sheetflood-dominated alluvial fan deposits, and the coarser-grained parts that contain abundant conglomerate and cobble to boulder conglomerate likely represent debris flow-dominated alluvial fan deposits (Aschoff and Schmitt 2008; McNamara, 2010).

The white sandstone member in focus area A (Figure 12) is predominantly white to tan in color with multiple overprinting hues. Distinct patterns in coloration observed through the stratigraphic section define four distinct stratigraphic intervals of note. The lowermost few tens of meters, as well as the interval from about 175 m through to the top of the white sandstone member, are characterized by the predominant co-occurrence of red and yellow hues superimposed on white coloration. Coloration patterns are more complex from about 30 m above base to about 100 m above base. Red, yellow, and purple hues occur in this interval superimposed on the white coloration. Commonly, red and yellow coloration are not directly adjacent to one another except through an intermediate of purple or white coloration. This interval coincides with an overall finer-grained lithology that appears to be part of a sheetflood-dominated alluvial fan depositional environment. The coarser-grained interval between about 100 to 175 m stratigraphic

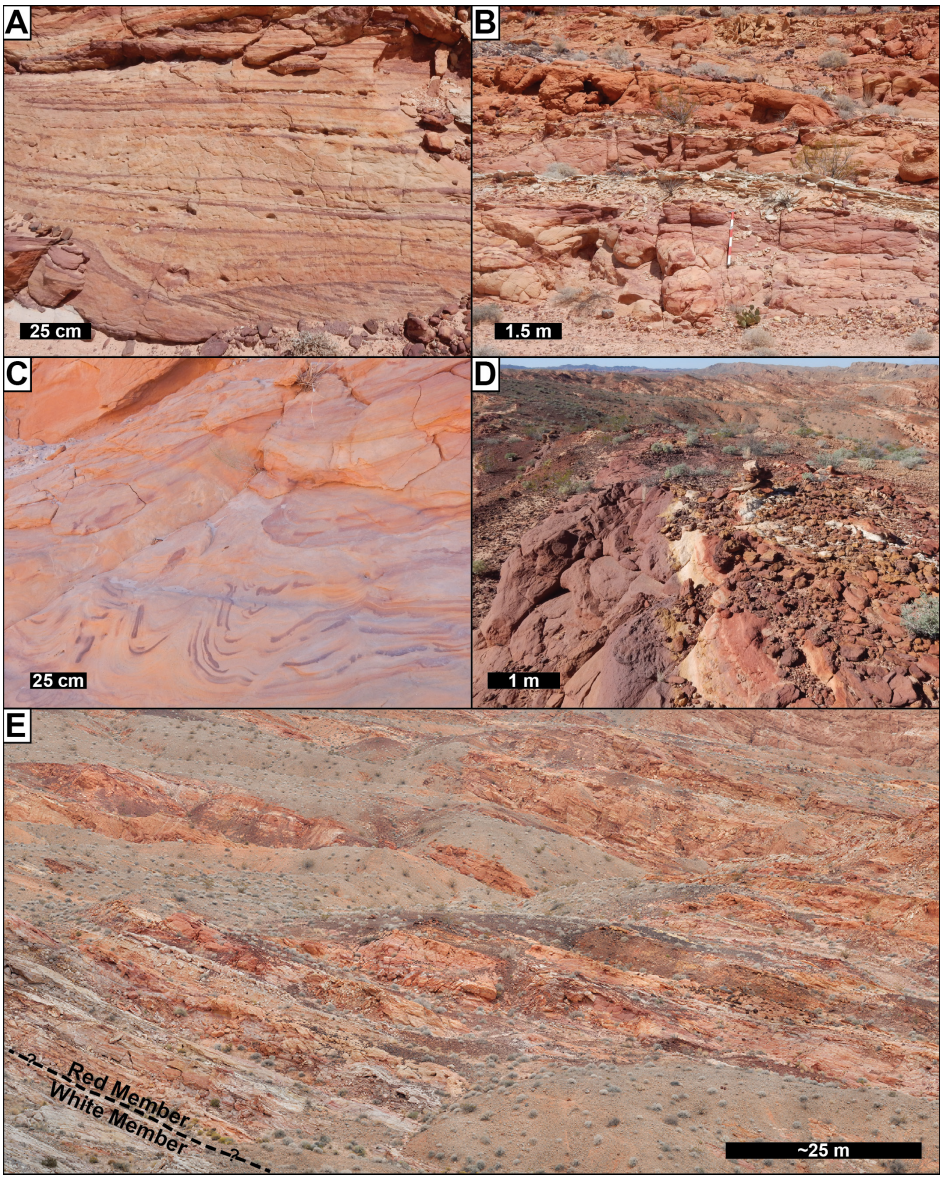

Figure 4. Coloration facies of the lower red sandstone member (Kbr). (A) Red and purple coloration, with increased concentration at cross-stratification surfaces. (B) Range of red and purple to white/tan coloration characteristic of the member (Jacob's staff near image center 1.5 m tall with each red/white bar = 25 cm). (C) Purple coloration patterns found along soft-sediment deformation surfaces. (D) Intensely concentrated red and purple coloration. (E) Perspective view of the lower red sandstone member in the study area (about 75 m of section), showing the range of colors and general bedding-parallel concentration of colors.

height exhibits much less variability in hue, instead exhibiting either white or red coloration. The coloration at the white–red sandstone boundary changes to a predominant medium red coloration.

Cementation facies occur in similar zonation to the coloration facies and overall seem to be more abundant where the member is finer-grained as part of the sheetflood-dominated alluvial fan (Figure 12). Concretion forms vary in morphology and size along with a variety of ironstone horizon types throughout the lowermost 100 m of the white sandstone member. Where the formation is coarser-grained and red coloration is more prevalent about 100 to 175 m above base, there is a dearth of cementation facies, but with a transition to finer-grained sediments irregular and iron-replaced fossil wood with overgrowths, and the reoccurrence of concretionary forms. Southeast about 2 km laterally along strike from the stratigraphic transect, small (less than 1 cm in diameter) spherical concretions and iron-replaced fossil wood fragments/spheroidal concretions, with wood fragments at their center, occur at the about the 350 to 400 m stratigraphic interval, but only minor amounts occur along the transect at diagenetic pattern focus area A (they are more common southward approaching the Baseline fault). The dominant concretionary mineralogy changes from iron oxide throughout

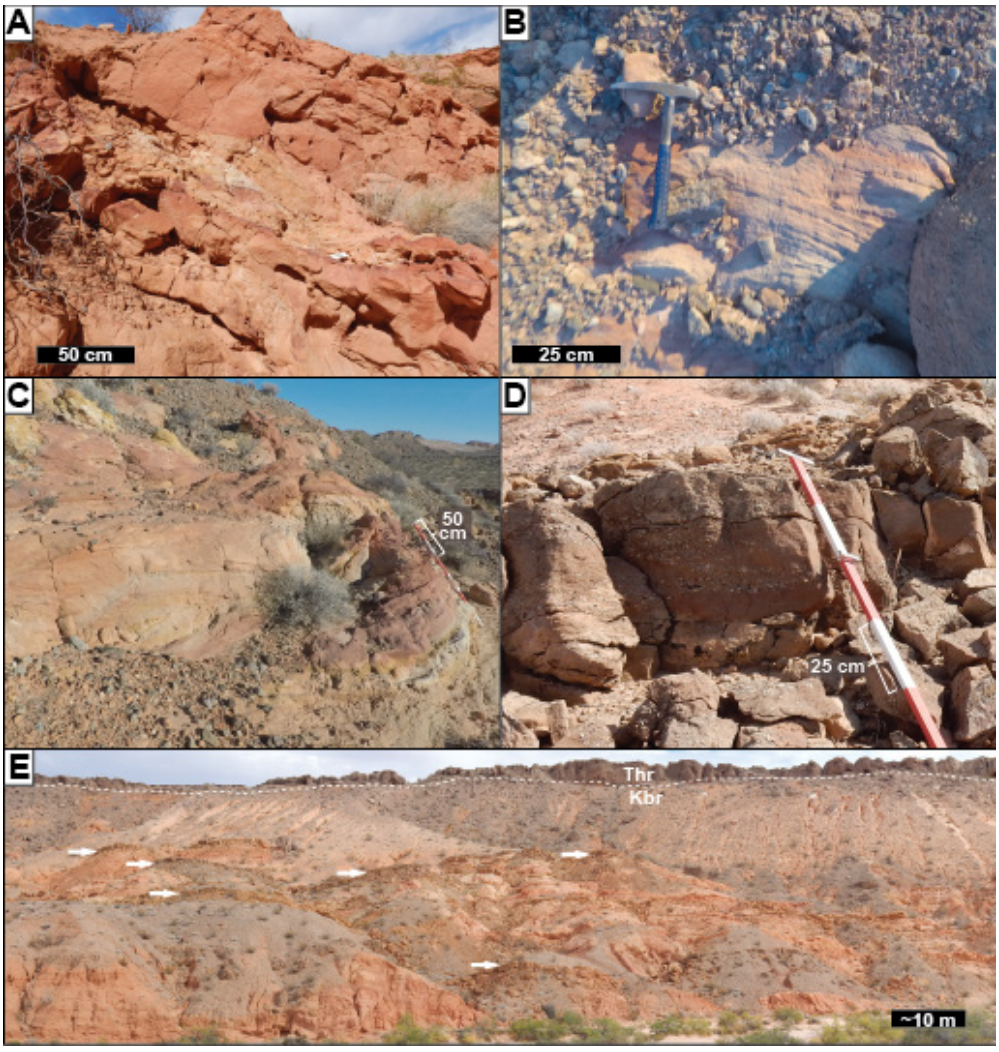

Figure 5. Coloration facies of the upper red sandstone member (Kbr). (A) Predominately solid brick red characteristic of the upper part of the member. (B) White to light red coloration of the uppermost part of the member (about 3 m below the contact with the Rainbow Gardens Member of the Horse Spring Formation). (C) Range of coloration variability expressed in the upper red sandstone member (1.5-m Jacob's staff at right). (D) Brown-colored conglomeratic lens. (E) Panorama of the uppermost red sandstone member (Kbr) and contact with the overlying Rainbow Gardens Member (Thr, prominent cliff band at ridge top), showing brown coloration of the conglomeratic lenses (white arrows) and red siltstone/sandstone of the surrounding floodplain sediments.

the white sandstone member to carbonate in the uppermost white sandstone and the lowermost red sandstone members. Digitate surface ironstone horizons coincide with this switch in dominant mineralogy.

Diagenetic mineral product distribution in focus area B (Figure 1C), documented along the continuous stratigraphic section through the entirety of the Baseline Sandstone (Figures 13 and 14) also reveal associations between diagenetic mineralogy and depositional environment. The white sandstone member is predominantly white in color with a mix of other hues exhibiting a diffuse and pastel (less concentrated) expression similar those exposed in diagenetic pattern focus area A (Figure 12). The lower-most white sandstone member shows greater color variability (including red, yellow, purple, and white hues), with a transition to fewer hues throughout the middle part. The uppermost white sandstone exhibits a gradational change up section from white coloration to predominantly yellow/yellow-brown coloration. Overall, the lower-most red sandstone member is red in color with other colors (purple, yellow, and white hues) that occur in a much more variegated and concentrated expression than in the white sandstone member. Intense color variability extends through the lower red sandstone member until about 750 m above the base, corresponding to the transition from a fluvial fan to the finer-grained fluvial plain-dominated part of the section. The upper half of the red sandstone is predominately solid red-colored with minor color variation of yellow and white in a diffuse/pastel expression. The lenticular conglomeratic bodies exhibit a brown to yellow-brown coloration.

Concretionary forms occur throughout the Baseline Sandstone, but iron oxide concretion forms are

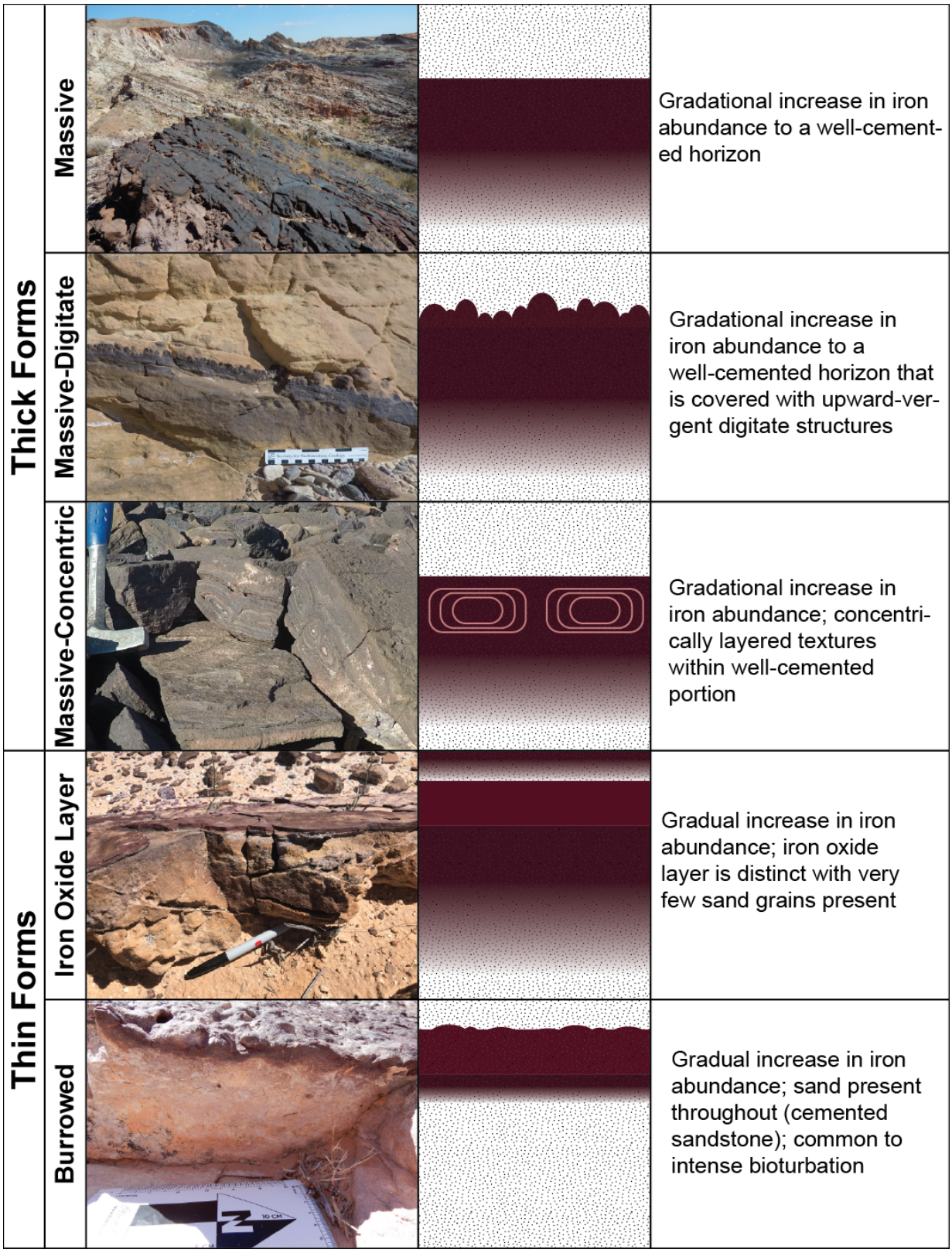

Figure 6. Examples of ironstone horizon types of the cementation facies, with photographs of examples (left column), idealized schematic showing distribution of iron oxide minerals in relation to the alluvial-fluvial sandstone matrix (center), and general description (right column).

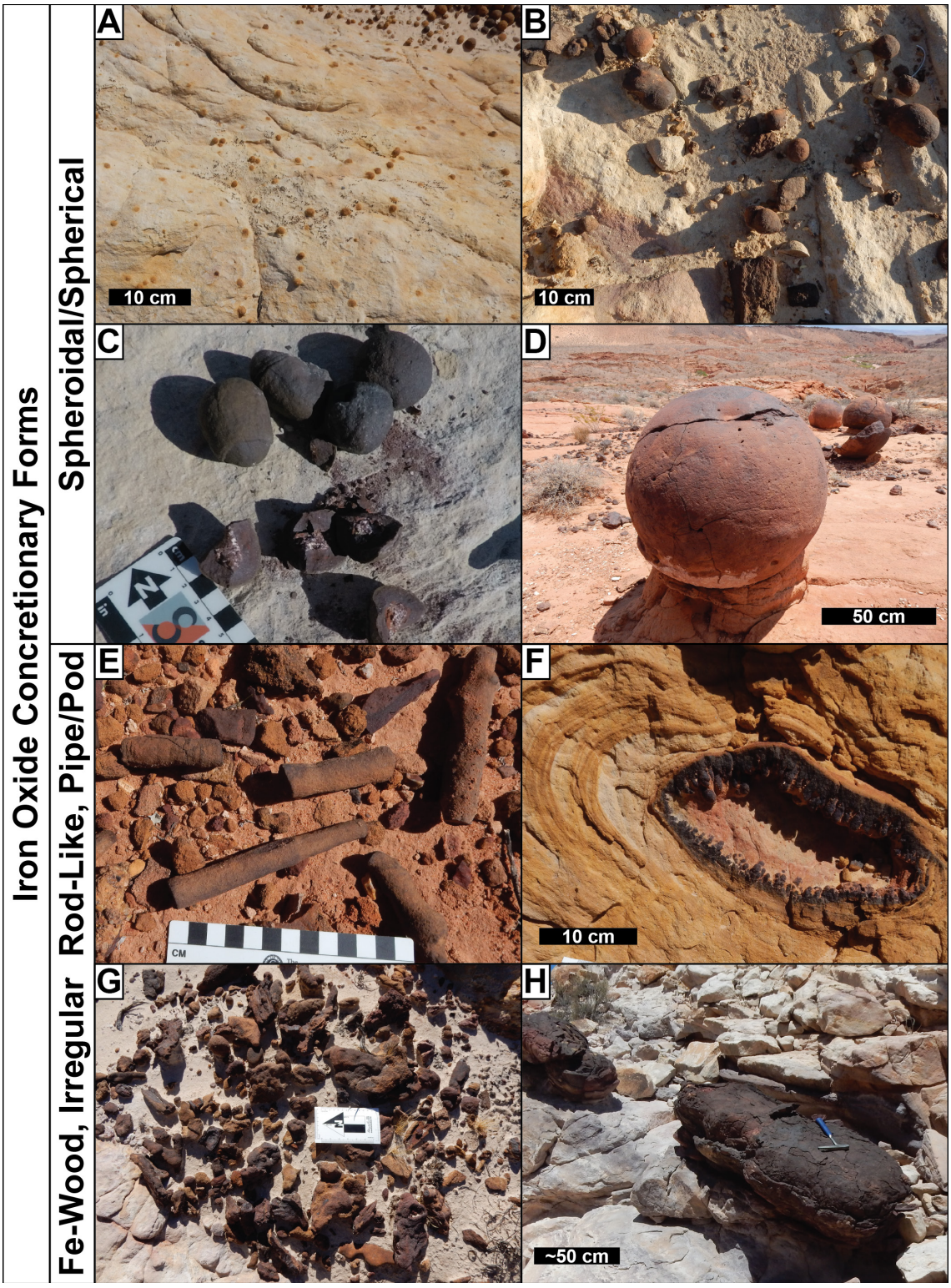

Figure 7. Examples of iron oxide concretionary forms of the cementation facies. (A) Small spherical concretions. (B) Spheroidal to irregular iron oxide masses that commonly contain wood fragments. (C) Spheroidal concretions that exhibit a rinded morphology and loosely cemented stark white center. (D) Large spherical concretion. (E) Cylindrical forms likely of rhizocretion or iron-replaced burrow origin. (F) Pod-like form with digitate structures oriented radially towards the center and concentric Liesegang banding. (G) Small irregular masses and iron-replaced wood fragments. (H) Large irregular masses.

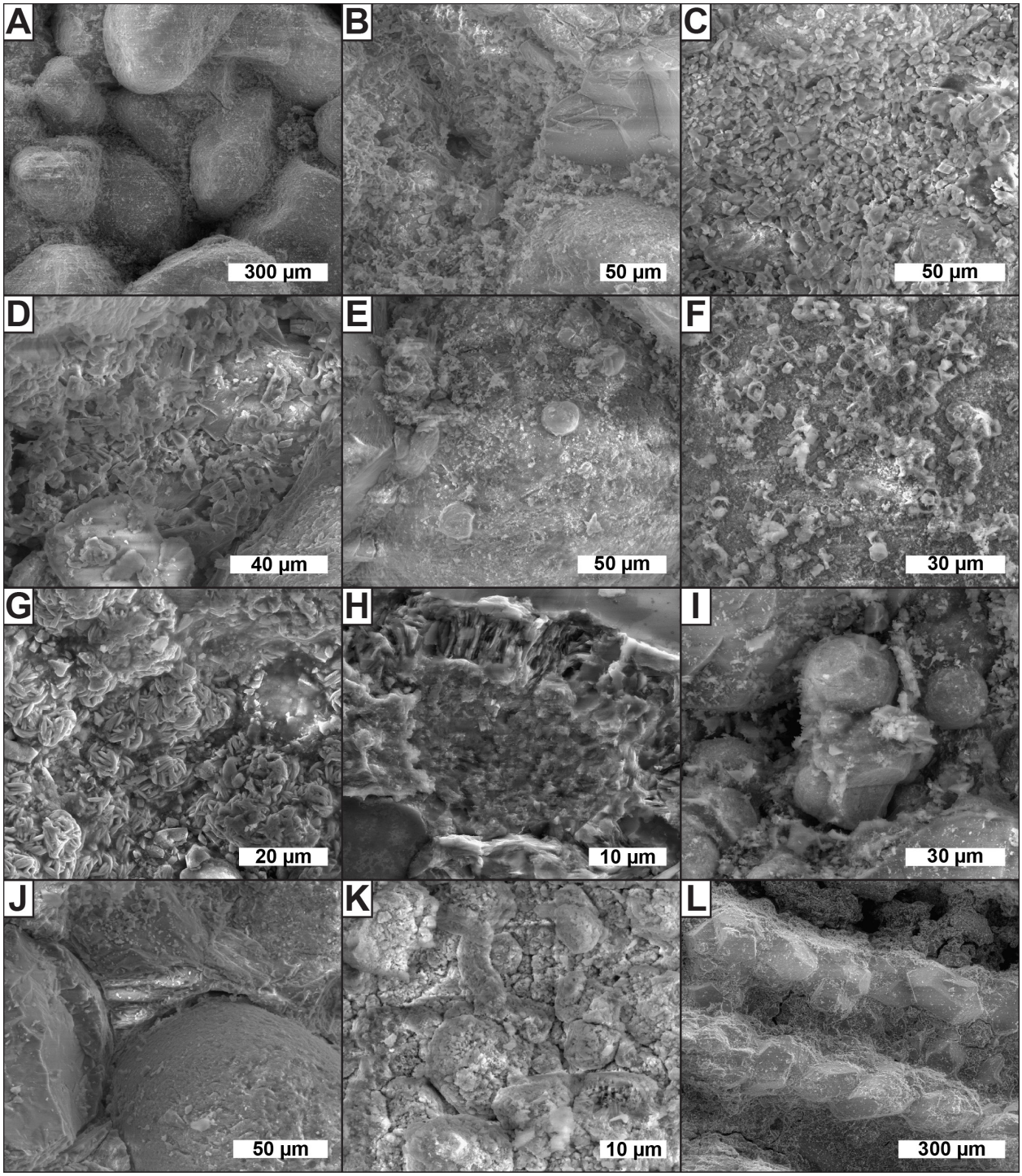

Figure 8. SEM images of representative coloration (A through F) and cementation (G through L) facies. (A) Yellow/yellow-brown sandstone contains acicular to platy goethite crystals. (B through D) Red-colored sandstone commonly contain platy or rhombohedral hematite. (E) Purple-colored sandstone contains hematite spherules of the pore-fill cement. (F) White-colored sandstone contains possible chlorite rims around a precursor(?) grain. (G) Hematite rosettes from metal oxides precipitated along the Baseline fault plane (Figures 15B and A4D). (H) Pore-filling iron oxides and kaolinite in a burrowed ironstone horizon. (I) Hematite spherules that comprise the iron oxide layer ironstone horizon type. (J) Pore-filling carbonate cements and circumgranular cracking. (K) A wood fragment replaced by acicular hematite. (L) Euhedral quartz crystals that replaced a fragment of *Tempskya*(?).

Figure 9. White sandstone member iron oxide concretionary forms that are associated with biological material and burrowing. (A) Assorted concretions from the mid to upper white sandstone member: 1, 4, 5, 7 are concretions that have preserved wood material and wood grain textures by iron oxides having cementation continued into the surrounding sandstone matrix. Concretion 2 is a rod-shaped form that represents either a rhizocretion or iron-replaced burrow. Concretion 3 is a spherical/spheroidal form, and 6 is a spheroidal form with smaller spheroidal forms superimposed, forming a "knobbly" external texture. (B) Iron-replaced wood fragment with iron oxide cements extends slightly (about 1 to 2 cm) from the original wood surface into the surrounding sandstone matrix. (C) Spherical/spheroidal concretions that exhibit concentric zonation from core outward: poorly cemented sandstone (left) or dark gray pyrite-cemented sandstone (right), bright orange jarosite, bright red hematite, dark purple/gray is a mix of hematite and goethite, and their exterior is a thin (about 2 to 3 mm) reduced/bleached rim.

most abundant through the white sandstone member and lower half of the red sandstone member and carbonate concretion forms predominately occur in the upper red sandstone member. Concretions throughout the white sandstone occur most commonly as small (less than 5 cm in diameter) spheroidal forms, with some that contain fossil wood fragments, and iron oxide-replaced fossil wood fragments. Pipe/pod-like iron oxide concretion forms occur in the uppermost about 50 m of the white sandstone coincident with brown to yellow-brown coloration and digitate surface ironstone horizons. Irregular concretions are more common up section and iron oxide-replaced burrows and rhizocretions, plus iron oxide-replaced fossil wood fragments are in the lower-middle red sandstone member. Coincident with the change in coloration to a primarily monotone red at about 750 m above base is a distinct end to abundant iron oxide concretion occurrence.

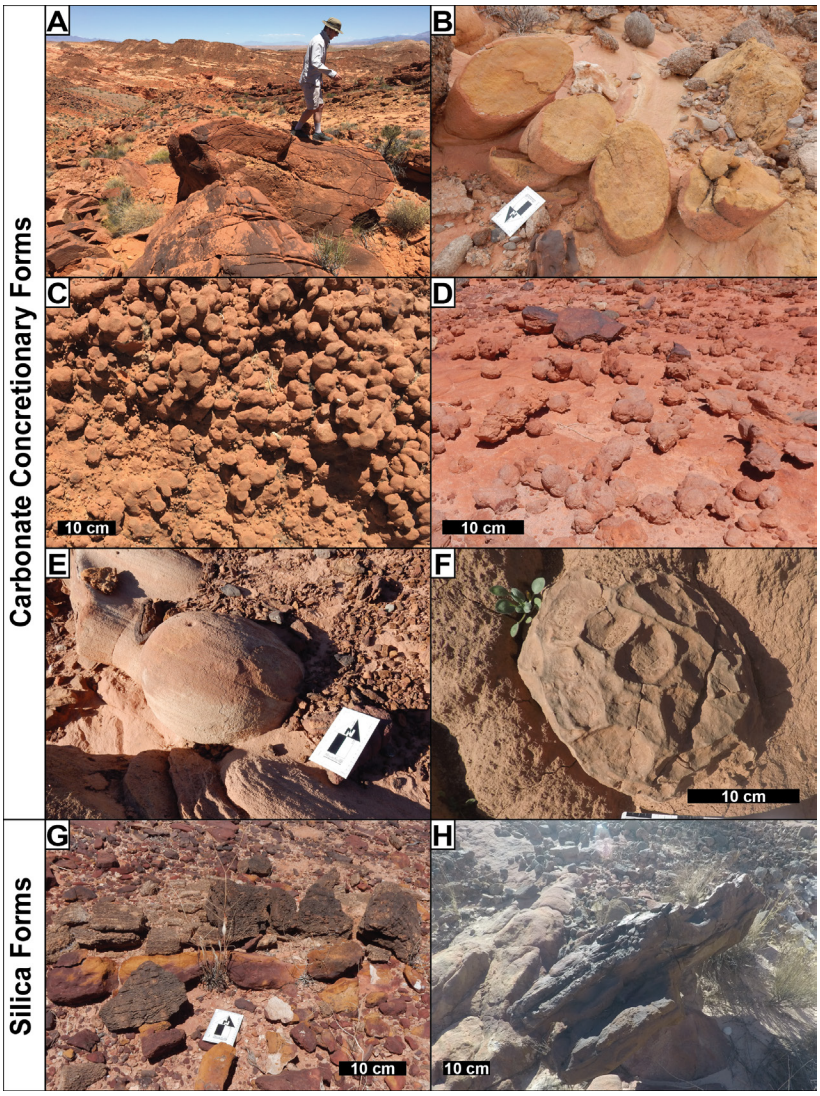

Figure 10. Examples of carbonate (A through F) and silica (G through H) concretionary forms of the cementation facies. (A) Large (about 30 to 50 m length, 2 to 3 m in diameter) elongate carbonate forms. (B) Pipe-like form. (C and D) Clusters of spherical forms in the red sandstone member (C), and the Aztec Sandstone (D). (E) Spheroidal to oblate form. (F) Septarian nodules of the upper red sandstone member. (G) Silica-replaced tree trunk in float, exhibits textures similar to *Tempskya*(?). (H) Bedding-parallel, laterally restricted (about 3 m extent), silica-cemented mass with associated silica-replaced *Tempskya*(?).

Ironstone horizons are restricted to the white sandstone and lower red sandstone members, coinciding with the occurrence of concretionary forms and the prevalence of the multivariate coloration. The massive horizon sub-form is the most common, and known examples of the other horizon types occur at limited locations. The massive-concentric sub-form only occurs at a few locations in the lower white sandstone, commonly co-occurring with the massive and burrowed sub-forms. The lower white sandstone is the only known location of the iron oxide layer sub-form ironstone horizon type, the best examples of which are about 600 to 700 m laterally southeastward at the same stratigraphic interval from their known occurrence along the stratigraphic section (Figure 13). Massive-digitate ironstone horizons occur primarily along scour surfaces in the uppermost white sandstone (about 500 m above the base) with an additional known occurrence in the middle red sandstone (about 725 m above the base). Carbonate concretions are restricted to the middle to upper red sandstone member along the stratigraphic section, and the only observed in situ example of silica concretions occurs at the white-red sandstone boundary.

Fault-Related Distribution

Striking diagenetic patterns with multiple overprinting patterns occur along the fault trace in focus area C (Figures 1B and 1C) where rocks adjacent to the fault trace exhibit significant color alteration and/or mineralization (Figure 15). In the hanging wall, rocks of the white sandstone member are intensely bleached

Table 5. Bulk ICP-MS results for key redox-sensitive elements, grouped by sample suite to which each sample belongs. Note the degree of error for each element varies as determined by comparison to known standard values..

Sample number	Be (ppm)	Mg (ppm)	Ca (ppm)	Sr (ppm)	Ba (ppm)	Ti (ppm)	V (ppm)	Cr (ppm)	Mn (ppm)	Fe (ppm)	Th (ppm)	U (ppm)
Baseline Fault Transects												
PS-1	0.3	701.3	672.8	25.3	223.9	104.0	9.2	0.5	13.6	2645.0	0.1	0.1
PS-2	0.3	232.5	326.6	11.0	21.0	94.3	10.3	0.4	8.8	1553.3	<0.07	0.2
PS-3	0.2	224.9	500.3	5.2	27.2	78.4	6.0	<0.2	3.9	538.3	<0.06	0.0
PS-4	0.3	442.3	582.8	22.8	91.6	88.0	8.5	1.3	11.2	1491.4	0.1	0.0
PS-5	0.4	564.4	465.5	30.0	115.4	89.1	9.9	0.7	13.6	1449.9	<0.06	0.1
PS-6	0.4	266.1	486.2	24.0	208.7	272.5	8.2	0.2	10.4	950.4	0.1	0.2
PS-7	0.2	255.9	669.8	6.6	23.1	84.5	6.1	0.6	2.8	487.3	<0.07	0.1
PS-8	0.2	167.8	265.3	4.9	14.0	98.1	3.2	0.3	2.6	286.1	0.2	0.2
Coloration Facies												
PS-9	0.2	83.5	266.7	14.4	28.0	77.5	8.7	172.3	20.8	3966.8	0.2	0.2
PS-10	0.2	141.1	437.7	6.6	27.1	81.9	8.3	<0.2	3.7	292.2	0.1	0.1
PS-11	0.4	512.1	443.7	16.2	48.2	119.8	15.4	0.9	22.2	5445.5	0.3	0.3
PS-12	-	-	-	-	-	-	-	-	-	-	-	-
PS-13	0.4	2444.0	7105.7	32.2	110.2	295.0	23.0	79.2	92.1	5488.8	0.9	0.6
PS-14	-	-	-	-	-	-	-	-	-	-	-	-
PS-15	0.2	207.5	1177.2	9.9	45.0	87.5	5.6	0.2	3.8	986.4	0.1	0.1
PS-16	0.2	448.6	345.5	10.6	53.1	138.0	4.7	0.2	8.5	612.2	0.1	0.1
PS-17	0.6	440.2	2532.8	33.8	119.7	521.3	85.3	425.1	48.4	34690.2	1.5	0.9
Cementation Facies												
PS-18	0.3	1644.4	89230.7	40.1	60.3	170.0	12.0	1.3	165.0	5399.1	1.0	0.7
PS-19	0.9	2081.2	6213.3	48.9	201.7	140.9	80.1	42.4	1048.3	28817.4	1.0	2.3
PS-20	0.7	1637.6	5736.3	34.2	122.2	354.9	81.5	410.5	933.5	53743.6	1.4	3.6
PS-21	2.4	261.7	1088.5	22.2	73.9	118.8	202.1	13.2	134.4	99546.7	1.1	3.2
PS-22	-	-	-	-	-	-	-	-	-	-	-	-
PS-23	4.5	1851.4	2742.3	16.7	59.7	273.9	18.6	2.2	138.6	157516.4	1.0	3.9
Measurement Standards												
BLK1	0.0	0.2	<2	0.0	0.0	0.6	0.1	0.1	0.0	0.9	<0.0006	<0.0001
BLK2	0.0	0.2	<2	0.0	0.0	0.6	0.1	0.0	<0.002	<0.1	<0.0006	<0.0001
AGV1-1	1.9	7132.3	30541.1	616.6	1003.8	3871.5	107.9	5.3	642.9	34690.0	4.1	1.7
AGV1-2	1.9	6710.1	29295.5	588.5	965.9	3375.5	104.3	5.9	622.4	33118.9	3.9	1.6
Error Magnitude												
AGV-1-1	-8%	-23%	-14%	-7%	-18%	-39%	-10%	-47%	-10%	-27%	-37%	-13%
AGV-1-2	-11%	-27%	-17%	-11%	-22%	-46%	-13%	-41%	-12%	-30%	-40%	-17%

and exhibit striking coloration overprint patterns within about 50 m of the fault trace. Rocks of the white sandstone adjacent to the fault trace exhibit coloration overprinting consisting of a light red base coloration with thin (up to about 5 mm) darker red to purple parallel color bands. In a few examples, red pinstriping is

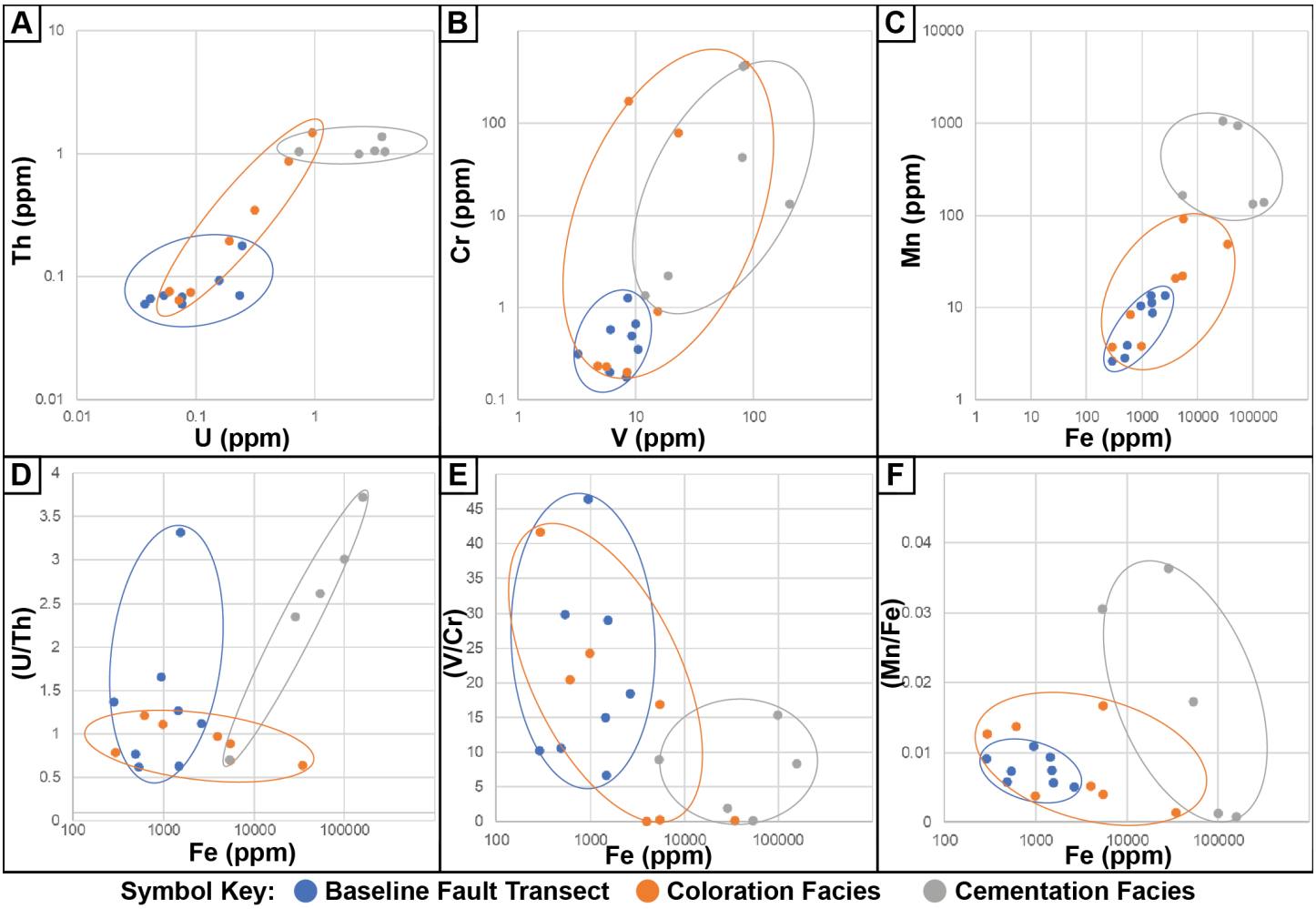

Figure 11. Cross-plots of elemental concentrations for key redox-sensitive elements as measured using ICP-MS. The A through C simple cross-plots show that the Baseline Fault Transects samples (BFT) and the cementation facies overlap with coloration but do not overlap each other. In D through F, elemental ratios are plotted against iron concentration to normalize for concentration effects; note that the distinct plotting areas of the BFT and cementation facies samples remain.

also overprinted by purple parallel color bands. Coloration patterns nearer to the fault commonly exhibit an orientation parallel to the fault plane, crosscutting bed boundaries. white sandstone member rocks immediately adjacent to the fault are most commonly stark white and friable. In some locations immediately abutting the fault, the white sandstone exhibits a dusky purple to purple-gray coloration. Reflectance spectroscopy (Figures 15E and 15F) shows that the stark white coloration coincides with the occurrence of kaolinite clay (absorption couplet about 2200 nm), red and purple colors indicate hematite (absorption features near 600 and 850 nm), and yellow coloration indicates goethite (absorption feature at about 1000 nm).

The fault plane itself commonly exhibits dense iron oxide mineralization either as cement in between grains and cataclastic intergranular spaces, or as crystalline iron oxide coating along the fault plane surface (Figure 8G). Intense mineralization commonly penetrates only up to about 10 cm into the Aztec Sandstone rocks of the fault footwall (Figure 15B). Fault deformation is typically very localized with cataclasis and the damage zone only about 30 cm thick. Minor coloration changes in the Aztec Sandstone are typically darkening adjacent to heavy mineral precipitation along the fault plane, lighter color within a few meters of the fault plane, then a

Table 6. Summary of minerals identified in samples analyzed using clay-fraction XRD (Q = quartz, Ksp = potassium feldspar, K = kaolinite, I = illite, Ch = chlorite, S = smectite, I/S = interlayered illite/smectite, G = goethite, A = alunite, U = unknown).

Powdered Sample	Sample Context	Facies	Minerals Identified in Sample									
			Q	Ksp	K	I	Ch	S	I/S	G	A	U
PS-1	Ja upper red unit	Red coloration	x	x	x	x						x
PS-4	Baseline fault, altered Ja	White-light yellow coloration	x	x	x	x						
PS-6	Baseline fault, Kbw	Stark white	x	x	x				x			
PS-8	Baseline fault, Kbw	Stark white	x		x							
PS-9	Lower Kbw	Purple coloration	x		x	x	x				x	
PS-10	Middle Kbw	White coloration	x		x	x						
PS-11	Kbw-Kbr transition	Red coloration	x	x	x	x			x			
PS-14	Uppermost Kbr	Light red coloration	x	x	x	x		x				
PS-15	Lower Kbw	Yellow coloration	x	x	x	x				?		
PS-16	Upper Kbw	White coloration	x		x	x						
PS-19	Middle Kbr	Giant concretion center	x		x	x				x		

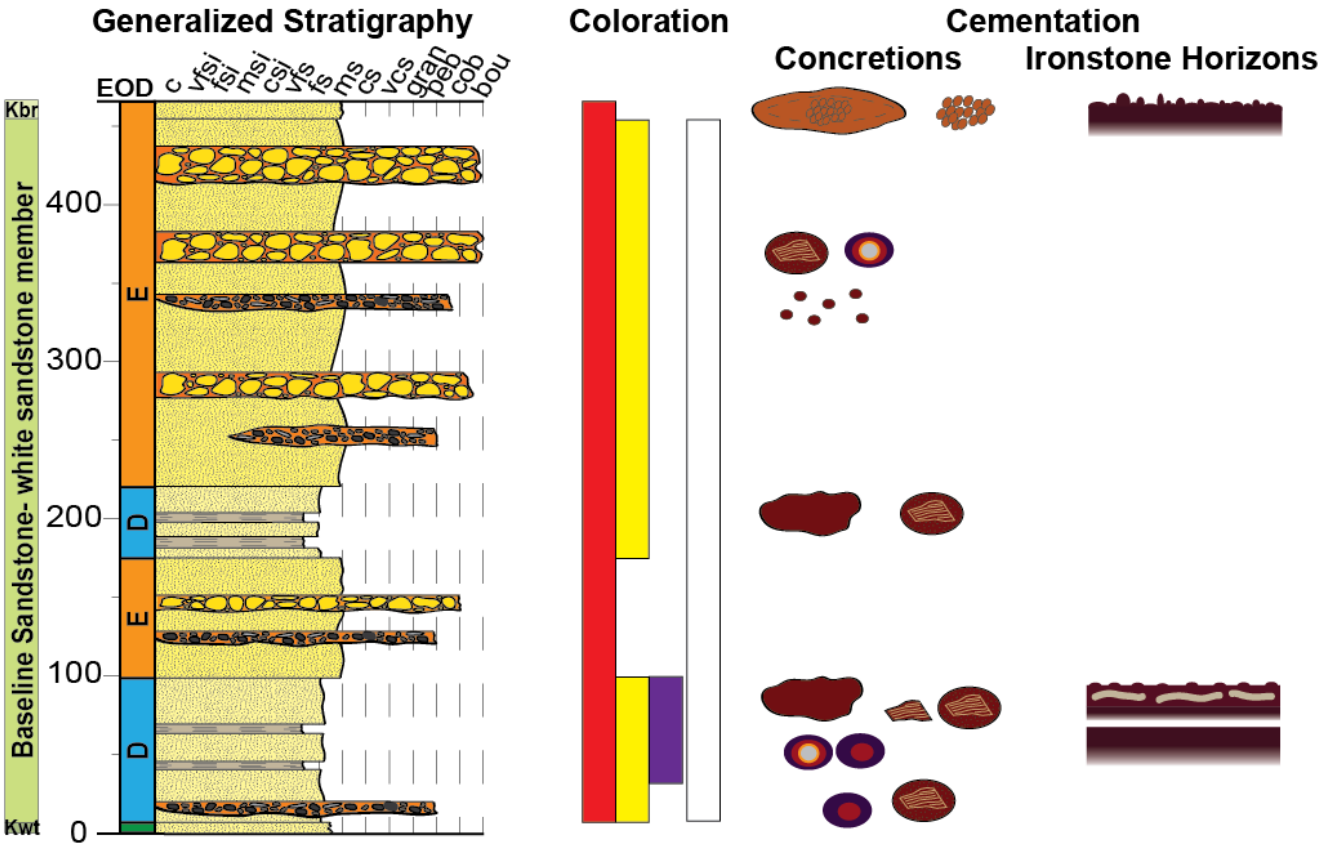

Figure 12. Generalized lithologic and diagenetic patterns of diagenetic pattern focus area A near Tearfault Mesa (Figure 1C). See Figures 3 through 5 for examples of coloration facies and Figures 6, 7, 9, and 10 for examples of cementation facies. Grain size abbreviations: C = clay, vfsi = very fine silt, fsi = fine silt, msi = medium silt, csi = coarse silt, vfs = very fine sand, fs = fine sand, ms = medium sand, cs = coarse sand, vcs = very coarse sand, gran = granule, peb = pebble, cob = cobble, bou = boulder. See Figure 14 for symbol key.

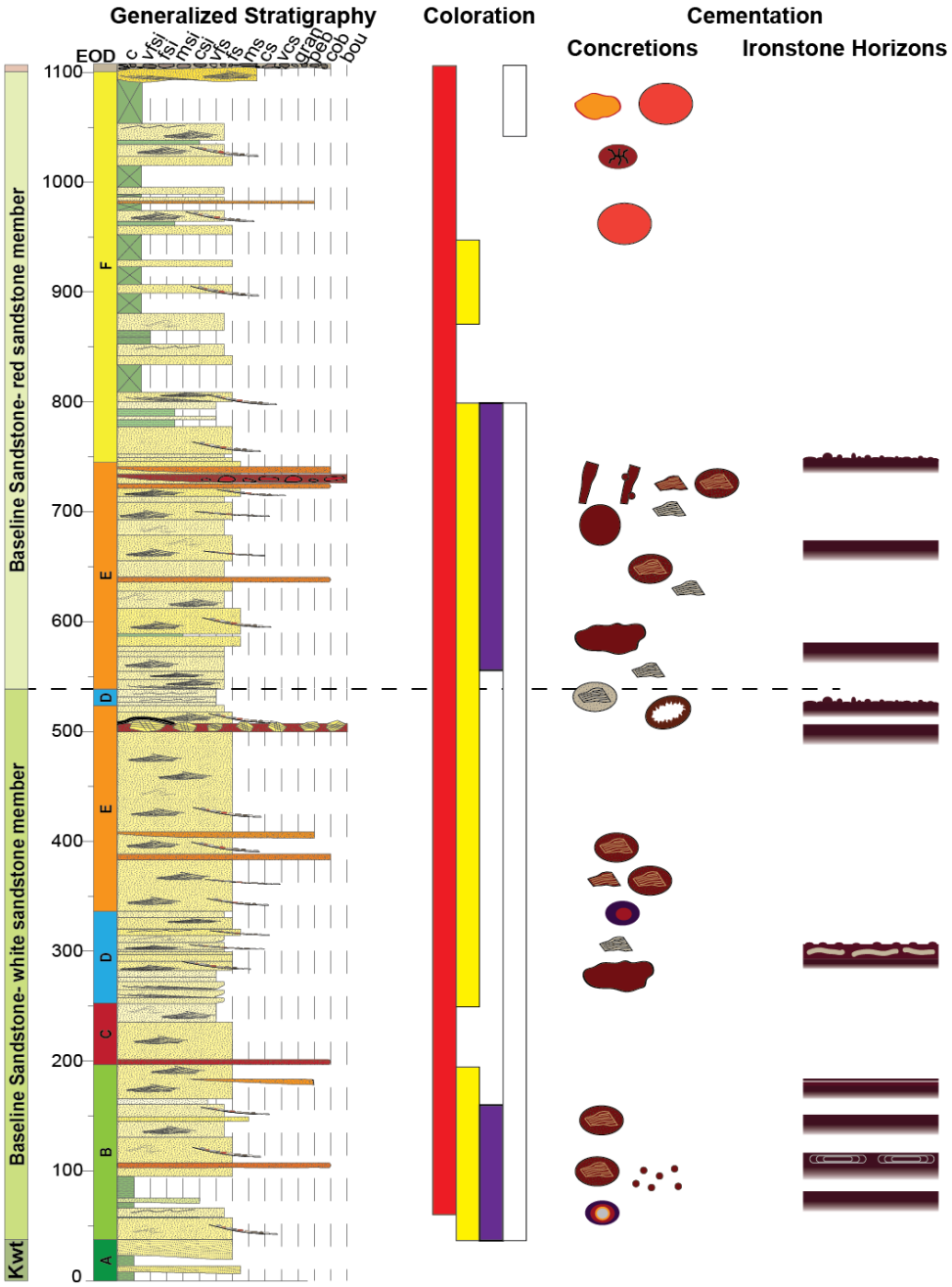

Figure 13. Generalized lithologic and diagenetic patterns of diagenetic pattern focus area B along the stratigraphic section (Figure 1C). See Figures 3 through 5 for examples of coloration facies and Figures 6, 7, 9, and 10 for examples of cementation facies. Grain size abbreviations: C = clay, vfsi = very fine silt, fsi = fine silt, msi = medium silt, csi = coarse silt, vfs = very fine sand, fs = fine sand, ms = medium sand, cs = coarse sand, vcs = very coarse sand, gran = granule, peb = pebble, cob = cobble, bou = boulder. See Figure 14 for symbol key.

return to normal red-orange coloration characteristic of the rest of the formation. Small spheroidal to spherical carbonate concretions commonly occur in patches up to 30 m away from the fault trace. Reflection spectroscopy shows that the dominant iron oxide both accounting for the general red coloration of the formation and the heavy iron oxide mineralization along the fault plane is composed of hematite. Concretion mineralogies (Figure 15F) that occur in the Aztec also exhibit a carbonate composition (absorption features at 2350 and 2500 nm) and dominantly kaolinite, with minor amounts of illite (absorption feature about 2200 to 2210 nm).

Observed alteration patterns are not persistent along the entire trace of the fault. Intense coloration and mineralization patterns associated with the Baseline fault seem to be restricted to within and up to about 100 m north of focus area C (Figures 1B and 1C). Toward the north end of the field area, secondary alteration pat-

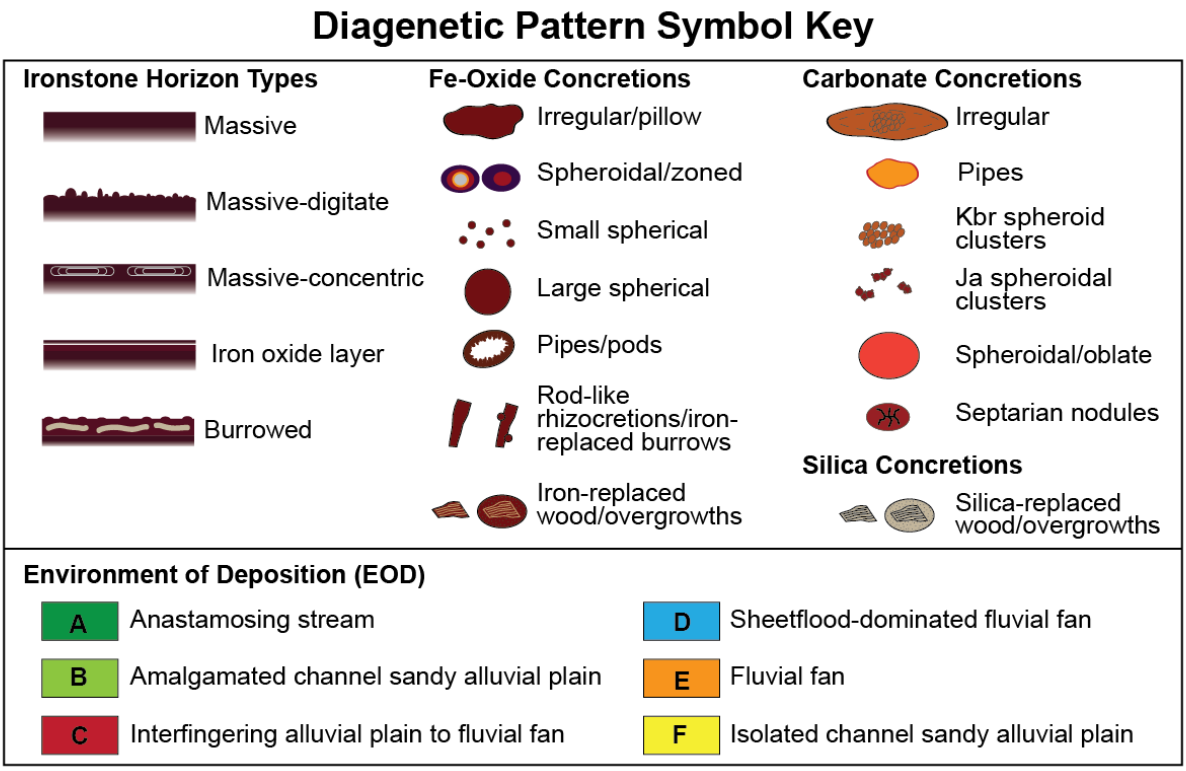

Figure 14. Key for symbology contained within the generalized lithologic and diagenetic patterns (see Figures 12 and 13).

terns are not apparent and the fault crosscuts the predominant iron oxide diagenetic coloration patterns that parallel the stratigraphy.

The Landsat mineral mapping workflow resulted in threshold and classified maps that validate the field observations of stratigraphic and fault-related distribution (Figure 16; also see Results section in the Appendix). The threshold 4/2 ratio map identifies diagenetic coloration patterns associated with hematite mineralogy (red color on Figure 16B), the threshold (4+6)/5 ratio map indicates areas where iron oxide concretions are common (green color on Figure 16B), the threshold 6/7 ratio map reflects ground-based patterns of bleached/altered zones (light blue color on Figure 16B), and finally, the threshold 5/6 ratio map highlights known clay-rich areas (teal color on Figure 16B). An image composite of these band ratios (red channel = 6/7 ratio, green channel = 5/6 ratio, and blue channel = 4/2 ratio) was classified using supervised and unsupervised methods resulting in a more objective visualization of diagenetic mineral distribution, showing they broadly parallel stratigraphic trends and fault-related distribution described above (Figures 16C and 16D).

Distribution Interpretation

The distribution of diagenetic mineral features throughout the field area, in relation to depositional environment, stratigraphic architecture, and structural features (the Baseline fault most importantly), provides clues to the controls on fluid flow through the duration of diagenetic alteration of the formation. In particular, the relations are best developed in chosen focus areas A, B, and C, and overall, the stratigraphic distribution of diagenetic mineral features corresponds with particular depositional environments as described below.

In focus area A, the relations of the diagenetic mineral features to depositional environment and the resultant depositional texture is evident where the white sandstone member is finer-grained overall correspond-

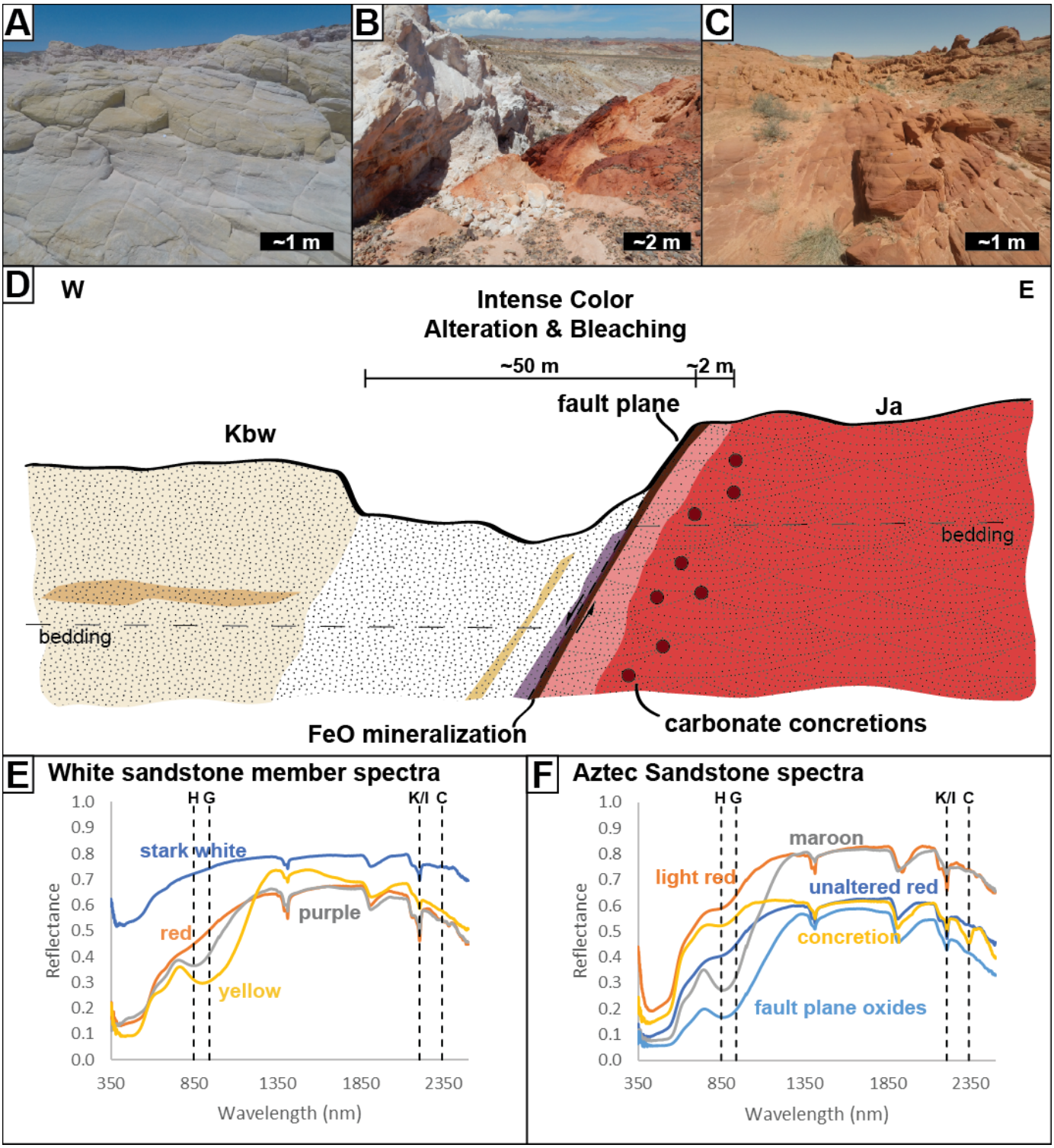

Figure 15. Generalized diagenetic patterns associated with the Baseline fault (diagenetic pattern focus area C of Figure 1C). (A) White sandstone member (Kbw) away from the fault exhibits light, bed-parallel colors. (B) Intensely bleached Baseline Sandstone in the hanging wall is in faulted contact with the red Aztec Sandstone (Ja) in the footwall, with heavy metal precipitation along the fault plane. (C) Unaltered Ja away from the fault is an even red color. (D) Schematic representation of diagenetic mineral patterns adjacent to the fault relate to the representative spectra E and F from the Kbw and Ja, respectively, where dashed lines indicate absorption features of key minerals.

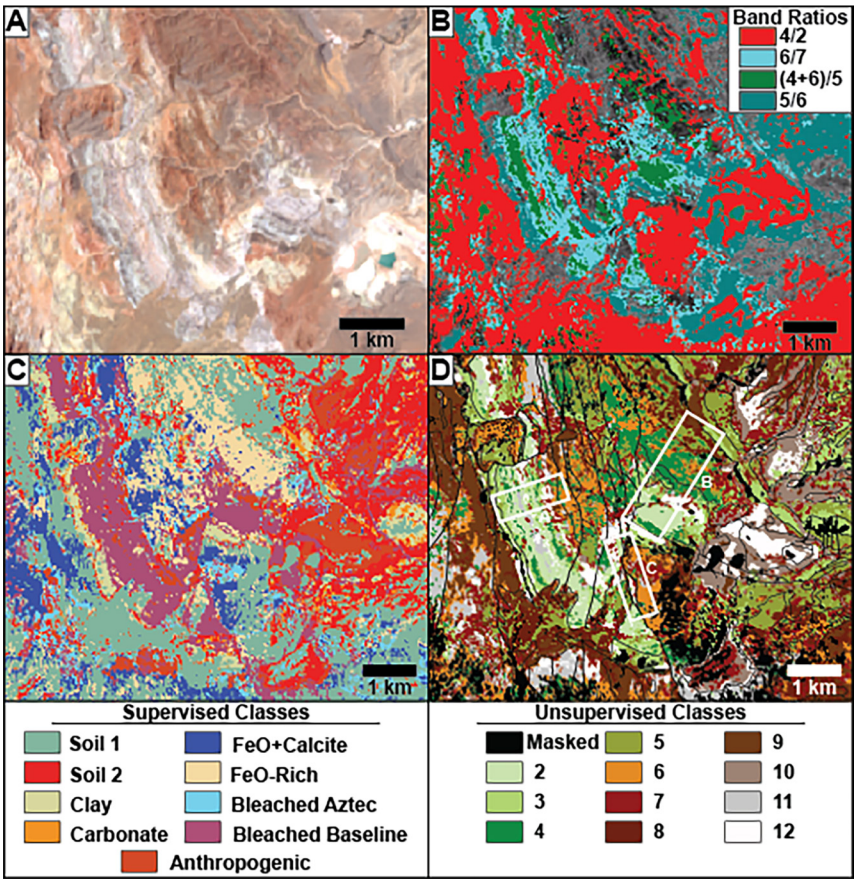

Figure 16. Multispectral remote sensing-derived diagenetic mineral maps: (A) RGB composite to show visible coloration of the Baseline Sandstone, (B) band ratio threshold map, (C) supervised classification, and (D) unsupervised classification with superimposed outlines of the diagenetic focus areas (white boxes). All maps are of the same general area of Figure 1B and derived from Landsat 8 scene LC08_L1TP_039035_20170526_01_T1 acquired May 26, 2017, downloaded from the U.S. Geological Survey EarthExplorer data browser.

ing with a sheetflood-dominated fluvial fan environment (depositional environment D of Figure 12). Here, abundant concretionary facies exhibit greater variability of forms, and higher intensity in coloration. Where the white sandstone is coarser-grained overall corresponding with a debris flow-dominated/channel-reworked alluvial fan environment (depositional environment E of Figure 12), concretionary facies are typically less abundant, and coloration facies are less varied. The depositional environment remains the same with the transition to the lower red sandstone member, with a change to more abundant carbonate concretionary forms, suggesting that the change in concretion mineralogy is not strictly tied to depositional environment.

In focus area B, there appears to be another relation between depositional environment and diagenetic mineral features. In the lower white sandstone member where the depositional environment is that of a sandy braided alluvial plain, ironstone horizons are common along with various small iron oxide concretions in this fine- to medium-grained sandstone lithology. This part of the member is also where the iron oxide layer and massive concentric ironstone horizon sub-forms occur. The formation coarsens upward overall with the transition to the alluvial fan depositional environments (environments C, D, and E on the generalized stratigraphic column of Figure 13), and concretionary forms and ironstone horizons are less abundant. Up section (across the member boundary) there is an overall decrease in grain size and an increase in the amount of silt and mud-sized grains shed from unroofing of the Triassic rocks contained within the hanging wall of the Willow Tank thrust (McNamara, 2010). This is coincident with variability and variegation/concentration of colors, along with an increase in concretion abundance, suggesting that pore-scale anisotropies may have influenced fluid-flow pathways leading to concentration of coloration along sedimentary bounding surfaces (Davis et al., 1997). The lower to upper red sandstone member changes in coloration expression from variegated to

even (Figures 4 and 5), with a decrease in abundance of concretionary forms (Figure 13). These stratigraphic changes likely represent a stratigraphic upper-bound on fluid-flow alteration, with possible influence from reservoir partitioning by finer grained floodplain materials that increase in abundance (depositional environment F of Figure 13). The carbonate cements/concretions of the upper red sandstone member show a preferred relation to lithology with spheroidal/bulbous concretion forms occurring in the sandier sediments whereas the septarian concretions occur in mud/silt-sized sediments, suggesting they formed from early diagenetic processes within the fluvial depositional environment.

Both the intense alteration/bleaching in the hanging wall, and the iron oxide mineralization along the fault plane indicate that the Baseline fault acted as a local conduit for fluid flow. The proximity of stark white coloration and other coloration hues that parallel the fault trace indicate a key relation between coloration and the fault. Overprinting of coloration pinstriping on early or initial coloration and even other pinstripes indicates multiple episodes of chemical reaction fronts through episodic fluid-flow events. Furthermore, the abundant kaolinite identified in the stark white sandstone in close proximity to the fault indicate that intense alteration has occurred along the fault. This is likely due to meteoric fluid infiltration that altered feldspar grains and unstable lithic fragments to produce kaolinite. The crystalline iron oxide rosettes along the fault plane, similar to those observed by Ault (2020), represent mineral precipitation and open space for mineral growth along the fault plane.

Relations and Timing

The determination of the paragenetic sequence of a formation relies in part on understanding the types and distribution of authigenic minerals along with preferred associations between diagenetic mineralogy and lithology (as outlined above). Integration of crosscutting relations observed at formation- to bed-scales between diagenetic mineral products, structural features, and lithology, along with grain- to pore-scale relations observed in thin section elucidate the diagenetic evolution and inform the relative paragenetic sequence of the Baseline Sandstone. Absolute (U-Th)/He dates of select iron oxide samples provide additional constraints on timing of alteration. Results and interpretations from these scaled relations are outlined below.

Relations Between Diagenetic Mineral Products and Structures

The crosscutting of the diagenetic mineral products and structural features are used here to interpret the relative timing of formation of the diagenetic minerals. Extensional and contractional structural features throughout the map area crosscut or overprint the various cementation and coloration facies. Crosscutting relations of diagenetic mineral products and contractional structures differ from those in the adjacent Aztec Sandstone. First, observed diagenetic patterns of both the Baseline and Aztec Sandstones are offset by Miocene-aged normal faults related to Basin and Range extension (Figures 17A and 17B, respectively). In addition, joint sets in this area are likely related to the normal faulting and also cut across diagenetic patterns. These patterns suggest that the main stratigraphic diagenetic patterns in both the Baseline and the Aztec are from an alteration episode that must have occurred prior to Basin and Range extension (pre-18 Ma).

Timing can be further constrained by the relation between coloration and cementation facies and deformation bands. Deformation bands likely formed as a result of Sevier orogeny thrust faulting/shortening and the co-occurrence of deformation bands and coloration have opposite expressions in the Baseline Sandstone versus the Aztec Sandstone. Coloration and cementation facies appear to be overprinted by deformation bands in the lower Baseline (Figures 3B and 17C), expressed by continuity in coloration/cementation across the deformation bands, suggesting deformation bands formed after the coloration. The deformation bands were not observed in higher (i.e., younger) stratigraphic intervals of the Baseline. The opposite case is true for the Aztec, where coloration is not continuous across deformation bands (e.g., Figure 17D), suggesting that the deformation bands formed before the coloration. Since the coloration patterns are the result of fluid flow (Eichhubl et al., 2004), it seems likely that the porosity-permeability

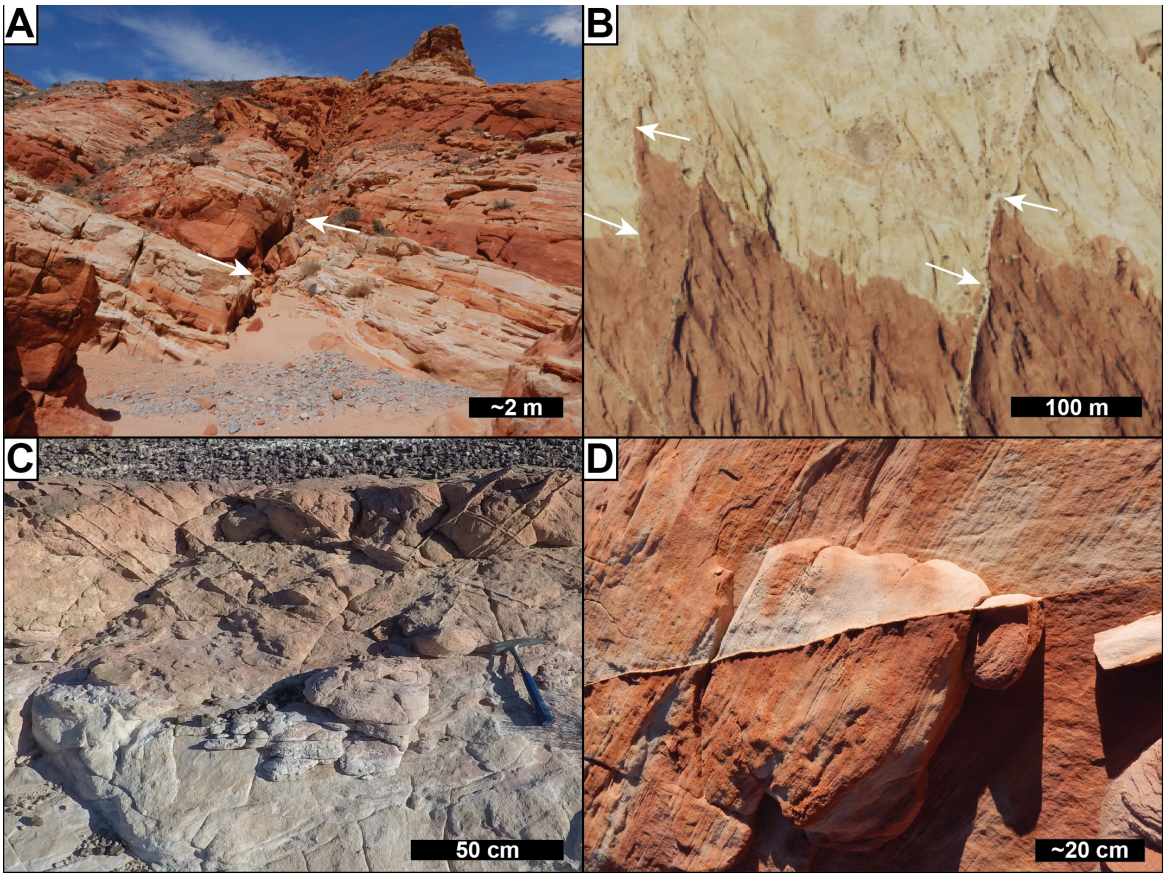

Figure 17. Cross-cutting relationships between coloration and structural features of the Baseline Sandstone and the adjacent Aztec Sandstone. (A) Coloration patterns of the Baseline Sandstone, lower red sandstone member, offset by the Miocene Baseline fault in the north end of the field area (white arrows indicate top of equivalent white/bleached bed); note the red unit above the arrows are also equivalent but display lateral changes in thickness/expression. (B) NAIP aerial image of the Silica Dome area in Valley of Fire State Park, shows the offset of the coloration boundary (indicated by white arrows) by Miocene normal faults. (C) Coloration facies of the white sandstone member increase in intensity toward the bed top, and is overprinted by deformation bands. (D) Coloration of the Aztec Sandstone in the adjacent Valley of Fire State Park exhibits coloration differences on either side of deformation bands.

of the deformation bands exerted an influence on fluid-flow paths, and thus the distribution of coloration in the sandstone beds.

The restriction of deformation bands to the lowermost Baseline Sandstone likely indicate that coloration and cementation facies were formed after thrust faulting initiated, and shortly after deposition of the white sandstone member began, during the early diagenetic stage, prior to any sufficient compaction and lithification needed in order for deformation bands to form (Issen and Rudnicki, 2000; Fossen et al., 2007, 2017). Conversely, the adjacent Aztec Sandstone was already lithified/cemented at this time, meaning that the complex relations and differences between formations might be a function of the different formation stress responses, where the Aztec (a lithologically more homogeneous eolian unit) was capable of formation of deformation bands. Therefore, crosscutting relations between diagenetic mineral products and structural features bracket the timing of an episode of iron oxide coloration and cementation to shortly following deposition, but prior to the formation of deformation bands within the Baseline. Further characterization of the type of deformation bands and determination of their likely formation mechanism (e.g., granular

flow vs. cataclasis, after Fossen et al., 2017) may also help to constrain timing of deformation band formation and thus relative timing of diagenetic mineral formation.

Relations Between Diagenetic Mineral Features and Lithologies

Examination of the broad focus areas and key outcrops show the close relation between diagenetic mineral features and lithology/sedimentary structures. Generally, diagenetic mineral features that are away (greater than 50 m) from the Baseline fault are parallel to bedding and stratigraphy. The degree to which sedimentary structures and bedding controls the distribution of diagenetic coloration and cementation differ in each member. In the white sandstone member, coloration patterns are typically diffuse, bed parallel, and commonly crosscut 1st- to 2nd-order surfaces and follow 3rd-order surfaces (Figures 3B, 3D, and 3E; surface hierarchy after terminology of Miall, 1996; Allen, 1983; Davis et al., 1997). Ironstone horizons are typically at bed boundaries (2nd-order surfaces; Figure 6) along the upper parts of the host beds (Figure 6). The digitate surface horizon type when in situ typically occurs at scour surfaces (2nd- to 3rd-order surfaces). It is unclear if the cemented horizon is in the underlying lithology or directly along/above the scour surface, but the digitate structures are oriented upward from this surface.

The lower red sandstone member coloration patterns are typically more variegated/concentrated and exhibit a closer relation with lithologies. Coloration appears to be concentrated along 1st- to 2nd-order surfaces (Figure 4A), even following surfaces distorted by soft-sediment deformation (Figure 4C). Massive sandstone and weakly stratified sandstone exhibit coloration expression that crosscut bounding surfaces similar to coloration patterns of the white sandstone member (Figure 4D). Coloration patterns of the upper red sandstone member appear to be somewhat similar in crosscutting relations to the white sandstone where they typically crosscut 1st-order bounding surfaces and commonly follow 2nd- to 3rd-order surfaces. Lenticular conglomerate bodies commonly exhibit brown coloration in contrast with the surrounding red sandstone and mudstone. Ironstone horizons of the red sandstone member exhibit similar crosscutting relations to bounding surfaces as the white sandstone.

The differences in the white and red sandstone members between coloration and bounding surface likely relate to original depositional porosity and permeability, and their influences on diffusive formation of the iron coloration and cementation facies (Davis et al., 1997). These differences in permeability may be controlled by increased proportion of fine-grained materials and possibly clay minerals concomitant with the unroofing of Triassic rocks in the hanging wall of the Willow Tank thrust along with changes in depositional environment in lower red sandstone member stratigraphy. Alternatively, the unroofing of the Triassic section in the hanging wall of the Willow Tank thrust may have resulted in deposition of clay minerals or other materials that acted as preferential nucleation sites of iron oxides, resulting in the variegated coloration.

Thin Section Relations

Thin sections exhibit similar characteristics across all samples, as well as unique attributes that relate to diagenetic mineral context (Figure 18). Generally, thin section samples of the Baseline Sandstone are composed of quartz arenite to sublitharenite (after Folk et al., 1970). Samples are typically moderately to very well-sorted, and framework grains are sub-rounded to well-rounded in white sandstone member samples, with sub-angular to rounded in red sandstone member samples. Intergranular primary porosity is most common, with minor additional secondary porosity from quartz grain fracturing and unstable lithic and/or feldspar grain dissolution (Schmidt and McDonald, 1979). Samples of the white and lower red sandstone members typically exhibit an open pore network with connected pore spaces that are wide, but still smaller than adjacent individual grains. Point and long contacts between grains are most common, however, some samples seem to exhibit incipient (i.e., not well-developed) concavo-convex grain contacts. The grain contact type seems to correlate with stratigraphic position, with samples from stratigraphically lower positions exhibiting longer and concavo-convex grain contacts, and those from stratigraphically higher positions exhibiting point and

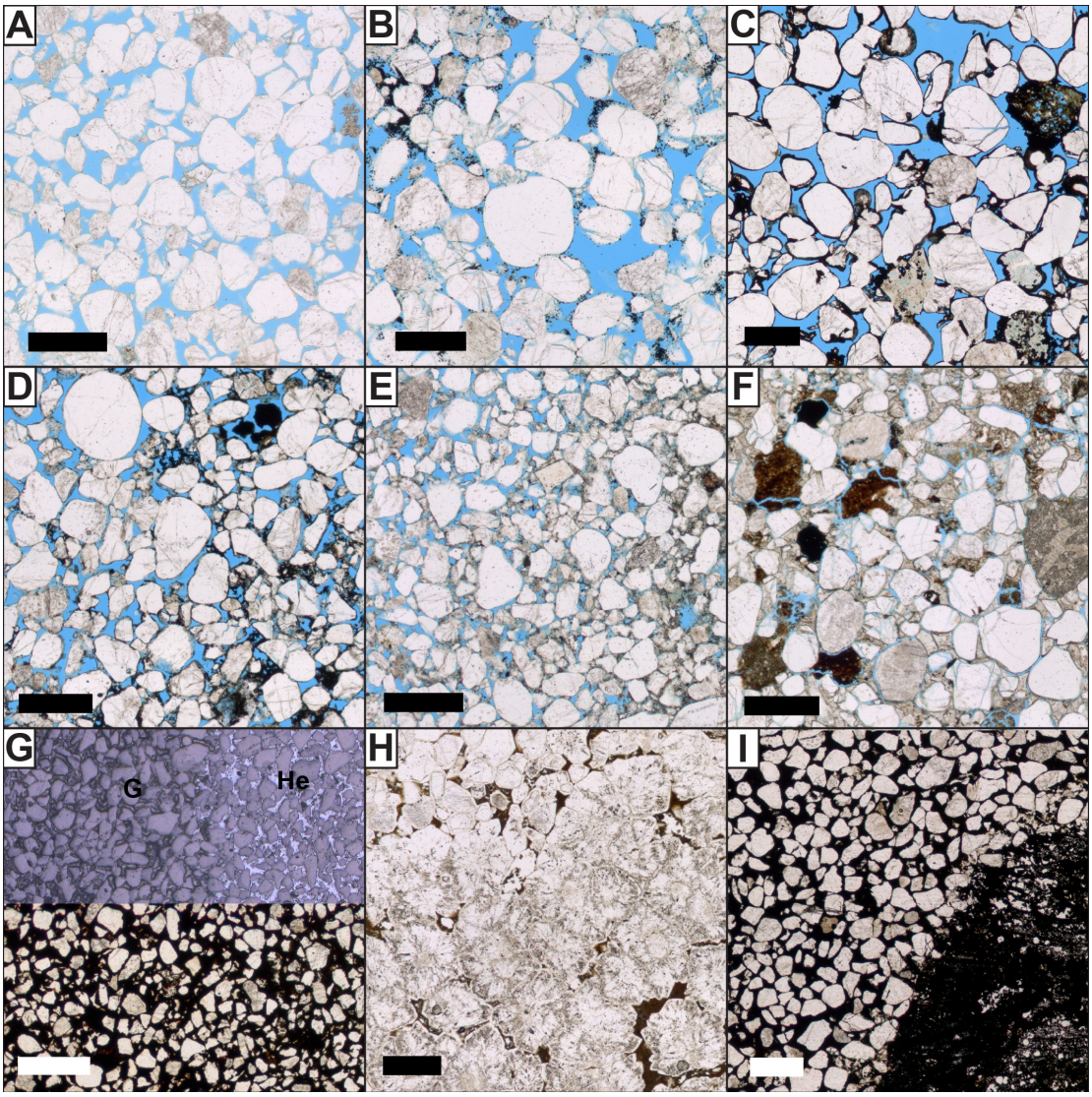

Figure 18. Photomicrographs of representative thin sections selected for detailed analysis (see Tables F.1A through F.1C) showing (A) white coloration, (B) purple coloration, (C) yellow-brown coloration, (D) red coloration, (E) red plus white coloration, (F) red coloration with carbonate cement, (G) massive digitate ironstone horizon type (note reflected light image [top]) overlain on plane-polarized transmitted light image (bottom) with continuous field of view in the frame to show change in iron oxide (G = goethite, He = hematite), (H) silica-replaced plant fragment (*Tempskya*(?) and quartz overgrowths in the surrounding sandstone matrix, and (I) center of spherical concretion with iron-replaced wood (iron-bearing, mineral-replaced wood [lower right]) with surrounding pyrite-cemented sandstone). Scale bars = 0.5 mm.

long contacts. Most samples contain lithic fragments and/or feldspar grains that exhibit a low to moderate degree of dissolution and replacement by minerals with low birefringence. Meniscus cements are most common among all samples and occur at point and long grain contacts. The cements of white and lower red sandstone samples commonly exhibit low birefringence and uniform texture, with some examples in optical continuity with one of the adjacent quartz grains. Upper red sandstone member samples contain cements with very high birefringence (up to 3rd order) that occlude the pore space and exhibit a poikilotopic fabric with individual crystal domains enveloping up to two to three framework grains. Circumgranular cracking (open

spaces surrounding grains) provided open pore space, occupied by a second-generation grain coating mineral (possibly carbonate).

Grain contact and lithic deformation observations in thin section can be used to characterize the degree of compaction experienced by the Baseline Sandstone. Overall, sandstone beds of the Baseline have experienced light to moderate compaction, as indicated by the prevalence of point and long contacts. Samples that come from lower stratigraphic horizons with predominately long contacts and incipient concavo-convex contacts suggest a higher degree of compaction. The prevalence of "floating" grains within cementation facies indicates that cementation occurred early, prior to significant compaction and lithification.

The thin section observations lead to an interpretation of a general sequence of eogenetic (early), mesogenetic (middle), and telogenetic (late) post-depositional changes (Choquette and Pray, 1970; Worden and Burley, 2003) that can be integrated with timing observations made at the larger field scales to produce a generalized paragenetic sequence (Figure 19). Crosscutting relations between quartz(?) meniscus cements and grain-coating minerals indicate that purple coloration likely formed prior to any significant cementation and compaction. Other coloration facies probably formed after the generation of meniscus cements and likely from remobilization of iron minerals (detrital or other early iron oxide grain coats) that formed earlier. From the thin section observations, it is unclear if the white coloration is a result of later bleaching of the sandstone or if grain coats just did not form in those sandstone units. However, given the red-colored Jurassic-Triassic source rocks for the Baseline Sandstone, and that the transport distance was less than 10 km (see Figure 1C), the post-depositional bleaching origin is most likely. The floating grains in the cementation facies indicate that cementation occurred prior to compaction, possibly during eogenesis.

For the bulk of the cementation facies of the Baseline Sandstone, it is possible that iron oxide was the original phase precipitated; however, for some samples (e.g., pyrite-cored concretions of Figures 9C and 18I) pyrite was likely the original phase precipitated with later oxidation to hematite plus goethite/other oxyhydroxides. Given the open pore network in many of the coloration facies, it is possible that an early cement phase (e.g., carbonate, see Loope et al., 2012) maintained the framework grain spacing through compaction but was later removed through bleaching during later alteration. The carbonate cements of the upper red sandstone member host-lithology likely formed during eogenesis from Cretaceous soil-forming processes superimposed on the isolated-channel sandy alluvial plain strata (Figure 13). The source of constituent ions was either from degradation of carbonate lithic fragments, which are more abundant in this stratigraphic interval (see point-count results in Duncan, 2022) or from soil-forming processes as part of the alluvial plain environment (Worden and Burley, 2003).

(U-Th)/He Dating of Iron Oxides

Ages for ironstone horizon and concretionary type iron oxides returned ages ranging from 26.68 to 19.35 ± 0.52 Ma (Figure 4A). The apparent young absolute ages of the samples, aside from the Baseline fault sample, are inconsistent with crosscutting field relations. The broad-scale patterns in diagenetic minerals, crosscutting relations between diagenetic features and structural features, and the apparent close affinity between iron oxide concretionary forms and fossil wood fragments collectively indicate that the main phase of iron oxide diagenetic alteration must have occurred very soon after deposition (within up to 20 to 10 Ma, the likely upper time limit that non-mineralized fossil wood fragments might remain; see Mustoe, 2018). Thus, the young absolute-ages measured here suggest issues of open-system behavior of the (U-Th)/He system, sensitivity to alteration and low closure temperatures of the small crystals of iron oxides, or the sample ages indicate a common oxidation/alteration age or closure age (see Fox and Shuster, 2014; Reiners et al., 2014; Ault et al., 2020). The sample from the crystalline iron oxides found along the Baseline fault returned ages of 5.26 to 5.05 ± 0.22 Ma that possibly reflect the formation age of the fault plane-coating oxides about 7 to 5 Ma, but at least provides a lower bound (i.e., youngest) age constraint on the fluid-flow alteration along the Baseline fault. More samples and analyses would be required to further resolve the absolute authigenic mineral ages.

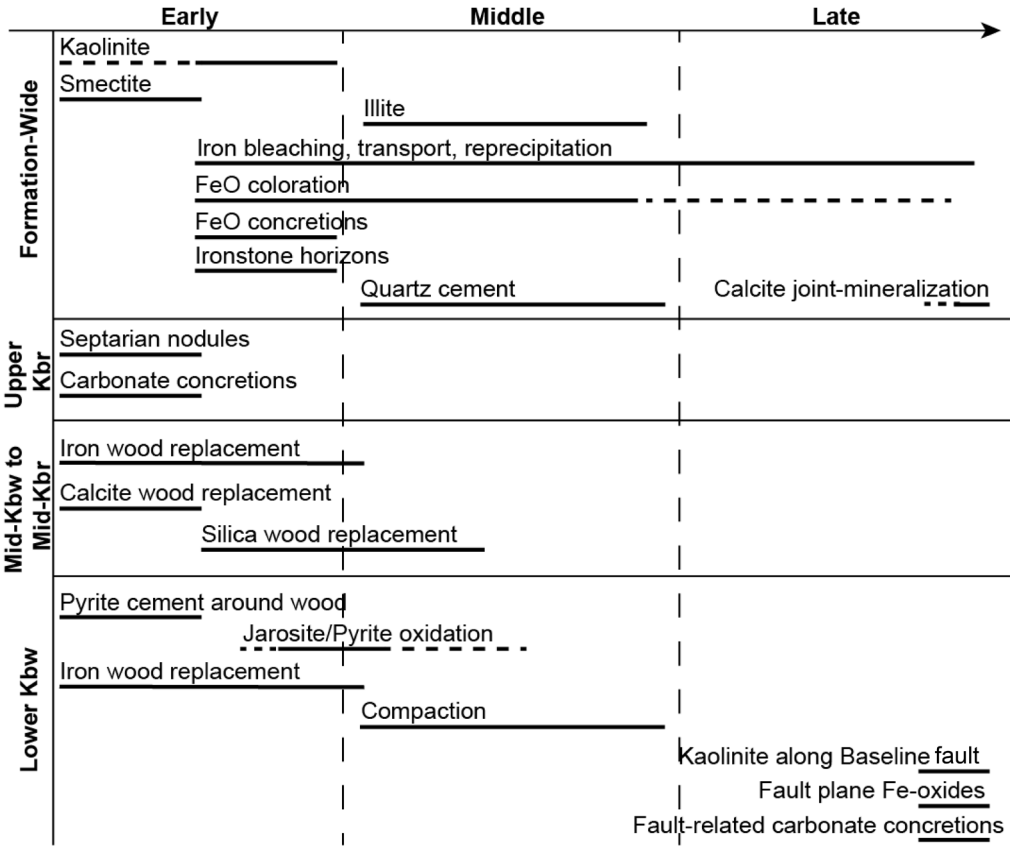

Figure 19. Paragenetic timeline for the Baseline Sandstone. Observations pertinent to the formation as a whole are shown at the top, and observations related to diagenetic attributes of specific stratigraphic intervals (organized by stratigraphic position) are shown in the lower half of the diagram.

DISCUSSION

The observed diagenetic mineral occurrences and their relations reveal distinct episodes of fluid flow-driven alteration, controlled by stratigraphic and structural attributes, on the syn- and post-depositional history of the Baseline Sandstone.

Paragenesis

Stratigraphic characterization of the Baseline Sandstone records the inception, advance, retreat, and demise of an alluvial to fluvial fan shed from the uplifted block of the Willow Tank thrust (Duncan, 2022). This foreland basin history and resulting change in depositional environments, along with the great thickness about 1 km) of the Baseline Sandstone and structural overprints (particularly the hanging wall vs. footwall of the Baseline fault) within the foreland basin history, means that discussion of the diagenetic stages requires consideration of results from multi-method and multi-scale workflows. This discussion outlines eogenetic (early), mesogenetic (middle), and telogenetic (late) stages reflected in the diagenetic evolution of the Baseline Sandstone deposits and summarized in the paragenetic timeline of Figure 20.

Eogenesis

The early diagenetic realm is defined by those processes that occur at the sediment surface or at shallow depths and are driven largely by pore-fluid chemistry controlled by the depositional setting and meteoric fluid input (Worden and Burley, 2003). Eogenetic features relate to the broad depositional phases and spatial trends of the Baseline Sandstone as determined by the stratigraphic analysis and documentation of diagenetic mineral distribution (Duncan, 2022; Figures 12 and 13). Concretionary forms (e.g., pyrite nodules, possible carbonate(?) cements that maintained open grain spacing) throughout the formation seem to indicate overall redox conditions involved in eogenetic processes related to the depositional environment. These diagenetic mineral products set the stage for later alteration through burial and uplift, since the distribution of depositional

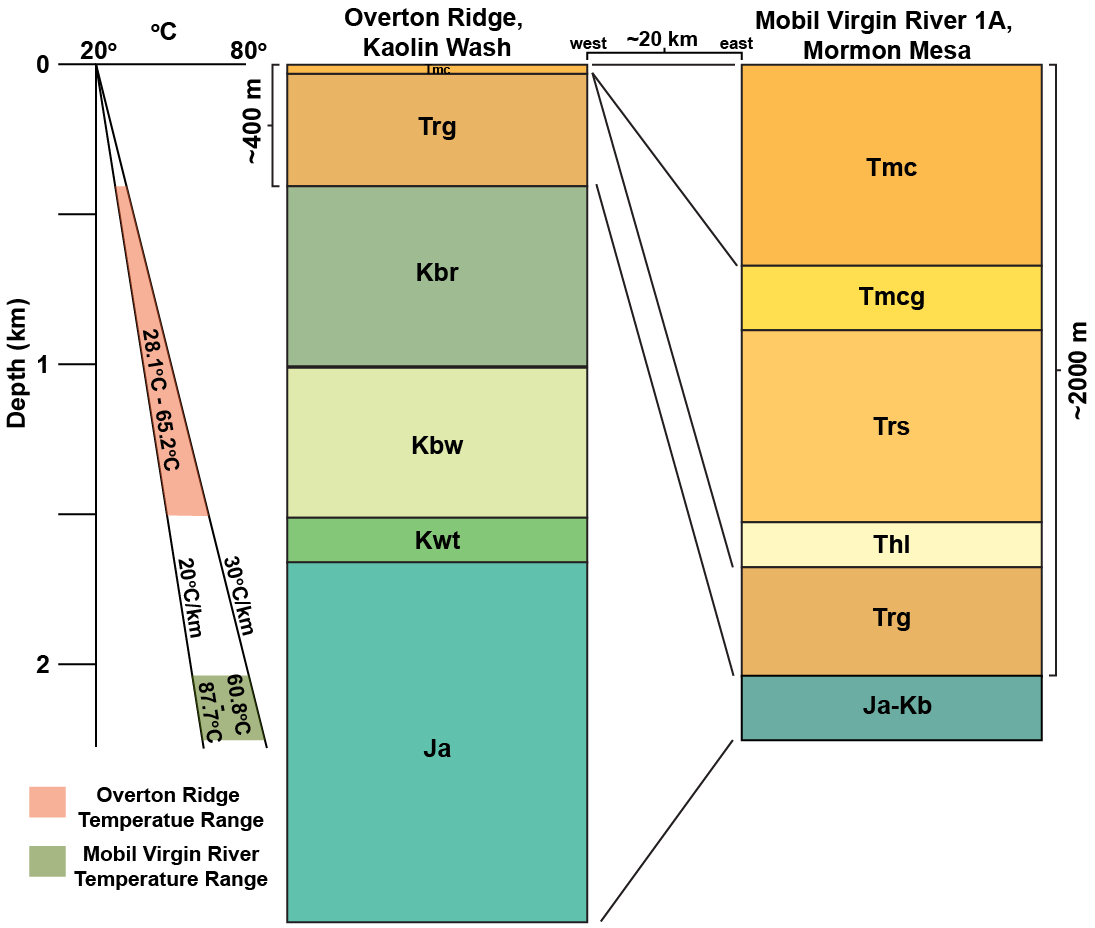

Figure 20. Stratigraphic column from Overton Ridge (data from Muntean, 2013), and the Mobil Virgin River No. 1A well at Mormon Mesa (data from Bohannon et al., 1993). Temperature ranges for the Baseline Sandstone are shown on the left for the section at Overton Ridge (shaded red wedge) and Mormon Mesa (shaded green wedge) calculated with depth and assuming a geothermal gradient range of 20° to 30°C. Stratigraphic units (also see Figure 1C): Ja = Jurassic Aztec Sandstone, Kwt = Cretaceous Willow Tank Formation, Kbw = Cretaceous Baseline Sandstone, white sandstone member, Kbr = Cretaceous Baseline Sandstone, red sandstone member, Trg = Tertiary Horse Spring Formation, Rainbow Gardens Member, Ja-Kb = Jurassic Aztec and Cretaceous Baseline undivided, Thl = Tertiary Horse Spring Formation, Lovell Wash Member, Trs = Tertiary red sandstone unit, Tmcg = Tertiary Muddy Creek Formation, gypsiferous part, Tmc = Tertiary Muddy Creek Formation.

facies influences the type and distribution of diagenetic alteration (Morad et al., 2010).

The principal stratigraphic parts of the Baseline Sandstone showing distinctive characteristics related to the diagenetic processes are the lower white sandstone member, the middle white sandstone member to middle red sandstone member, and the upper red sandstone member (Figure 19). The lower white sandstone was likely deposited in an alluvial plain environment, with alluvial fan processes dominant proximal to the Willow Tank thrust trace (Figures 12 and 13). The occurrence of pyrite-cemented spheroidal concretions suggests that the environment was reducing overall, possibly because of rapid burial or oxidation of organic material (fossil wood and plant fragments) in the floodplain sediments (Worden and Burley, 2003). The iron oxide layer ironstone horizons might have been areas of localized ponds within the alluvial plain environment, where iron oxide (or precursor mineral) spherules precipitated and accumulated at the pond bottom. The middle white sandstone to middle red sandstone include deposits of a fluvial fan environment (Moscariello, 2018),

where sheetfloods and stream flow acted as the dominant depositional processes. It is likely that this depositional environment was oxidizing overall, with meteoric infiltration through unsaturated sediments above the water table. The upper red sandstone member records a return to a fluvial depositional environment as activity ceased on the Willow Tank thrust and the fan retreated as weathering of the relict topographic high proceeded. This environment likely involved a greater amount of microbial activity within the sediment profile, pedogenic processes within floodplain sediments, and overall lower availability of oxygen due to oxidation of organic material in the sediment (Worden and Burley, 2003).

Deposition of the Baseline Sandstone occurred during the highest atmospheric partial pressure of carbon dioxide (pCO_2) concentrations of the Cretaceous Period, up to about 1500 ppm, which led to a peak in temperatures in the Cenomanian-Turonian (Hong and Lee, 2012) in the overall greenhouse climate of the Cretaceous Thermal Maximum (Huber et al., 2018). Due to this sub-tropical to tropical climate in North America, precipitation rates were much higher than they are today, with mid-latitude areas receiving about 3.6 times present rates (Ufnar et al., 2008). However, due to atmospheric and Western Interior seaway circulation patterns, it is likely that the eastern margin of the seaway received more precipitation than the western margin (White et al., 2001) at the location of the field area. Therefore, the climate of the Cretaceous in the field area during deposition of the Baseline would have been much warmer and wetter than the current arid conditions. The increased temperature, humidity, and pCO_2 conditions are important to consider for the eogenetic processes active within the sediment. These conditions may have led to increased chemical weathering rates through lower pH of rainwater (Bogan et al., 2009) and/or increased meteoric infiltration. These processes could possibly even include the formation of laterites and ferricretes or features characteristic of oxisols (U.S. Soil Survey, 1999). However, we identified very few clear soil profiles in this study of the Baseline (within the upper red sandstone member), so usage of soil profile names here are only for the purpose of communicating the likely processes and results brought about by the paleoclimate in the eogenetic realm.

Mesogenesis

The mesogenetic realm includes those processes that occur upon burial and isolation of the sediment from surface processes and meteoric fluid infiltration, or at burial depths of 1 to 2 km (Worden and Burley, 2003). Due to the relatively coarse-grained nature of the Baseline Sandstone, and the relatively shallow to moderate burial (less than about 400 m for the formation top, up to about 1460 m for the formation base; Figure 20), it is possible that meteoric/surface water infiltration continued through burial. As a result, only the lowermost part of the Baseline had possibly reached sufficient depths to be considered within the typical mesogenetic burial. Therefore, the mesogenetic realm of the Baseline is marked by the onset of progressive deposition by the stratigraphically higher parts of the Baseline itself, and structural deformation and tilting from the Laramide deformation from the formation of the Kingman arch.

Progressive deposition and burial of the Baseline Sandstone resulted in compaction and cementation that reduced overall porosity and permeability for stratigraphically lower parts of the formation. Compaction effects indicated by dominant grain contact types from base to top: concavo-convex contacts with deformed lithic grains, long contacts and point contacts indicate only a moderate degree of compaction of the stratigraphically lowest part of the formation. A general porosity degradation trend of about 5% per km for the lower white sandstone member through middle red sandstone member is likely due to these compaction effects (as determined through porosity characterization; see Duncan, 2022). In contrast, the overall lower porosity in the upper red sandstone is due to the greater abundance of early carbonate cement and carbonate concretions.

Processes related to burial, most notably compaction and cementation, are governed by the maximum burial depth of the formation and the resultant increased temperature and pressure conditions. The illite clay minerals identified in XRD analysis likely formed within the mesogenetic realm (Worden and Burley, 2003). It is unclear if the Baseline Sandstone was buried by any Cretaceous-Oligocene aged sediments given the nearly 70 Ma unconformity between the red sandstone

member and the Miocene Rainbow Gardens Member of the Horse Spring Formation. The area either remained a zone of sediment bypass for that time as the relict Sevier highlands eroded, or additional sediments were deposited atop the formation and were subsequently stripped away before the onset of Miocene deposition.

As an alternative scenario, the later backward shift in thrust fault activity to the Muddy Mountains thrust may have resulted in the emplacement of the Muddy Mountain thrust allochthon over the Baseline Sandstone, covering/shielding the deposits from erosion and increasing the overall burial depth. The thickness of the allochthon is likely about 2 km (Beard et al., 2007), meaning that if the thrust overrode the foreland basin deposits (Willow Tank and Baseline Formations) the effective burial would have been up to 2 km more than the present estimate. Observations of the degree of compaction obtained from thin sections do not seem to indicate a high degree of compaction, but over pressurization of the Baseline Sandstone following thrust allochthon cover may account for the (apparent) lack of compaction (e.g., Wilkinson and Haszeldine, 2011; Ulmer-Scholle et al., 2016).

The Baseline Sandstone at the field area was tilted prior to deposition of Miocene-aged sediments, and progressive tilting increased the structural tilt of the formation throughout deposition during the Miocene (discussed below). Therefore, it is unclear what the true maximum vertical burial thickness of the Baseline is at this location. Correlation with Baseline deposits in the Mobil Virgin River No. 1A well drilled about 20 km to the east of the field area (Bohannon et al., 1993) show significant thickness changes. Tertiary units thicken from about 400 m thick at Overton Ridge in the field area to greater than 2000 m thick, whereas the Cretaceous Baseline and Willow Tank and the Jurassic Aztec strata thin drastically, likely due to structural thinning along Basin and Range detachment faults. Nevertheless, the stratigraphic thicknesses of younger formations allow for estimating what can be considered a maximum burial depth. Taking the maximum local thickness of the Tertiary Horse Spring and Muddy Creek Formations (together comprising about 400 m of lithified sedimentary rock) the top of the Baseline Sandstone at the location of the field area was likely buried about 400 m with the basal part of the Baseline then buried up to about 1460 m depth, corresponding to a temperature gradient of 28° to 65°C from top to bottom (Figure 20; assuming a geothermal gradient of 20° to 30°C/km). This temperature range seems consistent with the observed quartz cements and clay mineral cements (presence of kaolinite, absence of dickite), and that inferred for the top of the nearby/stratigraphically lower Aztec Sandstone (Eichhubl et al., 2004). However, it is possible that the geothermal gradient was elevated due to the basinal fluid flow (Bjørlykke, 1994) during the deposition of at least the lower white sandstone member through the middle red sandstone member.

The geothermal gradient could also vary spatially due to the high geothermal gradient of the Basin and Range Province, where locally, the geothermal gradient is as high as 80° to 120°C/km (Coolbaugh et al., 2005). The thermal history of the sediments could also have been influenced by local volcanic history and the magma systems that fed nearby volcanoes that erupted during the middle Cenozoic ignimbrite flareup (Best et al., 2009). These volcanic systems include the Eocene-Miocene (36 to 18 Ma) Indian Peak-Caliente Caldera complex and ignimbrite deposits (Best et al., 2013) presently about 100 km to the north or the Miocene (about 14 to 11 Ma) Hamblin-Cleopatra Volcano (Barker et al., 2012) about 25 km to the south along the north side of Lake Mead.

The Baseline Sandstone was likely subjected to a horizontal/basin ward temperature gradient as well as a vertical geothermal gradient. It is unclear if the Baseline in the field area was overridden/covered by the Willow Tank thrust allochthon, except for the part of the formation immediately adjacent to the thrust trace, which exhibits growth structures and progressive unconformities (Aschoff and Schmitt, 2008). Therefore, sediments of the white sandstone member proximal to the Willow Tank thrust trace may have experienced increased temperature and pressure conditions related to the emplacement of the thrust sheet in contrast to thrust-distal sediments. The eastward thickening of Tertiary strata means that the Baseline at Mormon Mesa (Figure 20) likely was subjected to temperatures about 60° to 90°C (at 20° to 30°C/km). However, it is possible that the temperatures were even higher related to increased

local geothermal gradients and increased fluid flow heat transfer since the formation is structurally thinned from extensive structural thinning and dissection from Basin and Range faults (Bohannon et al., 1993).

Telogenesis

The telogenetic realm includes the processes upon structural modification and uplift, subjecting sedimentary units to meteoric water infiltration unrelated to the host rock/sediment's original depositional environment/climate (Worden and Burley, 2003). For the Baseline Sandstone, the telogenetic realm includes three principal phases: Laramide folding and erosion, Basin and Range tilting and erosive beveling, and climate change during the Late Pliocene, as discussed below.

Laramide shortening resulted in the formation of the Kingman uplift south of the field area (Lamb et al., 2018), causing erosional stripping of about 4.5 km of Paleozoic-Mesozoic sedimentary rocks and exposing the Proterozoic core of the uplift (Herrington, 2000; Faulds et al., 2001). Crosscutting relations indicate the uplift formed at least partly contemporaneous with 73 to 64 Ma granitic intrusions and Paleocene-Eocene deposits of the west-southwestern Colorado Plateau margin (Faulds et al., 2001, and sources therein). It is possible that uplift deformation caused tilting and rotation of the rocks and structures along the flank of the structure, including the Baseline Sandstone, which may account for the change in strike toward the southwestern part of the field area (Figure 1C; Beard et al., 2007). However, it is unclear if the surrounding thrust faults (pre-Laramide structures) exhibit similar deformation (Bohannon, 1984), so it must remain only a possibility. However, the timing of the Kingman uplift and large magnitude erosion can be used to estimate the age of maximum burial depth of the Baseline bracketed to about 64 to 56 Ma, before potential uplift.

Basin and Range extension initiated in this area about 17 to 15 Ma (Wernicke et al., 1988; Lamb et al., 2018), producing large-magnitude extension and tilting of rocks, crosscutting the Sevier-Laramide structures, and foreland basin fill. Regionally, extension is on the order of about 60 km, as evidenced by the lateral translation of the Frenchman Mountain block on the eastern side of Las Vegas (Fryxell and Duebendorfer, 2005). Westward translation along half-graben Basin and Range normal faults in the northern block of the Lake Mead fault system (Beard et al., 2007), resulted in progressive tilting of the Baseline Sandstone and forming an about 25° dip disparity between the Baseline Sandstone plus the overlying Horse Spring and Muddy Creek Formations (Lamb et al., 2018). Concomitant erosive beveling produced the horizontal surface cutting at an angle through the formation (see the cross section from Muntean, 2013) upon which Quaternary sediments were deposited. During this period, meteoric fluids likely used the Baseline fault as a flow conduit to produce the observed bleaching and kaolinite within the fault hanging wall and crystalline hematite precipitation along the fault plane. The age of the most recent episode of this fluid flow can be constrained using (U-Th)/He age dating of the crystalline hematite to about 7 to 5 Ma (youngest possible age), contemporaneous with Muddy Creek Formation deposition (Dickinson et al., 2014).

The last observed mineralization to occur in the field area relates to regional climatic variability over late Miocene to Pleistocene time, contemporaneous with and subsequent to deposition of the Muddy Creek Formation (Brock and Buck, 2009; Dickinson et al., 2014). Carbonate minerals along joints and as pendant cements along the bases of some beds formed from meteoric fluids related to the "Savannah-like" environment (arid to semi-arid) conditions during deposition of the Muddy Creek Formation (Kowallis and Everett, 1986; Brock and Buck, 2009), or during more recent shifts in paleoclimate over the last about 2.8 million years (Brock and Buck, 2009). Further erosion and downcutting once again exposed the Baseline Sandstone at the surface, exposing it to direct meteoric fluid influx percolating through the rock and along joints and faults.

Sevier Orogeny Fluid Flow vs. Basin and Range Fluid Flow

Our work reveals two distinct episodes of fluid flow-driven diagenetic alteration: the first from Cretaceous Sevier orogeny related basinal fluids, and the second from Miocene meteoric infiltration that used the

Basin and Range-related Baseline fault as a flow conduit. The fluids likely had distinct chemistries, resulting in distinct mineralogical signatures. Broad fluid flow alteration patterns in the Baseline Sandstone relate to mineralization in the adjacent Aztec Sandstone exposed in Valley of Fire State Park, which exhibits striking and varied coloration that resulted from basinal fluids that flowed outward from underneath the fold and thrust belt (Eichhubl et al., 2004). The timing relations outlined for the Baseline Sandstone indicate that the iron oxide coloration and cementation patterns overlap in age with the alteration of the Aztec Sandstone, suggesting that they formed through the same fluid flow episode.

The large amount of iron-derived coloration and iron oxide cementation present in the Baseline Sandstone requires advective transport and mobilization of iron through the diagenetic evolution of the formation. However, advective flow for iron mineralization requires internal and external iron sources. Internal sources for the iron likely relate primarily to the sediment shed into the foreland basin as thrusting occurred, and, as petrographic analysis reveals (Duncan, 2022), sediment provenance shifted as the Willow Tank thrust fault evolved and progressively older sediments were eroded into in the hanging wall anticline producing an unroofing sequence (McNamara, 2010). In the white sandstone member, sediments were dominated by those derived from the Aztec Sandstone, a fairly quartz-rich unit with abundant iron oxide grain coats. Sediments presently eroded from the Aztec exhibit a red coloration, suggesting that the white sandstone member would have likely exhibited a similar original red coloration prior to later bleaching and mobilization/concentration or reprecipitation of iron within the member.

As progressive erosion exposed the lower Jurassic-Triassic rocks within the hanging wall anticline of the Willow Tank thrust (including continental red bed deposits of the Moenave/Kayenta, Chinle, and Moenkopi Formations; Beard et al., 2007), sediments derived from these formations contributed a greater share of those shed into the foreland basin. This shift in sediment proportion likely resulted in the overall red coloration of the red sandstone member, with the additional possibility that these formations contributed a greater amount of iron for later remobilization within the member. This shift in provenance may account for the observed disparity in iron oxide coloration and cementation abundance between the white sandstone and red sandstone members, indicating that, at least in part, the authigenic iron oxide coloration and cementation were originally derived from detrital components or iron oxide grain coats within the red sandstone.

External sources of iron related to the fluid chemistry that drove the alteration of the Baseline Sandstone. First, the iron may have been supplied simply by iron contained within the fluids, acquired from sources farther from the field area than those nearby. Second, the fluids may have flowed through the nearby iron-bearing Aztec Sandstone (or other Jurassic-Triassic units) resulting in iron enrichment before reaching the Baseline Sandstone where it precipitated. These two scenarios are not mutually exclusive and could have led to a sequential enrichment of iron in the fluids as they flowed outward from the thrust belt until they were either: (1) saturated with respect to hematite/goethite, or (2) undersaturated in iron but encountered localized oxidizing conditions in the Baseline. Indeed, a mixture of internal and external sources of iron, and multiple precipitation mechanisms likely operated on the precipitation of patterns of Baseline iron oxide minerals.

Alteration patterns along the trace of the Baseline fault suggest a separate, recent (about 7 to 5 Ma) episode of fluid flow-driven alteration. These patterns are possibly similar in origin to alteration observed along normal faults and detachment faults in the region (about 50 km to the north-northeast of the field area) that exhibit isotopic and trace element characteristics suggesting that meteoric fluids and hydrothermal fluids exploited the faults as flow conduits (Diehl et al., 2010). There, the rocks involved in faulting are primarily composed of Paleozoic carbonate deposits, resulting in focused dissolution and solution collapse of the carbonate rocks along the faults. The observed bleaching, kaolinite concentration, and hematite precipitation adjacent to and along the Baseline fault (focus area C on Figures 1B and 1C) primarily concentrated in the Baseline Sandstone in the hanging wall is likely of similar origin to this carbonate alteration as an expression of the same type of fault-conduit fluid flow that contributed to dissolution and solution collapse. However, instead of dissolution

of carbonate rocks, alteration from large volumes of CO_2-rich meteoric infiltration (see Diehl et al., 2010) resulted in alteration of sediments, precipitation of the crystalline hematite rosettes along the fault plane, and concentration of kaolinite within the hanging wall adjacent to the fault. This kaolinite concentration may be similar to kaolinite formation that can occur from subaerial exposure and meteoric/freshwater leaching (e.g., the reservoir sandstone of the Magnus oil field in the North Sea [Emery et al., 1990]).

CONCLUSIONS

The Cretaceous Baseline Sandstone provides an exceptional opportunity to examine mineralogically and morphologically diverse, well-exposed diagenetic mineral products across scales to reveal a complex history of fluid flow in continental alluvial/fluvial fan to fluvial foreland basin deposits. Through the combination of multi-scale field characterization, remote sensing validation, and analytical results, this study documents the occurrence and attributes of five broad coloration facies, five ironstone horizon types, and numerous varied iron oxide, carbonate, and silica concretionary forms. The diagenetic feature formation was controlled by aspects that relate to depositional structures and lithologic textures, geochemical evolution (influenced by organic material oxidation and reaction biomediation), and/or structural pathways for fluid flow (e.g., the Baseline fault). The diagenetic history with relative timing is summarized below and on Figure 19.

1. The alluvial/fluvial setting and weathering and erosion of Triassic-Jurassic source rocks in the Willow Tank thrust hanging wall anticline provided sediments that contained early iron oxide grain coats. After rapid deposition and burial, the bulk of diagenetic iron oxide-related alteration formed coloration facies during the eogenetic (early) realm, likely driven by fluid flow related to porous lithologies and crustal thickening of the Sevier orogeny.

2. During the mesogenetic stage of burial of up to about 1460 m at the base of the formation, moderate compaction effects and quartz cements formed followed by secondary remobilization of iron oxide grain-coating minerals causing additional coloration.

3. During the telogenetic realm, a secondary fluid-flow-driven alteration period, with fluids likely from meteoric infiltration, resulted in bleaching and kaolinite concentration in the white sandstone member and crystalline iron oxides in proximity to and along the Miocene-aged (Basin and Range) Baseline fault.

4. Latest carbonate mineralization (along joints and along bottom surfaces of some features) in the field area formed, were likely related to regional climatic changes since about 2.8 Ma.

The Baseline Sandstone records important diagenetic archives that provide insight into the basin-scale fluid flow during the Sevier orogeny and meteoric fluid influx along faults during Basin and Range extension. Diagenetic alteration of the Baseline occurred related to its complex structural and depositional history.

ACKNOWLEDGMENTS

This work is derived from the Ph.D. dissertation of C. Duncan at University of Utah who gratefully acknowledges the input and contributions of his committee members, including: Marjorie A. Chan (advisor), Brenda Bowen, John M. Bartley, William Brazelton (all four University of Utah), and James Schmitt (Montana State University). This work was supported by the contribution of many individuals at University of Utah that aided in fieldwork, granted generous access to instruments, and reviewed manuscripts or provided fruitful discussion and feedback. We thank Steven Fryberger (Independent, Fort Collins, Colorado) and Greg Nielsen (Weber State University) for their thorough review and helpful comments of our manuscript. We respectfully acknowledge that the land in which this work was carried out is the ancestral lands of the Basketmaker culture, the Pueblo People, and the Southern Paiute Indian Tribe. This project was generously supported by

the GDL Foundation (Austin, Texas), with partial funding from Geological Society of America and American Association of Petroleum Geologists.

REFERENCES

Abrams, M.L., Brown, D., Lepley, L., and Sadowski, R., 1983, Remote sensing for porphyry copper deposits in southern Arizona: Economic Geology, v. 78, 591–604.

Allen, J.R.L., 1983, Studies in fluviatile sedimentation—bars, bar-complexes and sandstone sheets (low-sinuosity braided streams) in the brownstones (L. Devonian), Welsh borders: Sedimentary Geology, v. 33, no. 4, p. 237–293, https://doi.org/10.1016/0037-0738(83)90076-3.

Aschoff, J.L., and Schmitt, J.G., 2008, Distinguishing syntectonic unconformity types to enhance analysis of growth strata—an example from the Cretaceous, southeastern Nevada, U.S.A.: Journal of Sedimentary Research, v. 78, p. 608–623, https://doi.org/10.2110/jsr.2008.069.

Ault, A.K., 2020, Hematite fault rock thermochronometry and textures inform fault zone processes: Journal of Structural Geology, v. 133, https://doi.org/10.1016/j.jsg.2020.104002.

Barker, D.S., Thompson, K.G., Smith, E.I., and McDowell, F.W., 2012, Disequilibrium crystal-liquid processes at Hamblin-Cleopatra volcano, Lake Mead area, Nevada: Journal of Volcanology and Geothermal Research, v. 237/238, p. 42–53, https://doi.org/10.1016/j.jvolgeores.2012.05.009.

Beard, L.S., Anderson, R.E., Block, D.L., Bohannon, R.G., Brady, R.J., Castor, S.B., Duebendorfer, E.M., Faulds, J.E., Felger, T.J., Howard, K.A., Kuntz, M.A., and Williams, V.S., 2007, Preliminary geologic map of the Lake Mead 30' x 60' quadrangle, Clark County, Nevada, and Mohave County, Arizona: U.S. Geological Survey Open-File Report 2007-1010, 109 p., 3 plates, scale 1:100,000, http://pubs.usgs.gov/of/2007/1010/.

Best, M.G., Barr, D.L., Christiansen, E.H., Gromme, S., Deino, A.L., and Tingey, D.G., 2009, The Great Basin Altiplano during the middle Cenozoic ignimbrite flareup—insights from volcanic rocks: International Geology Review, v. 51, no. 7/8, p. 589–633, https://doi.org/10.1080/00206810902867690.

Best, M.G., Christiansen, E.H., Deino, A.L., Gromme, S., Hart, G.L., and Tingey, D.G., 2013, The 36-18 Ma Indian Peak-Caliente ignimbrite field and calderas, southeastern Great Basin, USA—multicyclic super-eruptions: Geosphere, v. 9, no. 4, p. 864–950, https://doi.org/10.1130/GES00902.1.

Bishop, J.L., Lane, M.D., Dyar, M.D., and Brown, A.J., Reflectance and emission spectroscopy study of four groups of phyllosilicates—smectites, kaolinite-serpentines, chlorites, and micas: Clay Minerals, v. 43, p. 35–54, https://doi.org/10.1180/claymin.2008.043.1.03.

Bjørlykke, K., 1994, Fluid-flow processes and diagenesis in sedimentary basins, *in* Parnell, J., editor, Geofluids—origin, migration and evolution of fluids in sedimentary basins: Geological Society Special Publication No. 78, p. 127–140, https://doi.org/10.1144/GSL.SP.1994.078.01.11.

Bogan, R.A.J., Ohde, S., Arakaki, T., Morie, I., and McLeod, C.W., 2009, Changes in rainwater pH associated with increasing atmospheric carbon dioxide after the industrial revolution: Water, Air, and Soil Pollution, v. 196, p. 263–271, https://doi.org/10.1007/s11270-008-9774-0.

Bohannon, R.G., 1983, Mesozoic and Cenozoic tectonic development of the Muddy, North Muddy, and northern Black Mountains, Clark County, Nevada: Geological Society of America Memoirs, v. 157, p. 125–148.

Bohannon, R.G., 1984, Nonmarine sedimentary rocks of Tertiary age in the Lake Mead region, southeastern Nevada and northwestern Arizona: U.S. Geological Survey Professional Paper 1259, 72 p.

Bohannon, R.G., 1992, Geologic map of the Weiser Ridge Quadrangle, Clark County, Nevada: U.S. Geological Survey Geologic Quadrangle Map 1714, scale 1:24,000.

Bohannon, R.G., Grow, J.A., Miller, J.J., and Blank, R.H., Jr., 1993, Seismic stratigraphy and tectonic development of Virgin River depression and associated basins, southeastern Nevada and northwestern Arizona: Geological Society of America Bulletin, v. 105, p. 501–520.

Bowen, B.B., Bell, J., and Story, S., 2012, Remote and field-based imaging spectroscopy for the diagenetic mineralogy of sedimentary rocks, *in* Sylvester, P., editor, Quantitative mineralogy and microanalysis of sediments and sedimentary rocks: Mineralogical Association of Canada Short Course 42, p. 115–132.

Brock, A.L., and Buck, B.J., 2009, Polygenetic development of the Mormon Mesa, NV petrocalcic horizons—geomorphic and paleoenvironmental interpretations: Catena, v. 77, p. 65–75, https://doi.org/10.1016/j.catena.2008.12.008.

Cady, S.L., Farmer, J.D., Grotzinger, J.P., Schopf, J.W., and Steele, A., 2003, Morphological biosignatures and the search for life on Mars: Astrobiology, v. 3, no. 2, p. 351–368.

Carpenter, D.G., 1989, Geology of the north Muddy Mountains, Clark County, Nevada and regional structural synthesis—fold-thrust and basin-range structure in southern Nevada, southwest Utah, and northwest Arizona: Corvallis, Oregon State University, M.S. thesis, 154 p.

Choquette, P.W., and Pray, L.C., 1970, Geologic nomenclature and classification of porosity in sedimentary carbonates: American Association of Petroleum Geologists Bulletin, v. 54, no. 2, p. 207–250.

Coolbaugh, M., Zehner, R., Kreemer, C., Blackwell, D., Oppliger, G., Sawatzky, D., Blewitt, G., Pancha, A., Richards, M., Helm-Clark, C., Shevenell, L., Raines, G., Johnson, G., Minor, T., and Boyd, T., 2005, Geothermal potential map of the Great Basin region, Western United States: Nevada Bureau of Mines and Geology Map 151, scale 1:1,000,000.

Crafford, A.E.J., 2007, Geologic map of Nevada: U.S. Geological Survey Data Series 249, 1 CD-ROM, 46 p., 1 plate, scale: 1:250,000.

Crafford, A.E.J., 2008, Paleozoic tectonic domains of Nevada—an interpretive discussion to accompany the geologic map of Nevada: Geosphere, v. 4, no. 1, p. 260–291, https://doi.org/10.1130/GES00108.1.

Davis, J.M., Wilson, J.L., Phillips, F.M., and Gotkowitz, M.B., 1997, Relationship between fluvial bounding surfaces and the permeability correlation structure: Water Resources Research, v. 33, no. 8, p. 1843–1854.

Deaton, B.C., 1987, Quantification of rock color from Munsell chips—research method paper: Journal of Sedimentary Petrology, v. 57, no. 4, p. 774–776.

DeCelles, P.G., 2012, Foreland basin systems revisited—variations in response to tectonic settings, *in* Busby, C., and Azor, A., editors, Tectonics of sedimentary basins—recent advances: Blackwell Publishing, p. 405–426, https://doi.org/10.1002/9781444347166.ch20.

Dickinson, W.R., Karlstrom, K.E., Hanson, A.D., Gehrels, G.E, Pecha, M., Cather, S.M., and Kimbrough, D.L., 2014, Detrital-zircon U-Pb evidence precludes paleo-Colorado River sediment in the exposed Muddy Creek Formation of the Virgin River depression: Geosphere, v. 10, no. 6, p. 1123–1138, https://doi.org/10.1130/GES01097.1.

Diehl, S.F., Anderson, R.E., and Humphrey, J.D., 2010, Fluid flow, solution collapse, and massive dissolution at detachment faults, Mormon Mountains, Nevada, *in* Umhoefer, P.J., Beard, L.S., and Lamb, M.A., editors, Miocene tectonics of the Lake Mead region, central Basin and Range: Geological Society of America Special Paper 463, p. 427–441, https://doi.org/10.1130/2010.2463(19).

Ducart, D.F., Silva, A.M., Toledo, C.L.B., and de Assis, L.M, 2016, Mapping iron oxides with Landsat-8/OLI and EO-1/Hyperion imagery from the Serra Norte iron deposits in the Carjas Mineral Province, Brazil: Brazilian Journal of Geology, v. 46, no. 3, p. 331–349, https://doi.org/10.1590/2317-4889201620160023.

Duncan, C.J., 2022, Stratigraphic, structural, and biologic controls on iron oxide diagenesis of the Cretaceous Baseline Sandstone, southern Nevada: Salt Lake City, University of Utah, Ph.D. dissertation, 456 p.

Ehrenberg, S.N., Aagaard, P., Wilson, M.J., Fraser, A.R., and Duthie, D.M.L., 1993, Depth-dependent transformation of kaolinite to dickite in sandstones of the Norwegian continental shelf: Clay Minerals, v. 28, no. 3, p. 325–352, https://doi.org/10.1180/claymin.1993.028.3.01.

Eichhubl, P., Taylor, W.L., Pollard, D.D., and Aydin, A., 2004, Paleo-fluid flow and deformation in the Aztec Sandstone at the Valley of Fire, Nevada—evidence for the coupling of hydrogeologic, diagenetic, and tectonic processes: Geological Society of America Bulletin, v. 116, no. 9/10, p. 1120–113, https://doi.org/10.1130/B25446.1.

Emery, D., Myers, K.J., and Young, R., 1990, Ancient subaerial exposure and freshwater leaching in sandstones: Geology, v. 18, p. 1178–1181.

Faulds, J.E., Feuerbach, D.L., Miller, C.F., and Smith, E.I., 2001, Cenozoic evolution of the northern Colorado River extensional corridor, southern Nevada and northwest Arizona, *in* Erskine, M.C., Faulds, J.E., Bartley, J.M., and Rowely, P.D., editors, The geologic transition, High Plateaus to Great Basin, the Mackin symposium: Utah Geological Association Publication 30, p. 239–272.

Fillmore, R., 2011, Geological evolution of the Colorado Plateau of eastern Utah and western Colorado: Salt Lake City, University of Utah Press, 496 p.

Folk, R.L., Andrews, P.B., and Lewis, D.W., 1970, Detrital sedimentary rock classification and nomenclature for use in New Zealand: New Zealand Journal of Geology and Geophysics, v. 13, no. 4, p. 937–968, https://doi.org/10.1080/00288306.1970.10418211.

Fossen, H., Schultz, R.A., Shipton, Z.K., and Mair, K., 2007, Deformation bands in sandstone—a review: Journal of the Geological Society (London), v. 164, p. 755–769, https://doi.org/10.1144/0016-76492006-036.

Fossen, H., Soliva, R., Ballas, G., Trzaskos, B., Cavalcante, C., and Schultz, R.A., 2017, A review of deformation bands in reservoir sandstones—geometries, mechanisms and distribution, *in* Ashton, M., Dee, S.J., and Wennberg, O.P., edsitors, Subseismic-scale reservoir deformation: The Geological Society (London) Special Publication 459, p. 9–34, https://doi.org/10.1144/SP459.4.

Fox, M., and Shuster, D.L., 2014, The influence of burial heating on the (U-Th)/He system in apatite—Grand Canyon case study: Earth and Planetary Science Letters, v. 397, p. 174–183, https://doi.org/10.1016/j.epsl.2014.04.041.

Fryxell, J.E., and Duebendorfer, E.M., 2005, Origin and trajectory of the Frenchman Mountain block, an extensional allochthon in the Basin and Range Province, southern Nevada: Journal of Geology, v. 113, p. 355–371.

Fu, Y., Yang, Z., Li, C., and Xia, P., 2021, Enrichment of platinum group elements in lower Cambrian polymetallic black shale, SE Yangtze Block, China: Frontiers in Earth Science, v. 9, p. 1–13, https://doi.org/10.3389/feart.2021.651948.

Gaffey, S.J., 1986, Spectral reflectance of carbonate minerals in the visible and near infrared (0.35-2.55 microns)—calcite, aragonite, and dolomite: American Mineralogist, v. 71, p. 151–162.

Grove, C., and Jerram, D.A., 2011, jPOR—an ImageJ macro to quantify total optical porosity from blue-stained thin sections: Computers & Geosciences, v. 37, no. 11, p. 1850–1859, https://doi.org/10.1016/j.cageo.2011.03.002.

Herrington, J.M., 2000, Evolution of the Kingman arch, southern Nevada: Las Vegas, University of Nevada, M.S. thesis, 97 p.

Hodgson, D.M., Bernhardt, A., Clare, M.A., Da Silva, A-C., Fosdick, J.C., Mauz, B., Midtkandal, I., Owen, A., and Romans, B.W., 2018, Grand challenges (and great opportunities) in sedimentology, stratigraphy, and diagenesis research: Frontiers in Earth Science, v. 6, no. 173, p. 1–9, https://doi.org/10.3389/feart.2018.00173.

Hong, S.K., and Lee, Y.I., 2012, Evaluation of atmospheric carbon dioxide concentrations during the Cretaceous: Earth and Planetary Science Letters, v. 327/328, p. 23–28, https://doi.org/10.1016/j.epsl.2012.01.014.

Huber, B.T., MacLeod, K.G., Watkins, D.K., and Coffin, M.F., 2018, The rise and fall of the Cretaceous Hot Greenhouse climate: Global and Planetary Change, v. 167, p. 1–23, doi: https://doi.org/10.1016/j.gloplacha.2018.04.004.

Issen, K.A., and Rudnicki, J.W., 2000, Conditions for compaction bands in porous rock: Journal of Geophysical Research, v. 105, no. B9, p. 21,529–21,536.

Knepper, D.H., Jr., 2010, Distribution of potential hydrothermally altered rocks in central Colorado derived from Landsat Thematic Mapper Data—a geographic information system data set: U.S. Geological Survey Open-File Report 2010-1076, 14 p.

Kokaly, R.F., Clark, R.N., Swayze, G.A., Livo, K.E., Hoefen, T.M., Pearson, N.C., Wise, R.A., Benzel, W.M., Lowers, H.A., Driscoll, R.L., and Klein, A.J., 2017, USGS Spectral Library Version 7: U.S. Geological Survey Data Series 1035, 61 p., https://doi.org/10.3133/ds1035.

Kowallis, B.J., and Everett, B.H., 1986, Sedimentary environments of the Muddy Creek Formation near Mesquite, Nevada, *in* Griffen, D.T., and Phillips, W.R., editors, Thrusting and extensional structures and mineralization in the Beaver Dam Mountains, southwestern Utah: Utah Geological Association Publication 15, p. 69–75.

Lamb, M.A., Beard, L.S., Hickson, T., Umhoefer, P., Dunbar, N., Schleicher, J., and McIntosh, W., 2015, Late Oligocene—early Miocene landscape evolution of the Lake Mead region during the transition from Sevier contraction to Basin and Range extension: Geological Society of America Bulletin, v. 127, no. 7/8, p. 899–925, https://doi.org/10.1130/B31144.1.

Lamb, M.A., Beard, L.S., Dragos, M., Hanson, A.D., Hickson, T.A., Sitton, M., Umhoefer, P.J., Karlstrom, K.E., Dunbar, N., and McIntosh, W., 2018, Provenance and paleogeography of the 25-17 Ma Rainbow Gardens Formation—evidence for tectonic activity at ca. 19 Ma and internal drainage rather than throughgoing paleorivers on the southwestern Colorado Plateau: Geosphere, v. 14, no. 4, p. 1592–1617, https://doi.org/10.1130/GES01127.1.

Li, L., Maher, K., Navarre-Sitchler, A., Druhan, J., Meile, C., Lawrence, C., Moore, J., Perdrial, J., Sullivan, P., Thompson, A., Jin, L., Bolton, E.W., Brantley, S.L., Dietrich, W.E., Mayer, K.U., Steefel, C.I., Valocchi, A., Zachara, J., Kocar, B., Mcintosh, J., Tutolo, B.M., Kumar, M., Sonnenthal, E., Bao, C., and Beisman, J., 2017, Expanding the role of reactive transport models in critical zone processes: Earth-Science Reviews,

v. 165, p. 280–301, https://dx.doi.org/10.1016/j.earscirev.2016.09.001

Li, Z.X., Bogdanova, S.V., Collins, A.S., Davidson, A., De Waele, B., Ernst, R.E., Fitzsimons, I.C.W., Fuck, R.A., Gladkochub, D.P., Jacobs, J., Karlstrom, K.E., Lu, S., Natapov, L.M., Pease, V., Pisarevsky, S.A., Thrane, K., and Vernikovsky, V., 2008, Assembly, configuration, and break-up history of Rodinia—a synthesis: Precambrian Research, v. 160, p. 179–210, https://doi.org/10.1016/j.precamres.2007.04.021.

Longwell, C.R., 1949, Structure of the northern Muddy Mountain area, Nevada: Bulletin of the Geological Society of America, v. 60, p. 923–968.

Loope, D. B., Kettler, R.M., Weber, K.A., Hinrichs, N.L., and Burgess, D.T., 2012, Rinded iron-oxide concretions—hallmarks of altered siderite masses of both early and late diagenetic origin: Sedimentology, v. 59, p. 1769–1781, doi: https://doi.org/10.1111/j.1365-3091.2012.01325.x.

McKeown, N.K., Bishop, J.L., Cuadros, J., Hillier, S., Amador, E., Makarewicz, H.D., Parente, M., and Silver, E.A., 2011, Interpretation of reflectance spectra of clay mineral-silica mixtures—implications for Martian clay mineralogy at Mawrth Vallis: Clay and Clay Minerals, v. 59, no. 4, p. 400–415, https://doi.org/10.1346/CCMN.2011.0590404.

McLemore, V.T., Eveleth, R.W., Brandvold, L.A., and Robertson, J.M., 1989, Platinum-group metals in New Mexico: New Mexico Geology, v. 11, no. 2, p. 29–30.

McNamara, K.C., 2010, The influence of growing structures on Cretaceous alluvial systems along the Cordilleran thrust belt front, Valley of Fire, southern Nevada: Bozeman, Montana State University, M.S. thesis, 138 p.

Miall, A.D., 1996, The geology of fluvial deposits: New York, Springer-Verlag Berlin Heidelberg, 583 p.

Morad, S., Al-Ramadan, K., Ketzer, J.M., and De Ros, L.F., 2010, The impact of diagenesis on the heterogeneity of sandstone reservoirs—a review of the role of depositional facies and sequence stratigraphy: American Association of Petroleum Geologists Bulletin, v. 94, no. 8, p. 1267–1309, https://doi.org/10.1306/04211009178.

Moscariello, A., 2018, Alluvial and fluvial fans at the margins of continental sedimentary basins—geomorphic and sedimentological distinction for geo-energy exploration and development, *in* Ventra, D., and Clarke, L.E., editors, Geology and geomorphology of alluvial and fluvial fans—terrestrial and planetary perspectives: The Geological Society (London) Special Publications, v. 440, p. 215–243, https://doi.org/10.1144/SP440.11.

Muntean, T.W., 2013, Preliminary geologic map of the Valley of Fire East quadrangle, Clark County, Nevada: Nevada Bureau of Mines and Geology Open-File Report 13-6, scale 1:24,000.

Mustoe, G.E., 2018, Non-mineralized fossil wood: Geosciences, v. 8, no. 6, p. 1–30, https://doi.org/10.3390/geosciences8060223.

Nevada State Parks, 2021, History of Valley of Fire State Park: Online, http://parks.nv.gov/learn/park-histories/valley-of-fire-history, accessed October 2021.

Pour, A.B., and Hashim, M., 2015, Hydrothermal alteration mapping from Landsat-8 data, Sar Cheshmeh copper mining district, south-eastern Islamic Republic of Iran: Journal of Taibah University for Science, v. 9, p. 155–166, https://doi.org/10.1016/j.jtusci.2014.11.008.

Reiners, P.W., Chan, M.A., and Evenson, N.S., 2014, (U-Th)/He geochronology and chemical composition of diagenetic cement, concretions, and fracture-filling oxide minerals in Mesozoic sandstone of the Colorado Plateau: Geological Society of America Bulletin, v. 126, no. 9/10, p. 1363–1383, https://doi.org/10.1130/B30983.1.

Reiners, P.W., Carlson, R.W., Renne, P.R., Cooper, K.M., Granger, D.E., McLean, N.M., and Schoene, B., editors, 2017, Chapter 11—the (U-Th)/He system, *in* Geochronology and thermochronology, 1st edition: Hoboken, New Jersey, John Wiley & Sons, Inc., p. 291–363, https://doi.org/10.1002/9781118455876.ch11.

Roddaz, M., Hermoza, W., Mora, A., Baby, P., Parra, M., Christophoul, F., Brusset, S., and Espurt, N., 2010, Cenozoic sedimentary evolution of the Amazonian foreland basin system, *in* Hoorn, C., and Wesselingh, F.P., editors, Amazonia, landscape and species evolution—a look into the past: Chichester, West Sussex, United Kingdom, John Wiley & Sons Ltd, p. 61–88, doi: https://doi.org/10.1002/9781444306408.ch5.

Roy, D.P., Wulder, M.A., Loveland, T.R., Woodcock, C.E., Allen, R.G., Anderson, M.C., Helder, D., Irons, J.R., Johnson, D.M., Kennedy, R., Scambos, T.A., Schaaf, C.B., Schott, J.R., Sheng, Y., Vermote, E.F., Belward, A.S., Bindschadler, R., Cohen, W.B., Gao, F., Hipple, J.D., Hostert, P., Huntington, J., Justice, C.O., Kilic, A., Kovalskyy, V., Lee, Z.P., Lymburner, L., Masek, J.G., McCorkel, J., Shuai, Y., Trezza, R., Vogelmann, J., Wynne, R.H., and Zhu, Z., 2014, Landsat-8: Science and product vision for terres-

trial global change research: Remote Sensing of Environment, v. 145, p. 154–172, http://dx.doi.org/10.1016/j.rse.2014.02.001.

Sabins, F.F., 1999, Remote sensing for mineral exploration: Ore Geology Reviews, v. 14, p. 157–183, https://doi.org/10.1016/S0169-1368(99)00007-4.

Schmidt, V., and McDonald, D.A., 1979, The role of secondary porosity in the course of sandstone diagenesis, *in* Scholle, P.A., and Schluger, P.R., editors, Aspects of diagenesis: Society for Sedimentary Geology (SEPM) Special Publication 26, p. 175–208, https://doi.org/10.2110/pec.79.26.0175.

Simpson, M.P., and Rae, A.J., 2018, Short-wave infrared (SWIR) reflectance spectrometric characterization of clays from geothermal systems of the Taupō Volcanic Zone, New Zealand: Geothermics, v. 73, p. 74–90, https://doi.org/10.1016/j.geothermics.2018.01.006.

Tidwell, W.D., and Hebbert, N., 1992, Species of the Cretaceous tree fern *Tempskya* from Utah: International Journal of Plant Science, v. 153, no. 3, p. 513–528.

Ufnar, D.F., Ludvigson, G.A., González, L., and Gröcke, D.R., 2008, Precipitation rates and atmospheric heat transport during the Cenomanian warming in North America—estimates from a stable isotope mass-balance model: Palaeogeography, Palaeoclimatology, Palaeoecology, v. 266, p. 28–38, https://doi.org/10.1016/j.palaeo.2008.03.033.

Ulmer-Scholle, D.S., Scholle, P.A., Schieber, J., and Raine, R.J., 2016, A color guide to the petrography of sandstones, siltstones, shales, and associated rocks: American Association of Petroleum Geologists Memoir 109, 526 p.

U.S. Soil Survey, 1999, Soil taxonomy—a basic system of soil classification for making and interpreting soil surveys, 2nd edition: Natural Resources Conservation Services, 886 p.

Wernicke, B., Axen, G.J., and Snow, J.K., 1988, Basin and Range extensional tectonics at the latitude of Las Vegas, Nevada: Geological Society of America Bulletin, v. 100, p. 1738–1757.

White, T., González, L., Ludvigson, G., and Poulsen, C., 2001, Middle Cretaceous greenhouse hydrologic cycle of North America: Geology, v. 29, no. 4, p. 363–366, https://doi.org/10.1130/0091-7613(2001)029<0363:MCGHCO>2.0.CO;2.

Wilkinson, M., and Haszeldine, R.S., 2011, Oil charge preserves exceptional porosity in deeply buried, overpressured, sandstones—central North Sea, UK: Journal of the Geological Society, v. 168, no. 6, p. 1285–1295, https://doi.org/10.1144/0016-76492011-007.

Worden, R.H., and Burley, S.D., 2003, Sandstone diagenesis—the evolution of sand to stone, *in* Burley, S.D., and Worden, R.H., editors, Sandstone diagenesis—recent and ancient: Malden, Massachusetts, Blackwell Publishing Ltd, p. 1–44, https://doi.org/10.1002/9781444304459.ch.

Xiong, D., Azmy, K., and Blamey, N.J.F., 2016, Diagenesis and origin of calcite cement in the Flemish Pass Basin sandstone reservoir (Upper Jurassic)—implications for porosity development: Marine and Petroleum Geology, v. 70, p. 93–118, http://dx.doi.org/10.1016/j.marpetgeo.2015.11.013.

APPENDIX

Supplemental Information to Structural and Stratigraphic Controls on Clastic Diagenesis of the Cretaceous Baseline Sandstone, Southern Nevada, U.S.A.

INTRODUCTION

This supplemental Appendix includes additional details related to the methods employed in this work, and further details on the field, laboratory, and remote sensing results of the work. In addition, this file includes data tables and figures that expand on the methods and results. In particular, this supplement provides many of the important details for the remote sensing workflow and results. Methods are described first, followed by results, with supplemental figures provided at the end of the document.

METHODS

This section of the supplemental Appendix expands on the multi-scale research methods used in this study to characterize the diagenetic attributes of the Baseline Sandstone. The data was integrated across orbital- to pore-scales as detailed below in the basic order of approaches:

1. "Ground truth" fieldwork and reconnaissance-level mapping to provide general context for sampling.

2. Remote sensing evaluation of Landsat satellite multispectral scene (processed in ENVI and Esri Arc Map) that provided a larger-scale perspective.

3. Multiple laboratory analyses to constrain mineralogical and geochemical attributes of the diagenetic products.

Field-Based Methods

Facies Characterization

Field-based methods focused on categorization/mineralogy, characterization of relationships to structures and sedimentary structures, and documentation of overall stratigraphic and spatial distribution. This work was focused in three key focus areas (about 0.5 to 1 km by about 1.5 to 2.5 km) chosen to show representative features and relationships to stratigraphic and structural attributes of the formation (see Figure 1C):

1. A stratigraphic transect through the white sandstone member into the lowermost red sandstone member of the Baseline Sandstone exposed within the hanging wall block of the Baseline fault (diagenetic pattern focus area A).

2. A full-formation stratigraphic transect through the Baseline Sandstone exposed in the footwall block of the Baseline fault (diagenetic pattern focus area B).

3. A part of the trace of the Baseline fault (diagenetic pattern focus area C).

The focus areas were also described, generally, at outcrop scale to document diagenetic facies and lithofacies, and explore the relationships between the two facies and included documentation of facies cross-cutting relationships, co-occurrence, and preferred associations.

Eleven key outcrops were selected for outcrop- to bed-scale characterization to document more detailed contextual information, especially for samples collected for further analysis (Table A1). These key outcrops are mostly aligned with the focus areas but also include outcrops from key stratigraphic positions and locations throughout the study area. The diagenetic facies associated with the Baseline fault (diagenetic pattern focus area C of Figure 1C) were described along three transects, including sample collection and reflectance spectral profile measurement. Each key outcrop was characterized through the following workflow:

1. The outcrop was imaged with a digital camera and/or with a Gigapan mount to produce an

Table A1. Key outcrop context summary. Kbw = white sandstone member of the Baseline Sandstone and Kbr = red sandstone member of the Baseline. See Figure 1C for key outcrop locations.

Outcrop	Location	Significance
KO-1	Basal Kbw, Tearfault Mesa area	Within concretion-dominated zone within the hanging wall of Baseline fault
KO-2	Basal Kbw, Baseline Mesa area	Within concretion-dominated zone within the hanging wall of Baseline fault
KO-3	Basal Kbw, Tearfault Mesa area	Red coloration zone, associated with change to debris flow-dominated interval
KO-4	Middle Kbr	Iron oxide and silica concretion-bearing interval, just stratigraphically below alteration boundary
KO-5	Upper Kbw, Florence Wash area	Pipe/pod-like concretion forms and digitate concretion forms on cemented horizons/blocks, intense color
KO-6	Basal Kbr, Tearfault Mesa area	Lowermost Kbr of of the hanging wall of the Baseline fault, contains carbonate concretions of various forms
KO-7	Basal Kbr, Florence Wash area	Lowermost Kbr of the footwall of the Baseline fault, coloration mostly variegated, abundant rinded concretions
KO-8	Middle Kbr, Kaolin Wash	Section above the altered-unaltered transition, likely represents transition to different depositional regime (sandy meandering fluvial)
KO-9	Upper Kbr, below Overton Ridge	Uppermost Kbr of footwall of Baseline fault below Overton Ridge, goes through a cluster of isolated channel bodies
KO-10	Middle Kbw, Tearfault Mesa area	Middle Kbw along flank of Tearfault Mesa, intense yellow to yellow-brown coloration
KO-11	Upper Kbw(?), next to highway	Most distal (depositionally) exposure of Baseline Sandstone

outcrop panorama. Imagery was collected from a select vantage point that provided the best perspective (e.g., downdip view direction to reduce distortion of contacts and thicknesses).

2. The outcrop panorama was used to map out and annotate general lithofacies and diagenetic facies visible at a distance, and to plan out a sample collection strategy and measured section pathway.

3. A measured section was described through the key outcrop, at a resolution appropriate for the specific outcrop, but generally about 10 to 25 cm with key outcrop 6 measured at about 1 m resolution. Lithologic attributes, bed thicknesses, sedimentary structures, and diagenetic attributes were described.

4. Representative samples of each principal diagenetic facies (sandstone coloration and concretionary forms) were collected from along the measured section pathway, or from elsewhere in the outcrop with location recorded on the outcrop panorama.

Key outcrops 4 and 9 were also imaged using an Unmanned/Uncrewed Aircraft System (UAS, aka drone) to produce a high-resolution aerial imagery and three-dimensional digital outcrop models.

Description and documentation of diagenetic facies associated with the Baseline fault near Baseline Mesa (diagenetic focus area C of Figure 1C) were performed at formation to outcrop scales in order to understand coloration and concretionary occurrences in association with the fault. Qualitative field descriptions were made of diagenetic facies along the fault and their extent into the hanging wall and footwall blocks (up to about 100 m away from the fault trace). Three transects

were established along which samples were collected at four locations: fault distal footwall, fault proximal (within 1 to 2 m from the fault plane) footwall, fault proximal hanging wall, and fault distal hanging wall. A portable reflectance spectrometer was used to measure visible-near infrared reflectance (VNIR) spectra at each transect location and from representative coloration and concretionary facies along the fault and within the hanging wall and footwall blocks up to about 100 m away from the fault trace. In total, 197 spectra were measured at 92 different locations along the fault trace.

VNIR Reflectance Spectra

A Terraspec 4 portable VNIR spectrometer was used to measure reflectance spectral profiles of coloration and concretionary facies in situ and samples in the laboratory. Generally, multiple measurements were collected in four areas (two of which coincide with diagenetic pattern focus areas A and B of Figure 1C), with photographs and facies/sedimentologic context recorded for each measurement. The spectrometer was regularly calibrated using a Spectralon white reference calibration plate throughout the about 2 hours work time each day. A handheld Trimble differential GPS was used to document the location of each measurement within decimeter accuracy. Reflectance spectra were spline-corrected in post-processing and plotted to identify preferential spectral absorption features.

Measurements were collected in four key locations: (1) the diagenetic facies of the Aztec Sandstone in the adjacent Valley of Fire; (2) the stratigraphic path through the white sandstone member and lowermost red sandstone member near Tearfault Mesa (diagenetic pattern focus area A of Figure 1C); (3) the Baseline fault trace towards the southern part of field area (diagenetic pattern focus area C of Figure 1C); and (4) the alteration boundary in upper red sandstone.

Remote Sensing Methods

Qualitative patterns in diagenetic mineral occurrence and stratigraphic distribution from field studies were tested/validated through objective multispectral satellite mineral mapping (e.g., Sabins, 1999; Knepper, 2010; Pour and Hashim, 2015; Ducart et al., 2016). A Landsat 8 Operational Land Imager/Thermal Infrared Sensor (OLI/TIRS) scene was selected for lack of cloud cover over the study area and an acquisition date closely coincident with field reflectance spectral profile acquisition. The scene was processed in Environment for Visualizing Images software (ENVI) with correction for atmospheric absorption effects to gain surface reflectance, then clipped to a smaller region of interest around the Valley of Fire/Baseline Sandstone for easier processing and classification (see Figure A1).

Band Ratios and Compositing

A series of band ratios and threshold values were created to determine which bands and band ratios identified mineral occurrences consistent with field mapping (Table A2). Due to the possibility of absorption features from key diagenetic minerals, bands 2, 4, 5, 6, and 7 (corresponding to blue, red, near infrared, and two shortwave infrared wavelengths, respectively) were used to create band ratio maps and composites (Roy et al., 2014). Specific band ratios employed were based on other published work that worked well for the observed field mineralogies (e.g., Pour and Hashim, 2015). These ratios were calculated in ENVI through either simple band ratios (e.g., red divided by blue, i.e., bands 4/2) or through compound ratios (e.g., red plus shortwave-infrared 1 divided by near-infrared (or bands (4+6)/5)). Threshold values for specific ratios helped determine how well a specific band ratio identified a known diagenetic pattern.

Various band combinations and band ratio combinations were composited in ENVI to create map products: Red, Green, and Blue (RGB), and Color Infrared (CIR) custom band ratio composites, and composites following the methods of Abrams et al. (1983), Sabins (1999), Knepper (2010), and Pour and Hashim (2015). An iterative process helped refine which band ratios best highlight known diagenetic mineral patterns.

Classification

The band composite images were classified via supervised and unsupervised classification tools available in ArcMap. Before classification, the composites were

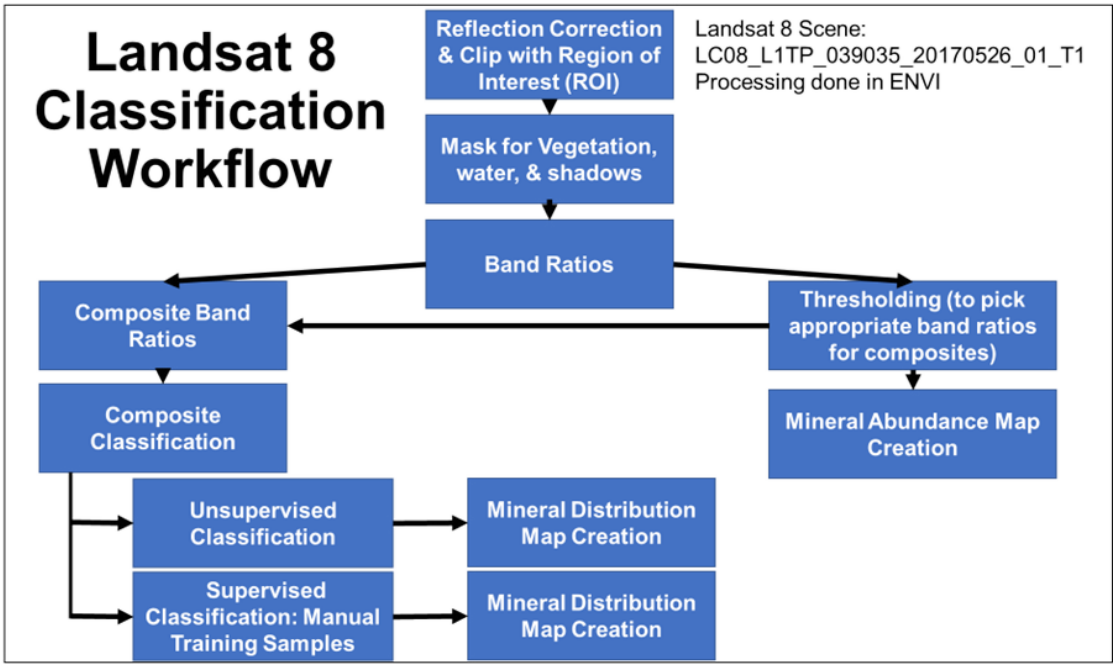

Figure A1. Summary remote sensing workflow schematic to produce derivative mineral maps.

masked to eliminate water, vegetation through Normal Difference Vegetation Index (NDVI), and shadows, to exclude the pixels containing those items in the classified maps and reduce subsequent computational requirements. Qualitative ground-truth observations from field characterizations were incorporated for the supervised classification through the use of nine main training classes, including soil types, bleached Aztec Sandstone, bleached Baseline Sandstone, clay-rich interval of the middle Willow Tank Formation, iron oxide with calcite, iron oxide rich, and anthropogenic influences as part of the adjacent Simplot Mine (see Figure A2 for map of areas that define training classes). Bleached Aztec and Baseline classes are those areas where iron oxide minerals have been mobilized and removed through redox processes. Through trial and error, it was determined that an unsupervised classification with 12 classes worked best, based on composite maps using band ratios after Abrams et al. (1983) with 6/7, 5/6, and 4/2 in the R, G, B channels, respectively.

Analytical Methods

Many representative samples (about 150 total) were collected of each diagenetic coloration and cementation facies for the diagenetic pattern focus areas, key outcrops, and Baseline fault characterization. Select samples were subjected to laboratory analysis to determine mineralogy of coloration and cementation facies mineralogy, bulk geochemical attributes, absolute age of the iron oxide cements, and crosscutting relationships between diagenetic minerals to determine the overall paragenetic sequence. For each analytical method, specific instrument, and processing details are provided below.

Thin Section Petrography

Standard dimension thin sections of 104 samples were prepared for transmitted-light petrographic microscopy. Several select samples were polished for reflected light studies and Scanning Electron Microscopy (SEM) or Quantitative Evaluation of Materials by Scanning Electron Microscopy (QEMSCAN) analyses. A portable reflectance spectrometer was used in the laboratory to measure reflectance spectral profiles for most of these thin section samples. Measured spectra were spline corrected and plotted to identify absorption features characteristic of the authigenic clay minerals and cements present. General observations for the bulk of the thin sections were collected, with nine key sam-

Table A2. Summary of band ratios, their purpose in the remote sensing workflow, and threshold values used in the mapping.

Band Ratio	Purpose	Threshold Values	
		Min	Max
(4/2)	Redness index- ferric iron oxide charge transfer absorption	1.015	2.000
(6/7)	Clays/carbonates, absorption features near 2.5 μm	1.070	2.000
(5/6)	Ferric iron oxide absorption feature	1.010	5.000
(4+6)/5	Ferric iron oxide crystal field absorption in band 5	2.080	2.000
(4/2)+((4+6)/5)	Iron oxide mapping	3.020	4.000

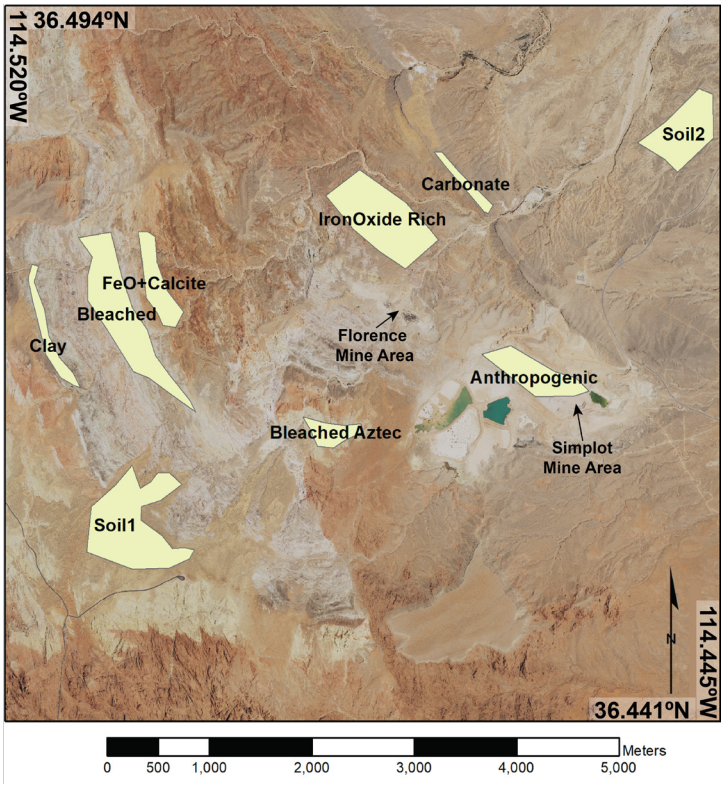

Figure A2. Training classes used for supervised classification as indicated by yellow polygons.

ples selected for detailed characterization (Tables A3A through A3C). This subset selection was chosen based on (1) representation of diagenetic facies, (2) overlap with other sample sets, if available (e.g., thin section MSS-L-4 is of the same sample of the white sandstone facies as powdered sample PS-10), and (3) data availability including images/mosaics, porosity estimates, etc.

Scanning Electron Microscopy

Representative samples of most diagenetic facies (21 total) were cut into an about 1-cm cube using a rock saw, and cut dry (no water for lubrication) to avoid any aqueous alteration. Each cube was then analyzed using an FEI Nova NanoSEM SEM equipped with an X-ray Energy Dispersive Spectrometer (EDS) to identify and characterize pore-filling cement mineral morphologies and their elemental abundances.

Powdered Sample Analyses: ICP-MS, XRD, and XRF

A total of 23 representative samples of coloration and cementation facies from the focus areas and key outcrops were analyzed using various geochemical tools (Table A4). Samples were chosen to (1) ensure representation of all coloration facies and cementation facies and (2) ensure spatial coverage throughout the formation. The samples were disaggregated by hand with a rock hammer, then lightly ground to a powder with a small quartz pestle and mortar. If possible, weakly cemented sandstone samples were ground until the rock was disaggregated, leaving the sand grains intact. Well-cemented concretion samples were ground until the sample was reduced to a fine powder. The bulk elemental concentration of 18 powdered samples was analyzed using a Thermo-Fisher Scientific Neptune Multicollector Inductively Coupled Plasma Mass Spectrometry (MC-ICP-MS). The identity of the clay-sized mineral fraction of 11 powdered samples was determined through glycolated and non-glycolated clay fraction X-ray diffraction (XRD) analysis. All powdered samples were analyzed with a Bruker hand-held X-ray fluorescence (XRF) spectrometer yielding qualitative elemental abundance results as a basis for comparison between the various diagenetic facies.

Table A3A. Summary of key thin section observations.

Sample	Grain Size (mm)	Sorting	Framework Grain Composition				Porosity		
			QFL	QmFLt	LvLmLs	LscLssCht	ImageJ Porosity (%)	jPORa Porosity (%)	Porosity Types
MSS-L-4 (white color, PS-10)	~0.05-0.53; avg 0.20	Well- to very well-sorted	94.5/3.8/1.7	92.6/4.2/3.2	25.0/75.0/0.0	0/0/100	16 ± 2%	19.6	Intergranular; minor dissolution of feldspar(?) grains; "open" framework of large pore spaces (but still smaller than individual grains)
MSS-L-2 (purple color, PS-9)	~0.04-0.73; avg 0.30	Moderately to well-sorted	95.2/1.0/3.8	92.7/1.16.2	6.3/68.8/25.0	0/50/50	18 ± 2%	21.4	Intergranular; intragranular (dissolution) --> either unstable lithics or feldspar grains (very low birefringence); some fractured quartz grains have FeO precipitates
MSS-L-6 (yellow color)	~0.05-0.75; avg 0.31	Moderately to well-sorted	94.2/1.8/4.0	92.4/2.0/5.7/	18.2/22.7/59.1	0/68.4/31.6	14 ± 2%	14	Intergranular primarily; minor fracture (though that could be sample prep); intragranular (dissolution) of unstable lithics (mudstone fragments, others)
MSS-L-8 (red color, PS-11)	~0.03-0.71; avg 0.18	Moderately sorted	91.5/4.0/4.6	87.0/4.1/8.9	25.9/33.3/40.7	0/35.5/64.5	21 ± 2%	15.9	Intergranular primarily; some fractured grains; minor dissolution of unstable lithics
MSS-L-15 (red + white, PS-14)	~0.02-0.55; avg 0.11	Moderately sorted	85.6/5.9/8.5	83.5/6.2/10.2	2.2/42.2/55.6	3.2/77.4/19.4	17 ± 2%	10.8	Predominately intergranular; minor intragranular in partially dissolved feldspars (x = 4000,y = 4000); open fracture on right side of slide ~0.17-0.62 mm wide
MSS-L-13 (carbonate cement, red color)	~0.03-0.55; avg 0.25	Moderately to well-sorted	84.9/1.6/13.5	80.7/1.7/17.7	1.2/15.3/83.5	23.5/60.0/16.5	6 ± 2%	5.1	Primarily intergranular, but located around grain boundaries --> circumgranular cracking? Indicative of soil or caliche formation; minor fracture porosity
Kbw-Ce-4 (FeO cement, FeO-replaced wood	Max average up to ~0.6, down to ~0.3 (similar lower bound to others)	Moderately sorted	No data	No data	No data	No data	No data	No data	Very little porosity throughout, filled w/ FeO; some fractured grains are also filled w/ FeO; concentric band of open pore space
Kbw-W-3 (silica-replaced plant fragment)	up to ~0.5; avg appears to be ~0.2	Moderately to well-sorted	No data	No data	No data	No data	No data	No data	Most pore space filled with quartz overgrowths or low birefringence material in upper right part; open pore spaces between silicified wood ("roses"); ~5-10% intergranular porosity; intraparticle porosity uncommon
Kbr-C-6 (ironstone horizon)	largest up to ~0.3 but that size is rare; average upper grain size up to ~0.23; visual average ~0.12	No data	No data	No data	No data	No data	No data	No data	Pore space completely filled throughout by FeO cements; ~5-10% iron cement; comparatively fewer fractured grains --> very low intragranular; cements occupy intergranular porosity; some pore spaces are large

[a]After Grove and Jerram (2011)

Table A3B. Summary of key thin section observations (conitnued).

Sample	Authigenic Componenets		
	Grain Coats	Cements	Replacement
MSS-L-4 (white color, PS-10)	Small (~0.5 µm) dark, opaque(?); common dark border to quartz grains (~0.5 µm thick)	Possibly quartz or kaolinite at grain contacts (low relief compared to quartz); possibly kaolinite; low birefringence; meniscus cements; one example of pore-bridging (possibly still meniscus)	Some grains exhibit slightly diffuse edges and interiors, possibly indicating partial replacement of feldspars by clays
MSS-L-2 (purple color, PS-9)	Very little (none apparent in x-pol); uneven/clustered distribution of ~5 µm FeO spheres	Possibly kaolinite cement, low birefringence and "patchy" appearance (could still be quartz cement); FeO spheres seem to preferentially occur coincident with partially dissolved grains; kaolinite or quartz cement; FeO spheres (<1% of the section) occur in enough abundance to fill the pore space	Some feldspar grains seem to be replaced with kaolinite; not very many dissolved grains, other sed lithics (Ss clast, chert grains) are not very altered
MSS-L-6 (yellow color)	Apparently all grains exhibit a fairly even coating of dark brown to black opaque crystals: ~3 µm thick, but variable thickness across slide; thickest in smaller pore spaces, fills pores where grains are close together; coats the outside and some inside pores of dissolved grains; dissolved lithics appear to contain more than dissolved feldspars	Meniscus cements, very low birefringence (δ=~0.002), most common along point contacts; open pore network; some small (close together) pores filled with FeO; meniscus cements only occur where grains are in contact and some grain contacts do not have clear (obvious) cements (possibly a 3D effect)	Blue-green clasts and lithic frags contain small high birefringent minerals (replacement by kaolinite?); unclear what the blue-green clasts are
MSS-L-8 (red color, PS-11)	Even grain coats ~2-3 µm thhick of FeO (hematite), thicker in small pore spaces; in progressively smaller pore spaces the FeO increased in concentration to nearly occlude pores	Similar to MSS-L-6, low birefringence and low relief cement at point contacts; meniscus cements; Ssome pores (~3-5%) are totally filled with FeO; Lithics/ Feldspars appear to be preferntial nucleation sites of FeO; FeO pore fill is amalgamation of the small crystals of FeO	Unstable lithics and/or feldspars show dissolution, possibly with FeO in the dissolved areas; some lithics have preferential FeO precipitated; possibly kaolinite replaceemnt of feldspar
MSS-L-15 (red + white, PS-14)	Dark gray high-birefringent (2nd-3rd order?), needle-like/rod-like ~20-30 µm in length --> irregularly distributed as a grain coat and pore-filling in some areas; semiplanar bands of this mineral where it is concentrated as a cement; "left" side of fracture coated with radiating dark brown, needle-like crystals	Predominant cement is the medium-brown, high birefringent mineral that coats grain surfaces throughout the sample; semiplanar (banded) fabric with cements most abundant; Cement may also occur where grains are close together (meniscus); fabric seems to be main control on cement distribution; possbily meniscus cements composed of low birefringent mineral (quartz, kaolinite)	Blue-green clasts contain high-birefringence minerals; possibly fully dissolved grain; partially dissolved lithic; iron staining
MSS-L-13 (carbonate cement, red color)	Dark rims on most grains (either mineral grain coat or high-relief edge?); appears that there is a second generation of calcite on the grain edge within the circumgranular crack space	Carbonate cements (likely calcite) fill pore spaces; appears to have a poikilotopic fabric, with individual crystal domains encompassing 2-3 sand grains; most crystal domains <~0.5 mm; largest aspect of a crystal domain = ~0.54 mm long (~0.075 mm wide); minor FeO cement	Replacement of unstable lithics or felspars by kaolinite; some grains appear to be replaced by FeO --> preferential replacement of lithics
Kbw-Ce-4 (FeO cement, FeO-replaced wood)	FeO grain coats in the pyrite-hematite boundary zone where pore-space appears to be open; other FeO grain coats in outer rim; brown-colored low birefringence mineral in rim, grain coating and pore-bridging in some areas, possibly FeO+clays (lllite?)	Bright reflection material fills pore spaces in zone adjacent to FeO-replaced wood --> pyrite, non-reflective material coats grains and formed along fractures; high-birefringence pore-filling material adjacent to pyrite, and open pore space; moderate reflection, pore-filling material with dim brown/purple in pore throats	High-birefringence material fills radial fracture that cuts across FeO cements and framework grains; wood frag replaced by dim and bright refelective material (goethite and pyrite?) --> possibly the same bright and dim material in the pyrite zone; very few lithics appear to be replaced with low birefringence material; cracks in pyrite zone might indicate secondary alteration of pyrite
Kbw-W-3 (silica-replaced plant fragment)	Dark grain coats indicate pre-quartz overgrowth edge; additional grain coats on the external border of quartz overgrowths (FeO and/or clays?); silica "roses" have a "concentric" (crystal edge paralleling) grain coat(?) near the edge	Quartz overgrowths that interlock (more well developed closer to "roses"); mottled low birefringence mineral cement in upper right part --> kaolinite or quartz cement; dark brown, but not opaque, possibly with high birefringence	Concentric structures or mottle cores to the "roses;" feldspar replaced by kaolinite(?)
Kbr-C-6 (ironstone horizon)	None visible between grains and cement; band of less well-cemented appears to have dark grain coats	Opaque cement that appears as platy brown to red-brown on thin exposures; less well-cemented band towards right side of slide; carbonate cement along bottom of sample --> caliche	Some grains (lithics or feldspars?) appear to have FeO (opaque) mineral replacement; unclear since XPL and reflected light images are unavailable

Table A3C. Summary of key thin section observations (continued).

Sample	Relationships	Grain Contacts/Compaction Attributes	Other
MSS-L-4 (white color, PS-10)	Unclear	Point and long-contacts most common, concavo-convex contacts present but less abundant; squashed lithic grains	n/a
MSS-L-2 (purple color, PS-9)	FeO spheres occur even along long and concavo-convex contacts; fractures filled with epoxy, some fractures also filled with FeO; dissolved grain with FeO spherules around outer surface but not interior	Point contacts; long-contacts common; concavo-convex	FeO formed prior to grain dissolution and spheres formed prior to compaction
MSS-L-6 (yellow color)	Meniscus cements prior to FeO grain coats; fractured grains prior to FeO grain coats; dissolution of feldspars and unstable lithics occurred prior to FeO grain coats or contemporaneous	Point and long contacts (long contacts are most common)	n/a
MSS-L-8 (red color, PS-11)	Meniscus cements formed prior to FeO grain coats --> likewise, pore-filling FeO likely filled after meniscus cements; feldspar and unstable lithics likely dissolved prior to or contemporaneous with FeO	Point contacts; long-contacts most common; possibly some concavo-convex	n/a
MSS-L-15 (red + white, PS-14)	Darker grain coats not preseint in between the low birefringent cment --> kaolinite/quartz cement prior to illite/smectite formation, dissolution of feldspars leading to precipitation of kaolinite?	Point and long contacts	Some grains (<<1%) exhibit a blue-green color
MSS-L-13 (carbonate cement, red color)	FeOs seem to occupy pore throats or even coat CO_3 cement; second generation of CO_3 grain coats/cement after initial CO_3 and FeO (FeO also impacted by circumgranular cracking); pore filling CO_3-->FeO-->CO_3 grain coats	Point contacts and long contacts; CO_3 cement seems to maintain space between grains	FeO after CO_3
Kbw-Ce-4 (FeO cement, FeO-replaced wood)	Fractured grains filled with FeO cement; radial fracture (filled with high birefringence mineral) cross-cuts FeO cement and grains; Fe replaces wood cell structure; some grain contacts do not contain Fe cements indicating compaction was prior to cementation	Point contacts ; long contacts most common	n/a
Kbw-W-3 (silica-replaced plant fragment)	1st generation grain coats prior to quartz overgrowths; 2nd generation grain coats after formation of quartz overgrowths; other cements after quartz overgrowths	Point and long contacts most common, seem to predate quartz overgrowths; some contacts might be concavo-convex, but may just be long contacts with quartz overgrowths surrounding the grain	n/a
Kbr-C-6 (ironstone horizon)	Possible replacement of grains by FeO along with wide grain spaces/floating grains --> possibly early cementation; CO_3 cement in caliche layer does not contain sand grains --> precipitation along fracture plane	Point and long contacts; wide pore spaces filled by FeO, "floating grains"	n/a

Table A4. Summary of powdered sample context and analyses performed for each sample.

Sample Number	Powdered Sample Name	Thin Section	SEM	ICP-MS	XRD	XRF	Context
PS-1	BFT1-1	x		x	x	x	Fault distal Aztec Sandstone, upper red zone
PS-2	BFT1-3	x	x	x		x	Fault proximal Kbw, stark white with gray-purple coloration
PS-3	BFT1-4	x		x		x	Fault distal Kbw, diffuse multicolored (white, red)
PS-4	BFT2-1	x		x	x	x	Fault distal Ja, middle alteration zone
PS-5	BFT2-2	x		x		x	Fault proximal Ja, white/orange, middle alteration zone
PS-6	BFT2-3	x		x	x	x	Fault proximal Kbw, stark white
PS-7	BFT2-4	x		x		x	Fault distal Kbw, diffuse multicolored (white, purple, yellow, red)
PS-8	BF20150703-2		x	x	x	x	Stark white Kbw adjacent to Baseline fault
PS-9	MSS-20180122-2	x	x	x	x	x	Kbw lithology, purple to white-tan coloration, 96.1 m stratigraphic height
PS-10	MSS-20180123-7	x	x	x	x	x	Kbw lithology, white with red-orange coloration, 221.7 m stratigraphic height
PS-11	MSS-20180125-12	x	x	x	x	x	Kbw-Kbr boundary, red-purple banded, 558.4 m stratigraphic height
PS-12	MSS-20180126-15	x				x	Middle Kbr lithology, red coloration, 769.9 m stratigraphic height
PS-13	MSS-20180126-18	x	x	x		x	Upper Kbr Lithology, red to yellow coloration, ~990 m stratigraphic height
PS-14	MSS-20180126-19	x			x	x	Uppermost Kbr lithology, red to white coloration, 1102.2 m stratigraphic height
PS-15	KO1Co3-20150802	x		x	x	x	Key outcrop 1 yellow coloration
PS-16	KO5KbwCo1-20150805			x	x	x	Key outcrop 5 white coloration
PS-17	KO1-Co5	x	x	x		x	Key outcrop 1 purple coloration
PS-18	Kbr-L-3	x	x	x		x	Upper Kbr carbonate pipe-like concretion
PS-19	Kbr-C-1A	x	x	x	x	x	Large spherical concretion center
PS-20	Kbr-C-1B	x	x	x		x	Large spherical concretion edge
PS-21	TMA20150725-01			x		x	Spherical, zoned concretion near Tearfault Mesa
PS-22	KO5-Ce1	x				x	Pod/pipe-like concretion with digitate structures on inner surface
PS-23	KO5-Ce2	x		x		x	Blocky, cemented horizons with digitate structures on upper surface

ICP-MS: Small (about 0.25 g) aliquots of each sample were placed in a lithium capsule and digested in hydrofluoric acid, then introduced to the mass spectrometer. Samples were analyzed along with a standard material Standard Reference Material 1643f (SRM-1643f) for calibration and determination of error.

XRD: Analysis was performed at the XRD Laboratory at the Energy and Geoscience Institute at the University of Utah using a Bruker D8 Advance X-ray diffractometer. The clay-sized fraction was extracted from a small aliquot of the powdered sample by immersion in deionized water and pipetted from the upper part of the test tube following setline. The fine particles were removed from this water sample by centrifuging for 30 minutes at 3000 RPM. The water was decanted and the sample was thoroughly mixed using an ultra-sonic homogenizer. The slurry was applied to a glass slide and allowed

to settle to obtain an oriented sample and once dried, an 'air-dried' XRD pattern was obtained. The sample was then exposed to ethylene glycol vapors for about 48 hours at 65°C, then a 'glycolated' XRD pattern was obtained. Nine samples were then also heated at 375°C for 1 hour and an additional XRD pattern obtained.

XRF: A handheld Bruker XRF spectrometer was used to measure relative elemental abundances in select samples, using the following settings: 15 kV high voltage, 25 μA current, 2 minutes per sample, under an ambient air atmosphere. The raw counts were deconvolved using a Bayes method and plotted as relative elemental abundances, since a full calibration curve was not incorporated.

(U-Th)/He Dating

Five small samples (about 1- to 3-cm-long pieces) of select concretion forms were submitted to the Arizona Radiogenic Helium Dating Laboratory (ARHDL) at the University of Arizona for (U-Th)/He dating of iron oxide cements. The samples were selected based on their unique morphologies (large sphere, massive with digitate structures on top surface, pod/pipe with digitate structures on interior surface) or for their relationship to stratigraphic surfaces (bedding-parallel cemented horizon) or structures (Baseline fault-coating oxides). Three aliquots of each sample were measured using an Element2 ICP-MS and compared to a zircon standard.

RESULTS

This section of the supplemental Appendix focuses on results of the diagenetic facies characterization, including their attributes, distribution determined through fieldwork and remote sensing-based diagenetic mineral mapping, and the specific interpretations of data that support the paragenetic timeline interpretation and insight into fluid-flow pathways and controls. This section is organized into four subsections.

1. Detailed results are presented for the coloration and cementation facies from both field and analytical results, followed by their interpretation.

2. Geochemical and mineralogical attributes of the diagenetic facies and other samples, are described and then interpreted.

3. Additional notes address stratigraphic distribution of the diagenetic facies.

4. Remote sensing mapping, workflows, and results include additional derived mineral maps that support the laboratory analyses.

Diagenetic Facies Characterization

Coloration Facies

Field characterization: Coloration facies were documented/described and include a wide range of hues and expressions. Sandstone hues are predominately of stark white, white/tan/gray, yellow, yellow-brown/brown, red, and purple, and coloration expression is solid, pastel/diffuse, or variegated/concentrated. The specific characteristics of the coloration facies and mineral characteristics are summarized in Table 1.

Many of these colors co-occur, however, there seems to be a preferred co-occurrence between yellows, browns, and purples (mostly goethite related with the purple hematite spherules), and a preferred co-occurrence between purples and reds (mostly hematite related). All of these hues overprint primary sedimentary structures yet mostly follow bed-scale stratigraphic architecture. Intensity and scale of continuity of coloration patterns varies throughout the field area, but coloration is typically more diffuse and pastel in the white sandstone member, more intense and concentrated/variegated through the lower red sandstone member, and much less varied and more-or-less monotonous brick red throughout the upper red sandstone member. Further discussion of stratigraphic coloration patterns, with respect to the stratigraphy, in particular on either side of the Baseline fault trace, is included below.

Coloration of stratigraphic uniit: As its name implies, the white sandstone member consists mostly of white/tan/gray sandstone (e.g., Figure A3) but with a wide range of other hues present that overprint the white coloration and that occur in distinct stratigraphic

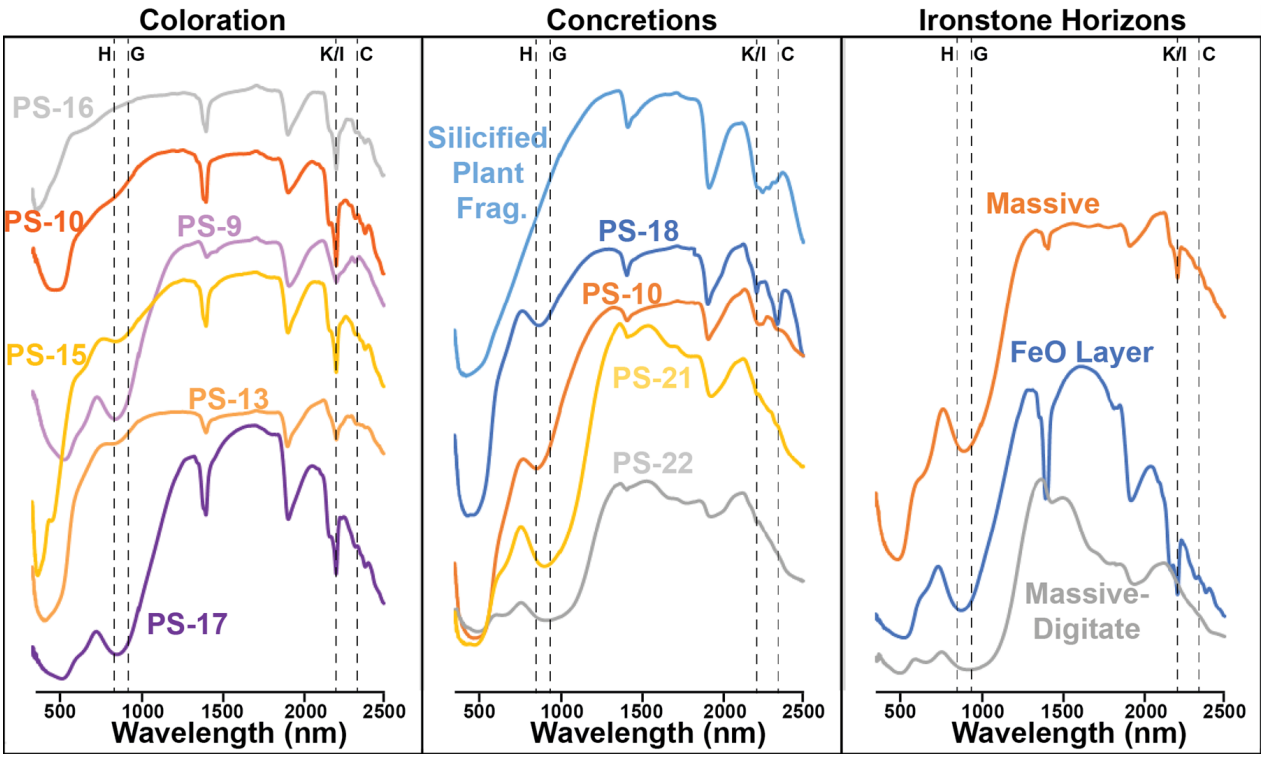

Figure A3. Summary reflectance spectral profiles of diagenetic facies. Dashed lines indicate characteristic absorption features of key mineral species: H = hematite, G = goethite, K = kaolinite, I = illite (K/I simply denotes the similar absorption feature for the two minerals and not any grouping/interlayering), C = calcite. Other abbreviations: PS = powdered sample, Frag. = fragment, FeO = iron oxide.

zones. Coloration throughout this member is typically diffuse and pastel in its expression, and comprises red to red-purple, purple, yellow, yellow-brown, and brown hues (Figures 3A through 3E). Colors typically increase in intensity towards bed tops (Figure 3B), and in proximity to cementation facies, especially ironstone horizons (Figure 3C). Most hues co-occur in parts of the member, but red hues typically do not directly contact yellow, yellow-brown, or brown coloration. A common co-occurrence exists between purple and yellow-brown (mustard yellow) facies in this member as well as the lower red sandstone member (Figure 3D). Where all hues are present there is usually a purple color intermediate between the red and yellow/brown hues (Figure 3E).

The lower red sandstone member is dominated by red hues, but exhibits similar variability in the range of hues contained as the white sandstone member (Figure 4). Coloration in this part of the formation is typically more concentrated and variegated, especially along bed boundaries and sedimentary structure boundaries (Figures 4A and 4B). Intense variegated coloration often follows lamina of sedimentary structures (Figure 4A) and even those distorted by soft-sediment deformation and convolute bedding (Figure 4C). Yellow/yellow-brown and purple hues again show a preferred association, and red hues do not typically come into contact with yellow/yellow brown hues and only through an intermediary purple or white/light red hue (Figure 4D).

The upper red sandstone member, beginning at about 750 m above base, is primarily an even "solid" red with very little variability in coloration (Figure 5A). Where coloration does vary, including white, yellow, and purple hues (Figures 5B and 5C), it is typically localized and is not as laterally or stratigraphically extensive as the white or lower red sandstone. Again, a preferred association between purple and yellow hues seems to exist in this member (Figure 5C). Conglomeratic lenses typically exhibit a red-brown coloration, darker than the surrounding sandstone, and the cement of the matrix material reacts with dilute HCl (Figure

5D). This color difference between the conglomeratic channel forms isolated within sandy overbank deposits is apparent when viewing this part of the member as red-brown conglomerate lenses isolated within the red color of the sandstone (Figure 5E).

Analytical results: SEM images of coloration facies samples show the morphology of goethite in yellow/yellow-brown-colored sandstone as acicular to platy crystals less than 1 μm across (Figure 8A) and hematite in red-colored sandstone as platy crystals less than 1 μm across (Figure 8B) and rare rhombohedral crystals up to about 10 μm across (Figure 8C). Kaolinite clays are also visible in red-colored sandstone of the upper red sandstone member (Figure 8D). The hematite spherules observed in the purple coloration facies are clearly identified in SEM (Figure 8E) and their smooth surface texture is clearly visible. Chlorite(?) rims that are arranged in rhombohedral to hexagonal arrangement, possibly formed around a later dissolved crystal (Figure 8F).

Reflectance spectroscopy of hand samples and in situ diagenetic facies throughout the field area provides insight into the general mineralogy that leads to coloration and concretionary types (Figures 15E, 15F, and A3). Generally, most samples exhibit narrow and strong absorption features centered at about 1414 nm, 1909 nm, and an absorption "doublet" with a minor absorption feature at 2165 to 2170 nm and a deeper absorption at 2207 nm. In some samples, the 2207 nm feature is not accompanied by the 2165 nm absorption (e.g., PS-9 of Figure A4). Red-, orange-, to purple-colored sandstone of both the Baseline and Aztec Sandstones exhibit a strong and relatively narrow absorption feature at about 850 to 855 nm, with purple colors exhibiting a stronger absorption than red/orange colors. In yellow to yellow-brown samples the same absorption feature is broadened and stretched to longer wavelengths (about 940 nm). Red-colored sandstone of the lower red sandstone member in diagenetic pattern focus area A and of the upper red sandstone in diagenetic pattern focus area B (Figure 1C) exhibit similar absorption features of other red-colored sandstone but with the addition of an absorption feature at 2340 nm. White-colored sandstone lack absorption features observed in the aforementioned spectral ranges of the colored sandstone.

Thin section attributes of samples from coloration facies share several common characteristics, but also display mineralogical attributes that contribute to the various coloration hues and intensities (while generalized observations of attributes were made in the 104 thin sections prepared for this study, a summary of detailed observations made in 9 key thin sections are provided in Tables A3A through A3C). Generally, coloration correlates with the presence/abundance and mineralogy of grain-coating iron oxide minerals. White-colored sandstone lacks substantial grain coating minerals (Figure 18A), whereas purple sandstone contains about 5-μm-diameter opaque mineral spherules (Figure 18B), and yellow/yellow-brown and red-colored sandstone contain dark-colored to opaque minerals of a size too small to resolve in thin section (Figures 18C and 18D). Yellow-colored samples with greater intensity contain nearly isopachous grain coats up to about 3 μm thick,, which increase in concentration in smaller pore spaces to occlude the pore space (Figure 18C). Purple sandstone contains 5-μm-diameter opaque mineral spherules, but when cut by the plane of the thin section exhibit a brick red coloration and exhibit white to gray-white color with red internal reflections in reflected light microscopy. The spherules exhibit a smooth external and internal texture and spherical morphology, and lack surface roughness or blocky internal texture characteristic of pyrite framboids. These characteristics are consistent with the mineral hematite. Red-colored sandstone also contains opaque grain-coating minerals that exhibit a patchy distribution and increase in concentration within smaller pore spaces to occlude the pore space (Figures 18D and 18E).

Coloration facies all commonly contain very little pore-filling cements, and indeed many maintain an open pore network. Cementation is typically composed of minerals with low birefringence and occurs as meniscus cements (likely quartz or feldspar) at point and long contacts between grains. In purple, yellow/yellow-brown, and red coloration facies, it is common for iron oxide grain coats to occur in high enough concentration within smaller pore spaces so as to occlude the pore space. Iron-bearing authigenic cements are primarily iron oxides throughout the Baseline Sandstone, and secondarily as iron sulfides in rare occurrences re-

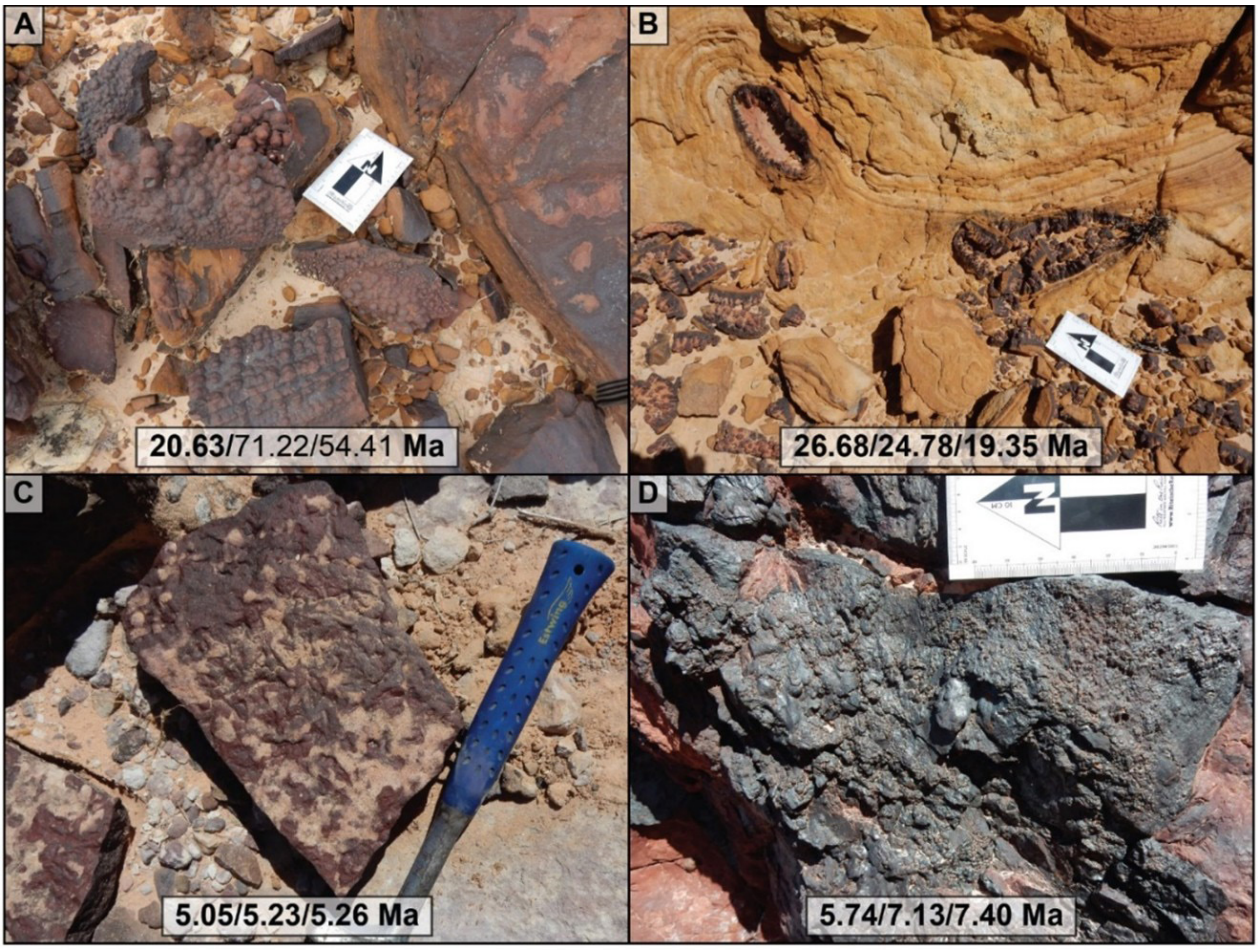

Figure A4. (U-Th)/He age summary with images of samples, and bold numbers indicate reliable age measurements. (A) Ironstone horizon with a digitate surface, the two unusable ages are due to a high Th/U ratio and low U. (B) Pod-like structures with digitate interiors from key outcrop 5. (C) Burrowed ironstone horizon from diagenetic pattern focus area A. (D) Metal oxides precipitated along the plane of the Baseline fault in diagenetic pattern focus area C.

stricted to the lower to middle white sandstone member. The opaque grain-coating minerals, typically iron oxides (goethite or hematite), do not commonly occur between the grains and meniscus cements but commonly occur within grain fracture spaces. The hematite spherules of the purple-colored sandstone commonly occur along grain contacts and within some fractured grains, however, other grain contacts including those that contain cement do not contain the spherules. Dissolved lithics and/or feldspar contain iron oxide grain coats along their outer surface and within the dissolved grain. In contrast, the purple sandstone contains dissolved grains with hematite spherules along its outer surface but not within the dissolved grain.

Coloration interpretation: Overall, the coloration of sandstone throughout the Baseline Sandstone indicates that the bleached and light colors lack or are low in iron oxide grain-coating minerals. Yellow/yellow-brown to brown hues and the red to purple hues indicate higher concentrations of iron oxides, as verified by the field, spectral, and analytical methods. The hues represent coloration changes by broad diagenetic fluid flow through the formation with low to moderate degrees of cementation, controlled by basic depositional textures to burial porosity and permeability, particularly where the hues cut across depositional texture. The hue intensity increase towards tops of beds likely indicates bed-scale heterogeneity and permeability differences at bed

boundaries, leading to increased precipitation at the tops of beds. In reflectance spectra, the about 850 nm absorption feature in red-, orange-, and purple-colored sandstone, along with most iron oxide concretions, and the red-colored horizons indicates that they contain hematite as the predominant iron oxide phase. The broadened absorption feature centered at about 940 nm exhibited by yellow- to yellow-brown coloration facies and associated concretion forms and horizons indicates the presence of goethite. The white-colored sandstone lacks the absorption features characteristic of iron oxides, indicating that they lack iron oxide minerals. Thin section characterization suggests that coloration facies hue is determined by iron oxide crystal size/shape and mineralogy, whereas intensity is determined by overall concentration of iron oxide in the sample. Purple and red coloration facies contain hematite, with the purple coloration derived from the occurrence of the 5 μm spherules (Figure18B) and red-coloration derived from various concentrations of the sub-micron size platy(?) hematite grain coats (Figures 18D and 18E). Yellow and yellow-brown coloration facies both appear to contain goethite, and their relative concentration determines the hue and intensity (Figure 18C).

Cementation Facies

Field characterization: Cementation facies occur in a very wide array of geometries, morphologies, and mineralogies, and can be subdivided into ironstone horizon types and concretionary types (Figures 6, 7, and 9). Ironstone horizon types are those cementation facies that exhibit largely bed-parallel or bounding surface-parallel geometry of relatively long lateral extent. This cementation type is further subdivided into "thick" form (greater than about 5 cm) and "thin" form (less than about 5 cm), based on the overall thickness observed of the various horizon types.

For the ironstone horizon types, the thick form occurs in three principal sub-forms (Figure 6). First, the massive sub-form is an up to an about 10-cm-thick massive/structureless cementation layer that occurs at the tops of beds. This sub-form is the most laterally extensive of the thick ironstone horizons, with maximum lateral extent directly observed up to about 75 m, with some horizons possibly extending up to about 250 m (as observed in aerial imagery). Coloration again darkens approaching the top of the horizon and is commonly dark brown with some beds dark red in color. This style is most common in the footwall part of the Baseline Sandstone. Second, the massive-digitate sub-form, is composed of an up to an about 10-cm-thick cementation layer that is capped by about 1- to 5-cm-tall digitate forms that are oriented perpendicular to the bed and in an upward direction (i.e., on top surfaces of cemented horizons). Where in situ, this horizon style occurs at bounding surfaces of cross-bedded/scoured sandstone. This cement is typically dark brown in color and is associated with yellow/yellow-brown, and brown-colored sandstone. Third, the massive-concentric sub-form consists of internal concentrically layered textures within the well-cemented part. This sub-form has the same overall attributes of the massive (first) sub-form, with greatly reduced lateral extent of about 25 m directly observed in the field.

The thin form ironstone horizon type is composed of two principal sub-forms. First, the iron oxide layer is a thin (up to about 3 cm) layer of brick red to purple iron oxide that surprisingly contains very few sand grains. This layer typically occurs at the tops of beds that also exhibit a gradual increase in purple color intensity approaching the layer. Lateral continuity of this sub-form is moderate, with observed lateral extent in the field up to about 20 m. Second, the burrowed subform is composed of a thin (up to about 3 to 5 cm) layer of ironstone that contains horizontal burrows. The burrows appear to be single shaft, straight to low sinuosity with simple fill and lacking any obvious lining. However, due to the degree of cementation, fill and lining details are unclear. These burrowed horizons also commonly exhibit a coloration intensity change approaching the top of the cemented horizon, but most commonly the coloration associated with the horizon is thin (e.g., burrowed horizon on Figure 6). The cements that make up this sub-form are typically brick red to purple. The subform is found throughout the white sandstone member, but examples with the highest lateral continuity occur near Tearfault Mesa.

Concretionary types: The Baseline Sandstone concre-

tionary cementation facies are composed of localized concentrations of authigenic cements that result in differential erosion, and exhibit laterally/vertically restricted extent. Here the concretions are defined to be localized, discrete individual cemented forms, as opposed to the previously described horizons that are typically laterally extensive at larger scales. Concretions are highly varied in composition, sizes, and morphologies. Concretions fall into three main compositional categories, ordered in relative abundance from most abundant to least abundant: iron oxide, carbonate, and silica.

Iron oxide concretions occur in many different morphologies and sizes throughout the area and are broadly categorized into spheroidal/spherical, iron-replaced wood, rod-like, pipe/pod, and irregular forms. The spheroidal forms occur in size from less than a mm, to over 2 m in longest dimension, whereas spherical forms, those with nearly equal x, y, and z axes, occur up to 1 m in diameter. The size distribution of the spheroidal and spherical concretions is skewed towards smaller sizes; typically, maximum size is up to about 20 cm in diameter, with only up to about 30 known examples of concretions that exceed this size within the study area. These spheroidal and spherical concretions commonly exhibit red, red-brown, and dark brown hues on their exterior surfaces. Internally, broken small (less than 10 cm) spheroidal and spherical concretions commonly exhibit an internal rinded structure with purple and red-colored iron oxide in what commonly appears to be iron-replaced wood at the core, a medium gray core, stark white poorly cemented core, or a brick red core (Figures 9A and 9C). Typically, if the core is medium gray sandstone, the concretion also contains a bright orange ring between the red/purple in the outer layers, and the gray of the core. Surface textures are most commonly smooth, but some spheroidal forms include smaller spheroids superimposed on the surface producing a bumpy, "knobby" texture (Figure 9A, number 6). Iron-replaced wood concretionary forms preserve a wood-grain texture (Figure 9B), and include up to about 5 cm overgrowths that extend into the surrounding sandstone, overlapping with the irregular concretionary morphology. The large spheroidal/spherical concretions (greater than 20 cm) typically do not exhibit significant variation throughout the interior.

The rod-like concretionary forms commonly occur as straight, smooth cylindrical forms with some also exhibiting bulbous/irregular growths along the length of the rod (Figure 7E). These forms range up to 2 to 3 cm in diameter and up to about 15 cm in length. These concretion forms commonly exhibit dark brown exterior surfaces, purple to purple-brown interiors. Pipe/pod concretionary forms are those that exhibit densely cemented rinds that define an irregularly shaped domain, and enclose a very poor cement interior (Figure 7F). The pods commonly exhibit digitate structures up to about 2 to 3 cm in length oriented towards the pod center (similar to geode growth). These concretion forms are associated with the digitate surface ironstone horizon, and are surrounded by Liesegang banding of yellow-brown to brown coloration. The interiors, along with being less well-cemented, also exhibit a coloration difference with the surrounding sandstone as a light red color. Irregularly shaped concretion forms of various sizes comprise the last category of iron oxide concretion cementation facies, ranging from cm-scale up to irregular/pillow-shaped forms several meters in length (Figures 7G and 7H). Small-scale forms are commonly associated with iron-replaced wood fragments, and some irregularly shaped concretions contain iron-replaced wood, with additional over-cementation growth into the surrounding sandstone. Large-scale irregular forms commonly exhibit a range of internal textures, from solid masses with roughly concentric layering (Figure 7H), to 2- to 3-cm-thick rinds and poorly cemented interiors.

Carbonate concretion forms occur in a variety of sizes and morphologies, and are typically only in the red sandstone member or the Aztec Sandstone adjacent to the Baseline fault. Morphology of these carbonate concretion forms includes irregular/pillow-like/elongate forms up to 10 to 20 m in length and 2 to 3 m across (Figure 10A), pipe-like (Figure 10B), clusters of spherical/spheroidal masses up to about 5 cm in diameter (Figures 10C and 10D), spheroidal to oblate individual concretions up to about 30 cm in diameter (Figure 10E), and oblate septarian nodules up to about 15 to 20 cm in diameter (Figure 10F). The large elongate forms commonly contain clusters of spheroidal masses at their centers. Coloration of these forms is typically medium

to light red, with some pipe-like forms in the upper red sandstone exhibiting a yellow center and redder rim (Figure 10B).

Silica concretionary forms occur principally in float as silica-replaced plant fragments (Figure 10G), or in situ as silica cements surrounding replaced plant fragments (Figure 10H), and occur in the middle white sandstone member to lower-middle red sandstone member interval. Plant fragments exhibit textures similar to the tree fern *Tempskya* (Tidwell and Hebbert, 1992; other wood fragments with conifer[?] textures are replaced with iron oxide, as described above). In situ examples are localized cement in irregularly shaped nodules up to about 10 to 20 cm thick, and 1 to 2 m lateral extent. Cementation appears to have initiated at the wood fragment and grew into the surrounding sandstone. The only known example of in situ silica concretions occurs in the uppermost white sandstone member very near the boundary with the red sandstone.

Analytical results: Concretionary forms and ironstone horizons exhibit similar VNIR spectra absorption features to the coloration facies. The iron oxide concretions most commonly exhibit the same absorption features of the purple-colored sandstone (e.g., PS-18 and PS-10 of Figure A3). Concretions that occur in association with yellow- to yellow-brown coloration, or that exhibit a deep purple-gray coloration (as opposed to a reddish-purple) exhibit absorption features similar to the yellow- to yellow-brown colored sandstone (e.g., PS-22 of Figure A3). Some concretions, especially zoned concretions, exhibit an absorption feature intermediate of the red vs. yellow-colored sandstone where the absorption feature minimum is shifted to about 900 nm (e.g., PS-21 of Figure A3) consistent with a mixture of hematite and goethite (with possible other iron oxyhydroxides). Ironstone horizons exhibit similar absorption features to the coloration facies and concretionary forms. The brick-red iron oxide layer sub-form exhibits the strong and narrow absorption feature at about 850 to 855 nm (consistent with hematite), the massive with digitate structures sub-form exhibits a strong broadened feature centered at about 940 nm (consistent with goethite), and the massive sub-form exhibits a strong absorption intermediate to massive and massive with digitate structures having the minimum at about 900 nm. Carbonate concretions exhibit similar absorption features to the red-colored sandstone with the addition of an absorption couple at 2340 nm and about 2500 nm (consistent with carbonate minerals). Silicified wood fragments and silica overgrowths exhibit an absorption pattern similar to the white-colored sandstone but with a difference in the 2207 nm absorption broadened to longer wavelengths (broadly consistent with quartz with kaolinite).

Iron oxide cementation facies exhibit key petrographic characteristics (Tables A3A through A3C). Pore-filling cements in these samples are typically completely opaque in thin sections that are normally about 30 μm thick. In reflected light microscopy the iron oxide cements exhibit a medium-gray to gray-white with brown internal reflections (goethite) or gray-white to white with red internal reflections (hematite, Figure 18G). In spherical concretions that exhibit zonation in color (e.g., Figure 9C) or contain wood fragments at their core (Figure 18I), reflected light microscopy reveals pyrite in the gray-colored core, hematite in the purple-red-colored outer zone, and jarosite at the boundary between pyrite and hematite. The pore-filling hematite of Figure 18I also contains some goethite in the pore throats. The pore-filling iron oxides of the cementation facies commonly maintain wide spacing between the framework grains (Figures 18G and 18I).

Silica-replaced plant fragments (Figure 18H) contain multiple generations of iron oxide grain-coating minerals (Kbw-W-3 of Tables A3A through A3C): (1) along surfaces of framework quartz grains beneath quartz overgrowths, (2) within radiating quartz crystals surrounding possible stems characteristic of the tree fern *Tempskya*(?) false trunk structure (Tidwell and Hebbert, 1992), and (3) along the external boundary of both the quartz overgrowths surrounding detrital grains and the crystal faces of the radiating crystals. It is unclear if the 1st and 2nd generation grain coats formed contemporaneously or subsequently, but the 3rd generation is clearly the youngest. Since the pore-filling cements obscure and corrode grain edges, grain coating minerals are unresolved in many samples cemented by carbonate (Figure 18F), iron oxide (Figure 18G), or pyrite (Figure 18I) cements. Host-rock lithology of the upper red sandstone member (Figure 18F) contains

abundant carbonate cement that exhibits a poikilotopic fabric with individual crystal domains encompassing up to two to three sand grains. The carbonate cement also exhibits circumgranular cracking that commonly forms in soil environments and/or caliche layers as a result of thermal effects (Ulmer-Scholle et al., 2016). A second generation of carbonate crystals occur in the circumgranular crack space and appear to nucleate on the framework grains. Silica-replaced plant fragments commonly exhibit a radiating pattern of quartz crystals with the *Tempskya*(?) stems at the center, and quartz overgrowths around the quartz grains adjacent to the wood (Figure 18H). Quartz overgrowths become progressively less well formed (smaller crystal faces) with distance away from the wood area. These quartz overgrowths are the only known true overgrowths (in optical continuity with the quartz grains), with limited/minor amounts of meniscus quartz cement throughout the rest of the formation.

The SEM images reveal key pore-scale morphological attributes of diagenetic minerals. The metallic mineral oxides that occur along the Baseline fault (Figure 15) are revealed to consist of hematite rosettes about 10 µm across and made up of platy hematite crystals up to about 0.8 µm thick (Figure 8G). The iron oxide-cemented burrowed sandstone (Figure 8H) displays pore-filling platy hematite along with vermiform kaolinite in contact with the grain. The iron oxide layer sub-form of ironstone horizon cements is composed of amalgamated spherules (Figure 8I), the same spherules that occur in purple-colored sandstone. Carbonate cements from the upper red sandstone member also exhibit the circumgranular cracking with visible clay minerals in the SEM images, and secondary, small carbonate crystals in the open space (Figure 8J). Morphologies of iron oxide crystals that replaced the wood texture range from a granular/globular(?) to acicular morphology (Figure 8K). The silica-replaced plant fragments and quartz overgrowths exhibit euhedral crystal faces and are coated with a platy submicron-sized mineral (Figure 8L).

Cementation interpretation: The intermediate absorption feature centered at about 900 nm exhibited by some concretion forms and horizons (e.g., PS-21 of Figure A3) likely indicates a mix of hematite and goethite, with other possible iron oxyhydroxide phases (e.g., lepidocrocite, ferrihydrite). The white-colored sandstone and the silicified wood and silica overgrowths lack the absorption features characteristic of iron oxides, indicating that they lack iron oxide minerals. Thin section characterization reveals that the cementation facies also exhibit a general relationship between color and mineralogy. Brown- to gray-purple-colored parts of cementation facies are composed of goethite cements, whereas red- to reddish-purple-colored parts are composed of hematite cements. Bright reflection with a gold tinge indicates that dark gray cements at the cores of spheroidal concretionary forms in the lower to middle white sandstone member are composed of pyrite (Figures 9C and 18I).

Diagenetic Facies Geochemical and Mineralogical Attributes

Compositional attributes of the diagenetic facies are largely deduced from bulk geochemical and pore-scale mineralogical analyses of field samples and representative diagenetic facies. These analyses include VNIR, ICP-MS, XRF, and clay-fraction XRD.

General VNIR Reflectance Spectroscopy and Interpretations

Specific spectroscopic observations related to the iron oxide, carbonate, and/or clay minerals present in each diagenetic facies is outlined above (Figure A3), but other more general observations provide additional insight into depositional and diagenetic processes as discussed here. Key absorption features common throughout most of the measured spectra include absorptions at 1410 nm and 1909 nm and a paired feature at 2207 nm and 2165 to 2170 nm (deeper and wider absorption in the longer wavelength). Samples that occur in intervals with known occurrence of carbonate minerals (in carbonate framework grains, authigenic cements, or later carbonate fracture/joint fill and caliche) exhibit an absorption at about 2340 nm and likely the beginning of another at 2500 nm. It is unclear if the 2500 nm feature is a true absorption since the spectral limit of the ASD spectrometer is 2500 nm.

When compared to representative spectra of likely

mineral occurrences (dashed lines of Figure A3; after Kokaly et al., 2017) the measured spectra indicate the presence or absence of characteristic diagenetic minerals. Iron oxide mineralogies largely give the diagenetic facies color along with the specific concretion mineralogy, the type of clay minerals present, and the presence/absence of calcite phases in the lithology and carbonate concretion forms. This mineralogical difference possibly relates to the diagenetic evolution of the formation.

The absorption features at 1410 nm and 1909 nm common to most samples likely indicates the presence of hydrated minerals (clays, oxyhydroxides) throughout the formation. Likewise, the absorption feature at 2207 nm indicates the presence of illite (Simpson and Rae, 2018), or when paired with the minor absorption feature at 2165 to 2170 nm is indicative of kaolinite (Bishop et al., 2008), which is present in most samples. The variable depth in the 2165 to 2170 nm feature indicates a variable proportion of kaolinite possibly mixed with other clay minerals such as illite or montmorillonite, with a deeper absorption indicating a higher kaolinite proportion and a lower absorption indicating a higher proportion of montmorillonite (e.g., McKeown et al., 2011). The absorption feature at about 2340 nm is consistent with an absorption feature found in carbonate rocks, and in the mineral calcite (Gaffey, 1986).

(U-Th)/He Dating of Iron Oxide Minerals

Five analyzed samples of cementation facies (two ironstone horizons, two concretionary, and one from the plane of the Baseline fault), were chosen for a preliminary pilot (U-Th)/He dating (Figure A4). Of the five samples analyzed, three returned consistent ages across all three aliquots per sample, one returned only a single usable age due to a high Th/U ratio and low U, and the fifth (from a large spherical concretion) did not return any usable dates due to a high Th/U ratio and low U (see Figure A4). The single date usable from the digitate surface ironstone horizon type sample is 20.63 ± 0.89 Ma, consistent with the age of the pipe/pod-like concretion sample from the same key outcrop (KO-5; see Figure 1C) at 26.68 to 19.35 ± 0.52 Ma. The sample of the burrowed sub-form ironstone horizon type sample showed an age of 5.26 to 5.05 ± 0.22 Ma, and the sample of the Baseline fault plane-coating oxides sample returned an age of 7.40 to 5.75 ± 0.13 Ma (Figure A4).

ICP-MS Observations and Interpretations

Bulk elemental concentration for powdered samples shows some general patterns in variation within the broad subdivision of the samples as Baseline fault transect (BFT), coloration facies, or cementation facies (Figure 11 and Table 5). BFT samples exhibit wide variability in alkali earth metals, U and Th, and select first row transition metals. Only a few elements out of those analyzed display any discernible pattern, with main differences arising from relationship to the formation to which the sample belongs (Aztec Sandstone [Ja] vs. the Baseline Sandstone [Kb]; see Table 5) or proximity to the fault trace. Ja samples contain higher concentrations of Mg, and generally contain elevated amounts of Ba, Sr, Mn, Fe, relative to the rest of the BFT suite except for PS-6. Fault-proximal Kb samples that exhibit a white/stark white coloration generally contain higher amounts of U, Th, and Ti. PS-6 is greatly enriched relative to other BFT samples in many elements making identification of patterns difficult.

Coloration facies generally exhibit relative enrichment/depletion determined by coloration hue and intensity; however, a possible stratigraphic pattern in these elemental abundances may also exist (Table 5). The representative yellow (PS-15) and white (PS-16) samples generally contain the least absolute amount of the elements analyzed with the yellow sample commonly containing the least, and the white sample containing the least of Ca, V, and Fe. Red and purple coloration are typically enriched more than white/yellow coloration samples in the elemental groups listed above, with more intensely colored samples enriched further. Interestingly, the intense purple coloration sample (PS-17) is enriched over the cementation facies samples in Sr, Ba, Th, Ti, V (except PS-21), and Cr, and it contains equal amounts of Fe as the center of the large spherical concretion (PS-19).

Cementation facies samples are generally enriched in most elements analyzed in comparison to the BFT suite and the coloration facies samples (Table 5); however, for Sr and Ba the difference is not as large and may

even, generally, be reversed. The carbonate concretion sample (PS-18) is enriched relative to the other cementation samples in Ca and Sr, but generally contains the lowest concentrations of the other elements from among the cementation samples. Samples PS-19 and PS-20 come from the same large spherical concretion (from near the center and edge, respectively) but they typically exhibit a distinct difference in concentration for most elements measured, in conjunction with observed zonation of coloration and changes in dominant iron oxide phase (hematite vs. goethite). The concretion center sample typically is relatively enriched in alkali earth metals but depleted in U and Th, and the select first row transition metals except for Mn. The zoned concretion (PS-21) exhibits similar magnitude of enrichment relative to the other cementation facies samples, but exhibits marked relative depletion of Mg and Ti, and marked enrichment in V. The ironstone horizon sample (PS-23) exhibits marked relative enrichment in Be, U, and Ti, and also exhibits a marked relative depletion in Cr and V.

Plotting elemental concentrations against one another for various redox-sensitive elements show varying concentration of U-Th, V-Cr, and Fe-Mn in populations of coloration facies, cementation facies, and samples collected along the Baseline fault. When U and Th (Figure 11A), V and Cr (Figure 11B), and Fe and Mn (Figure 11C) are cross-plotted, the three main groupings of powdered samples (BFT, coloration facies, and cementation facies) occur in fairly distinct groups. In general, the BFT and coloration facies overlap in the plot space, but the BFT and cementation facies do not overlap. The slopes of long-axes of ellipses drawn around the points vary in the plots: all three groups differ in U/Th, all three groups are similar (with possibly a slightly different slope in the cementation facies) in V/Cr, and have similarities between the BFT samples and coloration facies but different from cementation facies in Fe/Mn. When plotting the ratios of U/Th, V/Cr, and Fe/Mn against Fe concentration (to account for iron concentration between coloration and cementation facies), each group exhibits distinct slopes of enclosing ellipse long axes except the BFT and coloration facies groups in the Fe/Mn plot.

The bulk geochemical attributes of diagenetic facies samples provide key insights into relative enrichment/depletion of elements of authigenic minerals and redox-sensitive elements. The concentration of alkali earth metals likely reflects the composition of authigenic clay minerals and cements in the samples. Those samples that are relatively enriched in Mg likely contain smectite clays; however, the distinct enrichment of PS-13 and of PS-18 likely is the result of proximity to the Horse Spring Formation, which contains abundant magnesite ($MgCO_3$). The enrichment of U and Th in the intensely colored and cementation samples likely reflects either incorporation of these elements into the crystal structure of the hematite mineral, which gives the red and purple colors, which is found in the iron oxide cements or possibly adsorption of uranium onto the surface of the iron oxide minerals. The first-row transition metals likely relate to redox conditions under which the authigenic iron oxide cements formed. The relative enrichment in Fe and depletion in Mn of the large spherical concretion (corresponding to a change from goethite at the center and hematite at the edge) indicates that redox conditions fluctuated, either through changes in diagenetic fluid pH or redox potential, during the growth of the concretion.

XRF Observations and Interpretations

Similar to the ICP-MS results, XRF analyses of powdered samples provide qualitative insight into their bulk chemical attributes (Figure A5). Relative elemental abundances of powdered samples of two Baseline fault transects show generally a relatively higher amount of Al and lower amount of K in the hanging wall (white sandstone member rocks) vs. the footwall (Aztec Sandstone) of the fault. The amount of iron present seems to correlate with color, having the purple- and red-colored rocks containing a higher amount vs. the white and stark white rocks containing less. All samples exhibit varying amounts of sulfur; however, the purple-colored sandstone and the zoned spherical concretion contain relatively larger amounts.

Coloration and cementation facies samples exhibit similar relative elemental abundances to the Baseline fault transect samples. Iron abundance correlates with coloration, with white sandstone containing lower rel-

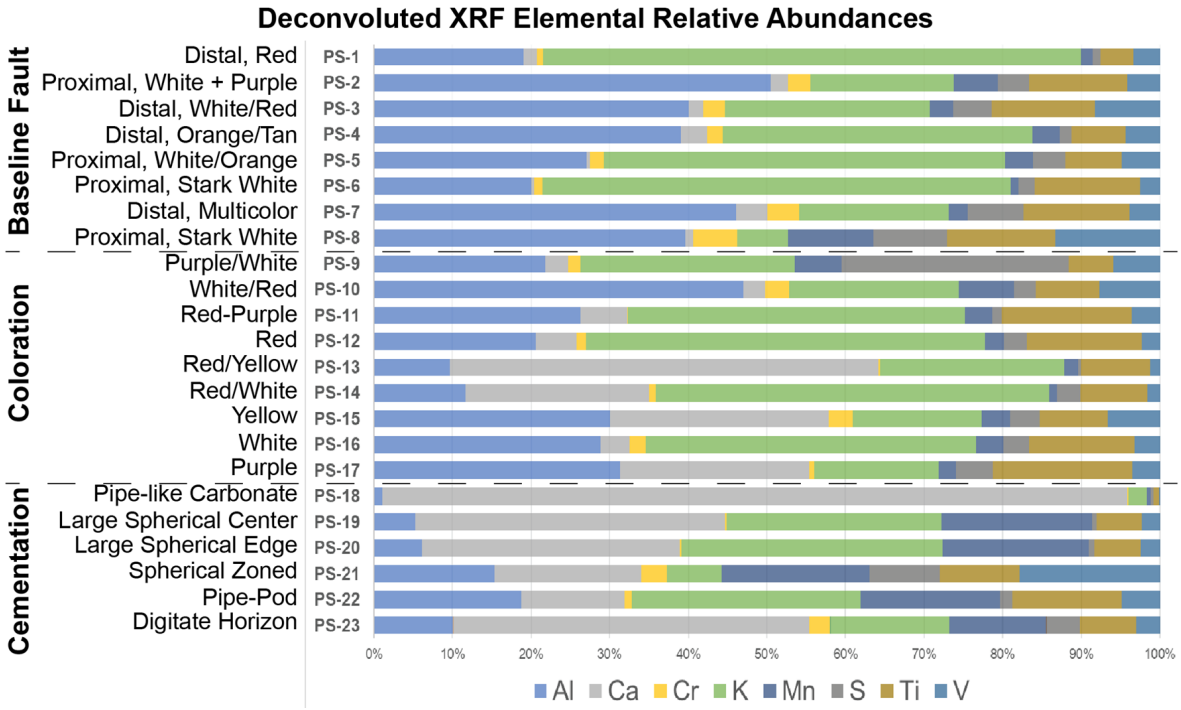

Figure A5. Deconvoluted XRF results showing the qualitative relative concentration of some redox-sensitive elements. Samples are grouped by the suite to which the samples belong.

ative amounts whereas red- and purple-colored sandstone containing more and, as would be expected, the iron oxide concretion samples are dominated by iron. White-colored sandstone again exhibits a relative increased abundance in Al and, in contrast to the Baseline fault samples, an inverse correlation between Al and K does not appear to exist in these samples. Samples from the upper red sandstone member in diagenetic pattern focus area B (PS-13, PS-14, and PS-18) exhibit a relative increase in Ca, coincident with known occurrences of carbonate cements. Surprisingly, a yellow-colored sandstone from the lower white sandstone member (PS-15) also exhibits a relative increase in Ca.

The relative elemental abundance of Baseline fault powdered samples likely indicates the degree of weathering/alteration experienced by the rock and possibly relates to the characteristics of the fluids involved. The higher proportion of aluminum and lower proportion of potassium in the hanging wall samples likely indicates a higher degree of chemical alteration in the hanging wall rocks, possibly as a result of alteration of potassium feldspars into kaolinite from fluids flowing along the fault. The lower iron abundance in stark white sandstone along the fault is also consistent with a fluid flow-driven alteration hypothesis, since acidic and/or reductive fluids could lead to dissolution and mobilization of iron. The relatively higher occurrence of sulfur in the purple-colored sandstone and the zoned spherical concretion (both from similar stratigraphic position) likely indicates the presence of iron sulfides (pyrite) or sulfate minerals (alunite or jarosite), consistent with thin section petrography and clay fraction XRD results (see below).

The iron abundances in the coloration and cementation facies likely relate to the diagenetic history of the sandstone, in particular with the dissolution, mobilization, and recrystallization of iron oxides in the various coloration and cementation facies. The low relative abundance of iron in the white-colored sandstone likely indicates that any pre-existing iron was stripped away during fluid-flow alteration of the formation, leading to progressively increasing concentration in the other coloration facies and cementation facies. Since no inverse correlation is apparent between aluminum and potassium in these samples, their presence and concentration

are likely due to the presence of kaolinite and illite/potassium feldspar, respectively.

XRD Observations and Interpretations

XRD analysis of sample clay fraction identified minerals related to the diagenetic facies of which they represent. Quartz and kaolinite were identified in all samples (Table 6), with coarse-grained kaolinite the dominant clay mineral. Most samples contain illite, and samples from near the Baseline fault (PS-6) and from near the white and red sandstone members transition (PS-11) contain trace amounts of interlayered illite/smectite. The powder sample PS-9 collected along the stratigraphic transect from the lower white contains chlorite and alunite. Sample PS-14 from the uppermost part of the red contains smectite.

The clay minerals identified in the powdered samples likely relate to Cretaceous paleosol processes and weathering on various timescales depending on the stratigraphic position, shallow burial of the formation, and possibly secondary alteration from fluid flow along the Baseline fault. The occurrence of kaolinite and illite in most samples suggests the possibility of surface weathering of muscovite mica and/or feldspar following deposition. It is possible that the occurrence of feldspar within the formation is related to weathering and very short transport distance of sediments derived from the Aztec Sandstone. Additionally, felspar may have been derived from air-fall tuff from eruptions from the Sierra Nevada Arc.

The occurrence of alunite, $KAl_3(SO_4)_2(OH)_6$, after mindat.org) and chlorite (likely either clinochlore, $Mg_5Al(AlSi_3O_{10})(OH)_8$, or chamosite, $(Fe^{2+},Mg,Al,Fe^{3+})_6(Si,Al)_4O_{10}(OH,O)_8$, after mindat.org) in the lower white sandstone member (sample PS-9) possibly suggest long-term weathering as part of the long-lived exposure of amalgamated channel, sandy alluvial plain environments within the fluvial system along the leading edge of the Sevier highlands (Reese, 1989; McNamara, 2010).

The occurrence of kaolinite along with the absence of dickite suggests that the formation was not buried deeply enough to transform the kaolinite to dickite, which typically occurs at about 110°C to 130°C (Ehrenberg et al., 1993). In the field area, the top of the Baseline Sandstone was likely buried to a minimum depth of about 400 m by the overlying Tertiary Rainbow Gardens Member of the Horse Spring Formation, Muddy Creek Formation, and Quaternary deposits (Muntean, 2013). Assuming a geothermal gradient range of 20° to 30°C and a total thickness of about 1100 m, the Baseline was likely exposed to temperatures between 28° to 65°C, well below the known temperature transformation (Figure 20). This is consistent with the estimated maximum burial depth of the underlying Aztec Sandstone as indicated by clay mineralogy (Eichhubl et al., 2004). The Tertiary deposits thicken from about 400 m at the Overton Ridge area to greater than 2000 m to the east of to the east of the Mobil Virgin River No. 1A well at Mormon Mesa (Bohannon et al., 1993), so maximum temperatures experienced by the Baseline were about 61° to 90°C (assuming about 2 km burial depth), still below the known temperature transformation (Figure 20). This temperature range is also below that of the typical thermal transformation temperature of FeOOH and ferrihydrite to hematite, and that of goethite to hematite (140° to 500°C, and 260° to 320°C, respectively; Cornell and Schwertmann, 2003).

Diagenetic Facies Distribution

This section includes additional observations of diagenetic facies occurrence and patterns in focus areas A and B (Figure 1C).

Focus Area A Diagenetic Patterns

Diagenetic patterns near Tearfault Mesa show a general relationship between diagenetic facies and depositional environment where the white sandstone member is finer-grained overall corresponding with a sheetflood-dominated alluvial fan environment (EOD D of Figure 12), with abundant concretionary facies exhibiting greater variability of forms, and higher intensity in coloration. Where the white sandstone is coarser-grained overall corresponding with a debris flow-dominated/channel-reworked alluvial fan environment (EOD E of Figure 12), concretionary facies are typically rarer and coloration facies are less varied and less concentrated (i.e., more diffuse in expression). The depositional environment remains the same with

the transition to the lower red sandstone member, with a slight change to more abundant carbonate concretionary forms, suggesting that the change in concretion mineralogy is not strictly tied to depositional environment.

Focus Area B Diagenetic Patterns

Carbonate concretions are restricted to the middle to upper red sandstone member along the stratigraphic transect. Small carbonate "grapestone" masses along joints occur near the large concretions (about 700 m above base) along with other crystalline calcite masses that appears to replace wood fragments. Large spheroidal/bulbous concretions occur in sandstone, whereas septarian concretions occur in the mudstone/siltstone. The only known occurrence of pipe-like concretions was identified in the uppermost about 25 m of the red.

Generally, there appears to be a relationship between depositional environment and diagenetic facies. In the lower white sandstone member where the depositional environment is that of a sandy braided alluvial plain, ironstone horizons are common along with various small iron oxide concretions. This part of the member is also where the iron oxide layer and massive with concentric ironstone horizon sub-forms occur. As the formation becomes coarser grained overall with the transition to the fluvial fan depositional environments (environments C, D, and E on the generalized stratigraphic column of Figure 13), concretionary forms and ironstone horizons are less abundant. Although the depositional environment remains largely the same at the white and red sandstone members boundary (Duncan, 2022), there is an overall decrease in grain size and an increase in the amount of silt and mud-sized grains shed from unroofing of the Triassic rocks contained within the hanging wall of the Willow Tank thrust. This is coincident with variability, variegation, and concentration of colors, along with an increase in concretion abundance. The somewhat abrupt change to monotone coloration and the cessation of iron oxide cementation facies does coincide with the shift in depositional environment back to a fluvial-dominated environment and overall decrease in grain size and change in overall architecture. However, the change seems to occur stratigraphically above the shift in depositional environment. The carbonate cementation coincides with the sandy isolated channel, alluvial plain depositional environment, where concretions show a preferred relationship to lithology with spheroidal/bulbous concretion forms occurring in the sandier sediments whereas the septarian concretions occur in mud/silt-sized sediments.

Satellite Mineral Mapping

Landsat multispectral satellite imagery is a tool to objectively evaluate mineral patterns and assess the validity of the observed qualitative patterns through field characterization, while showing continuity of larger-scale patterns. Landsat 8 Operational Land Imager (OLI) imagery covers spectral bands useful for identifying diagenetic minerals observed in the field (Figure A6). Simple threshold values applied to band-ratio raster images allow for the identification of various mineral products. Since these band ratios identify known mineral patterns (Figure 16B), they can be composited to derive mineral maps. Composite raster images were created using various combinations of band ratios (summarized in Table A2), with the best results obtained using the ratios after Abrams et al. (1983) having the 6/7, 5/6, and 4/2 ratio in the Red, Green, and Blue channels, respectively (Figure 16B).

Supervised and unsupervised classification of the composite raster validates the workflow and objectively reveals the distribution of diagenetic minerals, respectively. Each result is discussed further below. Supervised classification of the field area (Figure 16C) provides an intermediate check on the remote sensing workflow since the classification should classify similar pixels in the Landsat scene in similar groups if similarities exist. Unsupervised classification of the field area resulted in objective documentation of diagenetic patterns of the Baseline Sandstone and their relationships to the broad-scale stratigraphy and structures (Figure 16D).

Band Thresholding and Compositing

The threshold 4/2 ratio map identifies diagenetic mineral patterns associated with red coloration zones of the Aztec Sandstone and lower red sandstone member of the hanging wall block of the Baseline fault (red color on

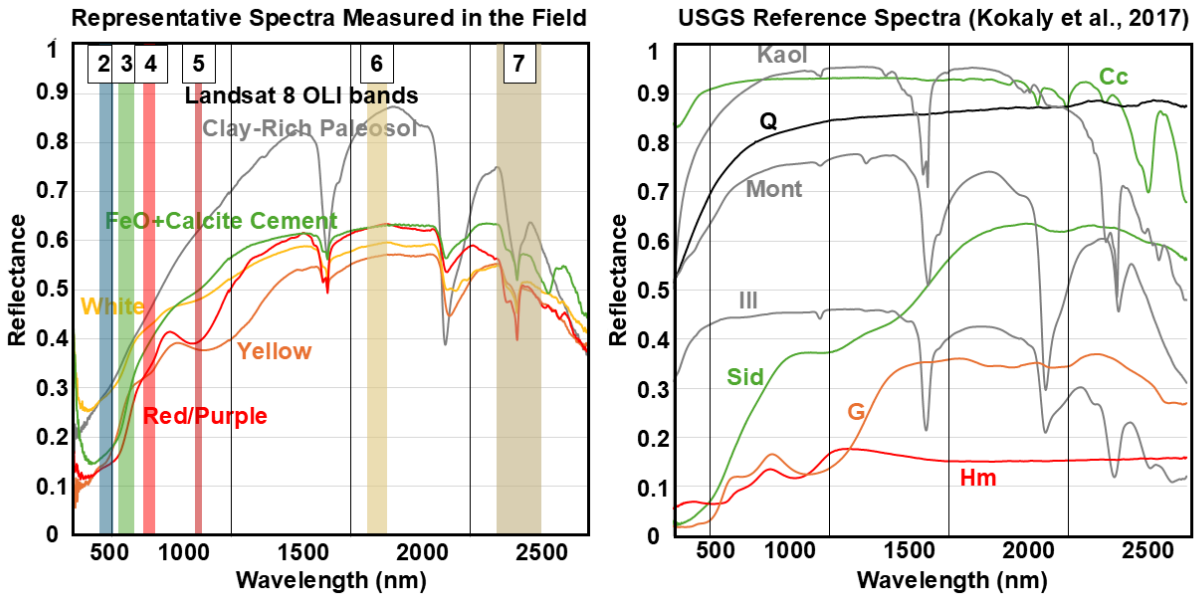

Figure A6. Visible-Near Infrared (VNIR) reflectance spectral profiles of rocks measured in the field area compared to representative reference spectra as measured in the lab. Numbered vertical bars indicate the band number and spectral range of Landsat 8 bands.

Figure 16A), resulting from the absorption feature in the long-visible/short-wave infrared. Some minor red coloration is also identified with this ratio in the red sandstone of the footwall block of the Baseline fault, although it is unclear whether the ratio is missing red-colored sandstone in that area due to soil cover. This threshold map also conforms to coloration patterns in the upper white sandstone member observed at the location of key outcrop 5 (Figure 1C) indicating goethite composition as revealed by reflectance spectroscopy, with lesser hematite coloration and concretionary forms at this location.

The threshold (4+6)/5 ratio map conforms more directly to ground-based observations. In particular, this band ratio highlights areas where iron oxide concretions (green color on Figure 16A) and bedding-parallel mineral cemented zones are present in the white sandstone member (focus areas A and B of Figures 1C and 16D). The close relationship between the threshold map and ground-based observations indicates that this threshold map can be used for identifying and mapping iron oxide concretion occurrences remotely, at least to a first order.

The threshold 6/7 ratio map reflects ground-based patterns of bleached/altered zones in the Aztec Sandstone, and color patterns of the white sandstone member (light blue color on Figure 16A). The threshold 5/6 ratio map highlights known clay-rich areas both in the middle stratigraphic part of the Willow Tank Formation and in soils/Quaternary alluvium around Baseline Mesa and the Simplot Mine/Kaolin Wash (teal coloration on Figure 16A).

To a first-order, the threshold maps identify known patterns in diagenetic iron oxide and clay minerals, indicating that combinations of these band ratios can be used in image composites to more accurately differentiate between coloration and concretion patterns (Figure A7). In the end, the band ratio combination after Abrams et al. (1983) was selected (Figure 16B) as the best representation of known diagenetic patterns and were successfully used for further classified mineral maps through supervised and unsupervised classification schemes (Figures 16C and 16D).

Classified Mineral Maps

Supervised classification: Supervised classification of the field area (Figures 16C and A8) provides an inter-

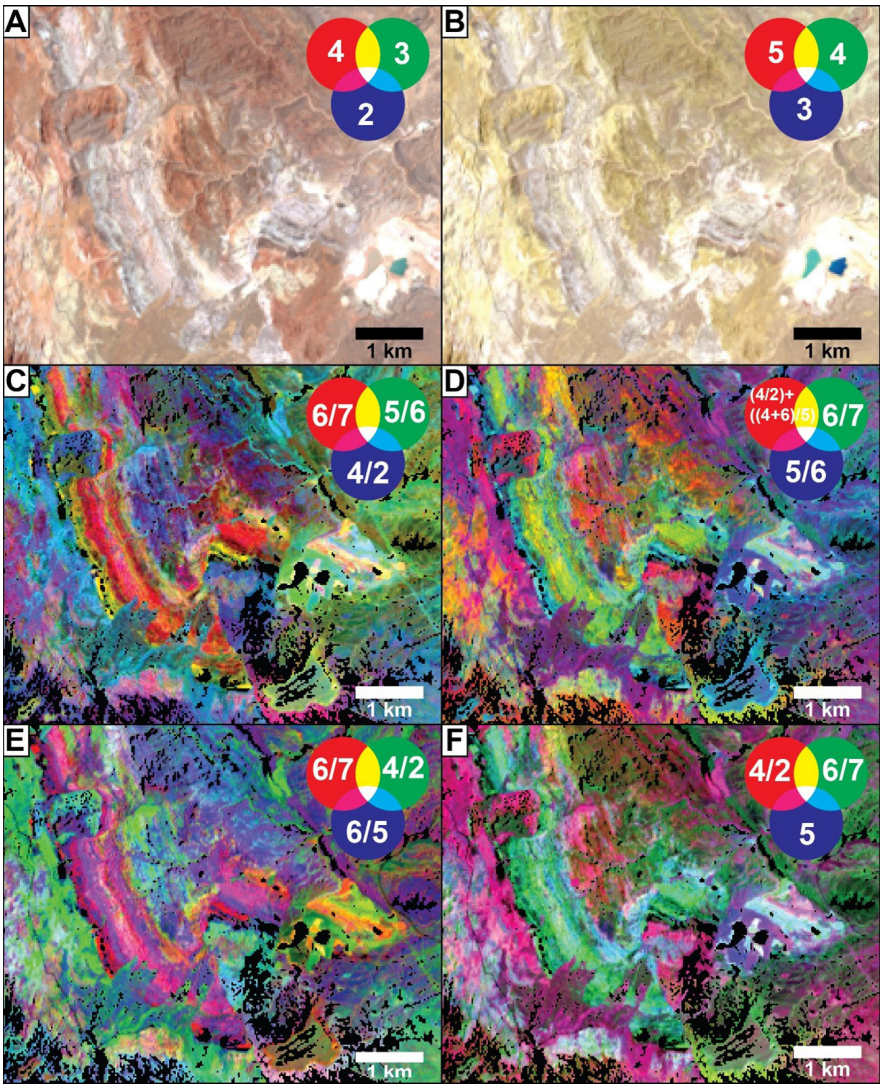

Figure A7. Composite images derived from various bands and band ratios. Diagram in upper right of each image indicates the band or band ratio used in each Red, Green, or Blue channels (RGB, as indicated by the corresponding Red, Green, or Blue circles). Color of each pixel then indicates relative strength of the particular band/band-ratio, or mixes of bands/band-ratios. (A) Standard RGB composite. (B) Color-infrared composite. (C through F) Composites of band ratios and compound band ratios.

mediate check on the remote sensing workflow since the classification should classify similar pixels in the Landsat scene in similar groups if similarities exist. However, this classification might not work best for objective pattern identification for three main reasons. First, this method is greatly dependent on the training samples selected and the number of samples used. Second, this method does not utilize masking, meaning that shaded pixels or pixels of vegetation/water are included in the resultant classification. Third, due to the moderate spatial resolution of the Landsat imagery, each pixel in the Landsat scene represents a mix of various spectral signatures (at 30 m/pixel resolution). Several observations from the classified image are interesting and validate this point.

Areas designated as training classes for this classification are shown in Figure A2. Similarities in the white sandstone member on either side of the Baseline fault, classified as "Bleached" (Baseline), align with field-based observations that indicate similarities in the white sandstone member throughout the field area. This classification also shows a difference between the red sandstone member on either side of the Baseline fault with that in the hanging wall classified as a combination of "Bleached Aztec," "FeO+Calcite," "FeO-Rich," "Anthropogenic," and "Soil 2", and that in the footwall classified as "FeO-Rich," minor "FeO+Calcite," and predominance of "Soil 1" and "Soil 2" in the upper red sandstone. In addition, the "Anthropogenic" class matches the active Simplot Mine (where silica-rich sand is being exposed) as well as the abandoned Florence Mine. However, this class occurs in other areas that are more accurately classified as intensely altered/bleached

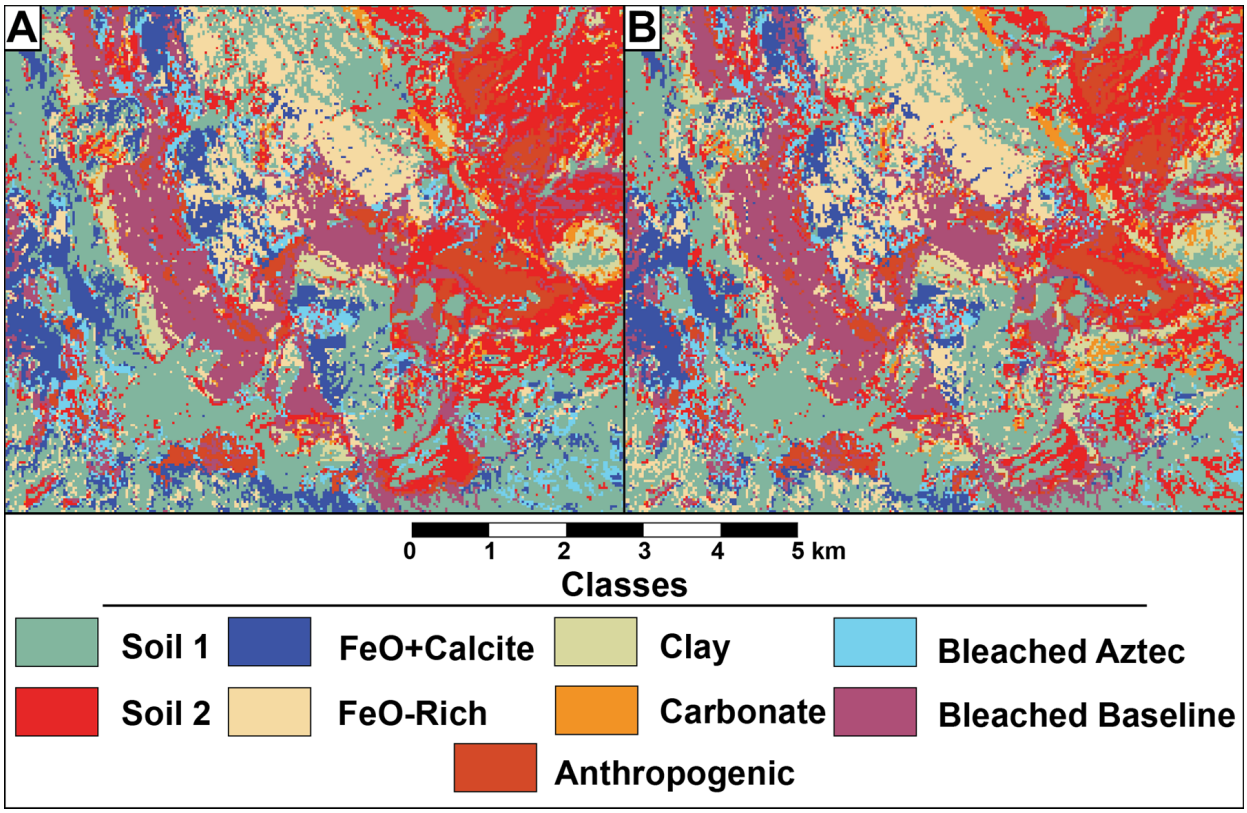

Figure A8. Supervised classification images using both the Abrams (A) and custom band combination (B).

(e.g., the rocks in proximity to the Baseline fault) or as soil cover (e.g., patches throughout the white sandstone member).

Unsupervised classification: Unsupervised classification of the field area resulted in objective documentation of diagenetic patterns of the Baseline Sandstone and their relationships to the broad-scale stratigraphy and structures (Figures 16D and A9). Patterns in classes derived through this classification align with the known diagenetic mineral patterns in the diagenetic pattern focus areas, thus validating this approach and providing additional observations of the pattern distribution and orientation away from the field-characterized area. Since this classification was unguided/uninfluenced from training samples and used masking, the results are determined through the relative strength of spectra reflected in each combined pixel and are therefore objective.

The white sandstone member patterns appear to align with the ground-based observations since clear stratigraphic patterns in diagenetic mineralogies emerge. The lowermost white sandstone member in both the hanging wall and footwall of the Baseline fault display a mix of class 2 and 4 that parallel the stratigraphy and coincide with known occurrences of concretionary forms and ironstone horizons (Figure A9). In the hanging wall block, the red coloration-dominated zone coincides with class 11, which does not continue laterally through to the footwall block and instead transitions to predominately class 2 (Figure A10). The upper white patterns match known diagenetic attributes and exhibit similar relationships throughout the rest of the white sandstone member. Coloration facies-dominated parts seem to coincide with class 2 and class 3, and the occurrence of concretionary forms coincides with the addition of class 4.

The uppermost white sandstone member to lowermost red sandstone member change to dominance of class 4 with addition of class 7. The hanging wall block part of the uppermost white and lowermost red exhibits a dominance of class 6, where known cementation facies are composed of red-colored carbonate concre-

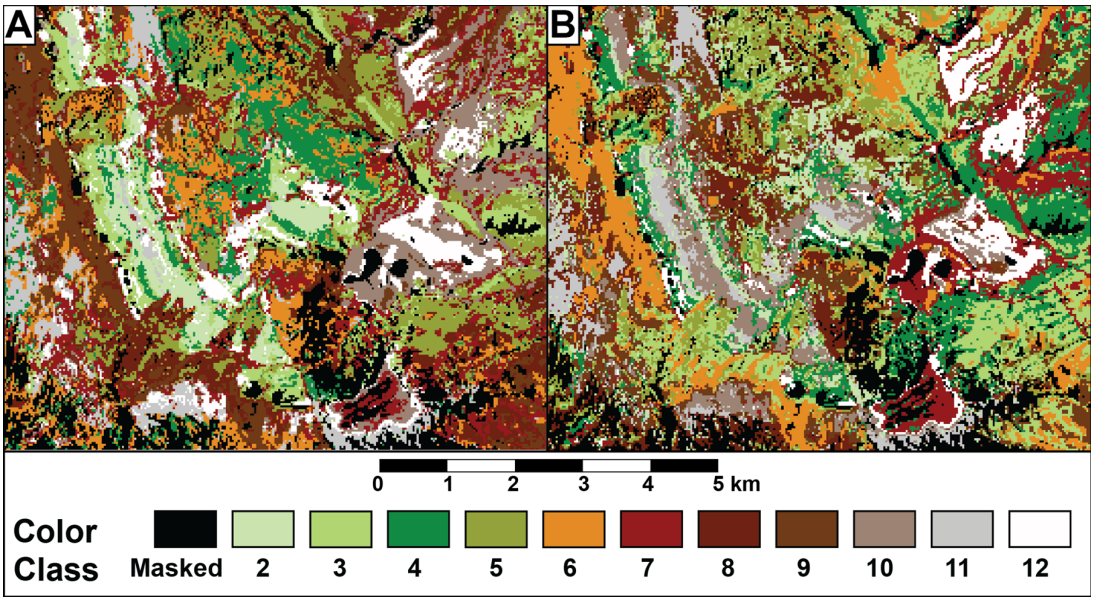

Figure A9. Unsupervised classification derived from the (A) Abrams, or (B) custom band ratios.

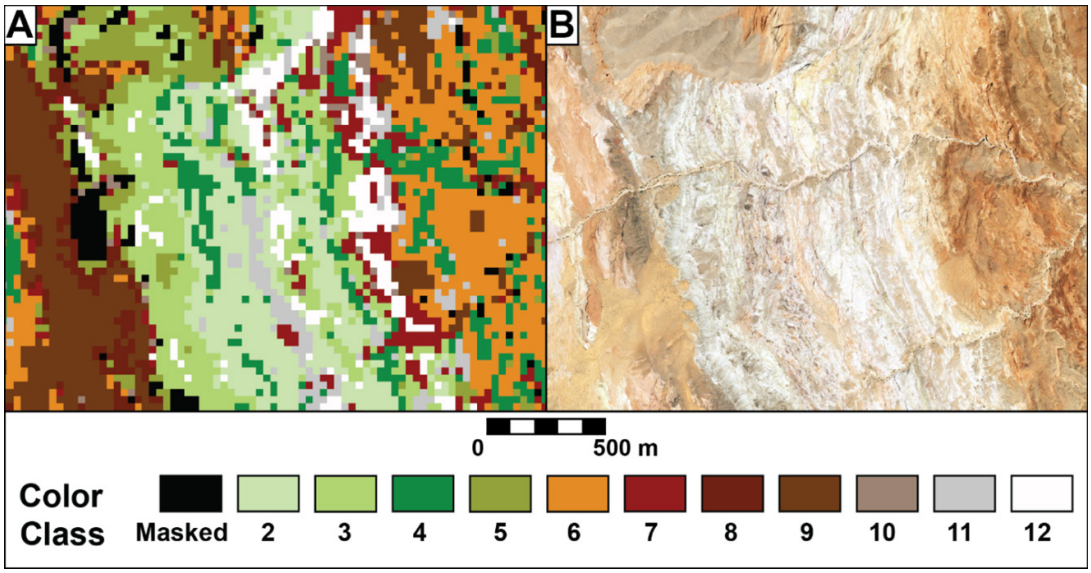

Figure A10. Detailed view of the unsupervised classification of the white sandstone through lower red sandstone members of diagenetic pattern focus area A.

tion forms. In contrast, the lower half of the red in the footwall block is dominated by class 4 with increasing amounts of class 6 up section in an area where concretionary forms are predominately iron oxide with minor carbonate concretions and later joint mineralization. The upper half of the red in the footwall block is dominated by classes 5, 8, and 9, with minor amounts of class 4 (Figure A11). This pattern is consistent with the relatively higher amount of Quaternary soil cover and increased amount of carbonate concretionary forms mixed along with the higher amount of floodplain preserved in this part of the stratigraphy. Overton Ridge, which is made up of the resistant limestone clast-dominated conglomerate of the Rainbow Gardens Member of the Horse Spring Formation (Figure 1C), curiously is classified mainly as class 3, similar to the fine-grained interval of the Willow Tank Formation.

Patterns adjacent to the Baseline fault are not as clearly relatable to ground-based observations as other areas (Figure A12). White pixels of class 12 seem to coincide with the stark white and bleached sandstone of the white sandstone member adjacent to the calcite concretion-bearing Aztec Sandstone, which is placed in class 6, similar to other calcite-cemented materials. The spectral mapping of class 12 coincides with the incision block from the white and other areas of altered white sandstone member north-

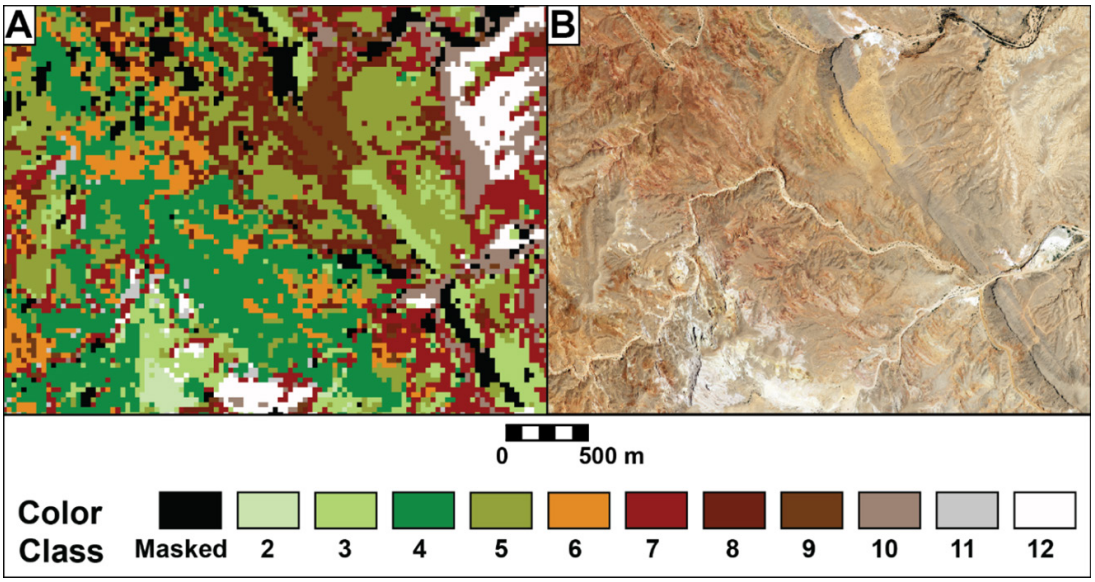

Figure A11. Detailed view of the unsupervised classification (A) of the red sandstone member in (B) a part of diagenetic pattern focus area B.

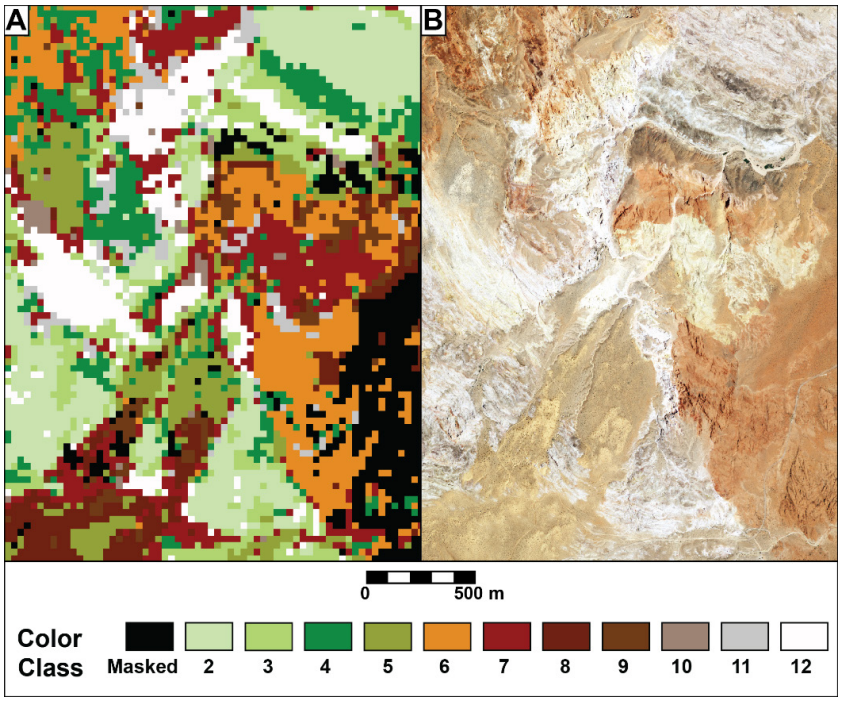

Figure A12. Detailed view of the unsupervised classification map (A) of the Baseline fault in the southern part of the field area (B).

ward along the trace of the fault. However, aside from the incised block, the rest of the pixels classified as class 12 may coincide with other examples of class 12 in the upper white and may be a repetition of the same stratigraphic interval from faulting. Another inaccuracy of this mapping is shown by the similar grouping of different units of the Aztec (the upper red and banded red and white unit, along with the lower red unit of Eichubbl et al., 2004). However, there is a slight difference between the two, as the upper red unit is a mix of classes 6, 7, and 9, and the lower red unit is predominately class 6 with minor class 4.

Similar to the band threshold images, iron oxide concretion forms seem to be highlighted by class 4. With the increasing abundance of carbonate concretion forms, the pixels appear to mix increasingly with those classified as class 6.

It is important to note that each class represents the relative dominance of particular spectral signatures related to the prevailing surface material in any given pixel of the Landsat scene. An opportunity exists for future characterization of each pixel through Principal Component Analysis (PCA) to further refine methodologies and extract additional information. However, sufficient conclusions to support the present research questions can be gained from qualitative exploration of the unsupervised classified map.

Satellite mapping interpretation: From the unsupervised classification map (Figure 16D), several significant observations about the spectral signatures of the ground surface materials, as well as the relative timing of their formation, can be inferred. The change in classes from the white to the red sandstone member likely relates to the stratigraphic patterns and change in depositional environment to one that includes a higher proportion of fine-grained overbank material and change to calcite cement. The coloration patterns observed on the ground in proximity to the Baseline fault seem to parallel the fault and are likely related to a Miocene-aged (or younger) timing. This remote-sensing mapping shows, objectively, that the patterns of diagenetic coloration or cementation facies parallel stratigraphy and are deformed/cross-cut in the same way from later folding (Laramide-aged Kingman arch) and faulting (Baseline fault and other Miocene-aged normal faults). These cross-cutting relationships indicate that the primary coloration and cementation facies formed before at least Laramide time.

APPENDIX REFERENCES

Abrams, M.L., Brown, D., Lepley, L., and Sadowski, R., 1983, Remote sensing for porphyry copper deposits in southern Arizona: Economic Geology, v. 78, 591–604.

Bohannon, R.G., Grow, J.A., Miller, J.J., and Blank, R.H., Jr., 1993, Seismic stratigraphy and tectonic development of Virgin River depression and associated basins, southeastern Nevada and northwestern Arizona: Geological Society of America Bulletin, v. 105, p. 501–520.

Cornell, R.M., and Schwertmann, U., 2003, The iron oxides—structure, properties, reactions, occurrences and uses, 2nd edition: Weinheim, Germany, Wiley-VCH, 664 p.

Ducart, D.F., Silva, A.M., Toledo, C.L.B., and de Assis, L.M, 2016, Mapping iron oxides with Landsat-8/OLI and EO-1/Hyperion imagery from the Serra Norte iron deposits in the Carjas Mineral Province, Brazil: Brazilian Journal of Geology, v. 46, no. 3, p. 331–349, https://doi.org/10.1590/2317-4889201620160023.

Duncan, C.J., 2022, Stratigraphic, structural, and biologic controls on iron oxide diagenesis of the Cretaceous Baseline Sandstone, southern Nevada: Salt Lake City, University of Utah, Ph.D. dissertation, 456 p.

Ehrenberg, S.N., Aagaard, P., Wilson, M.J., Fraser, A.R., and Duthie, D.M.L., 1993, Depth-dependent transformation of kaolinite to dickite in sandstones of the Norwegian continental shelf: Clay Minerals, v. 28, no. 3, p. 325–352, https://doi.org/10.1180/claymin.1993.028.3.01.

Eichhubl, P., Taylor, W.L., Pollard, D.D., and Aydin, A., 2004, Paleo-fluid flow and deformation in the Aztec Sandstone at the Valley of Fire, Nevada—evidence for the coupling of hydrogeologic, diagenetic, and tectonic processes: Geological Society of America Bulletin, v. 116, no. 9/10, p. 1120–1136, https://doi.org/10.1130/B25446.1.

Gaffey, S.J., 1986, Spectral reflectance of carbonate minerals in the visible and near infrared (0.35-2.55 microns)—calcite, aragonite, and dolomite: American Mineralogist, v. 71, p. 151–162.

Kokaly, R.F., Clark, R.N., Swayze, G.A., Livo, K.E., Hoefen, T.M., Pearson, N.C., Wise, R.A., Benzel, W.M., Lowers, H.A., Driscoll, R.L., and Klein, A.J., 2017, USGS Spectral Library Version 7: U.S. Geological Survey Data Series 1035, 61 p., https://doi.org/10.3133/ds1035.

McKeown, N.K., Bishop, J.L., Cuadros, J., Hillier, S., Amador, E., Makarewicz, H.D., Parente, M., and Silver, E.A., 2011, Interpretation of reflectance spectra of clay mineral-silica mixtures—implications for Martian clay mineralogy at Mawrth Vallis: Clay and Clay Minerals, v. 59, no. 4, p. 400–415, https://doi.org/10.1346/CCMN.2011.0590404.

Muntean, T.W., 2013, Preliminary geologic map of the Valley of Fire East quadrangle, Clark County, Nevada: Nevada Bureau of Mines and Geology Open-File Report 13-6, scale 1:24,000.

Pour, A.B., and Hashim, M., 2015, Hydrothermal alteration mapping from Landsat-8 data, Sar Cheshmeh copper mining district, south-eastern Islamic Republic of Iran: Journal of Taibah University for Science, v. 9, p. 155–166, https://doi.org/10.1016/j.jtusci.2014.11.008.

Roy, D.P., Wulder, M.A., Loveland, T.R., Woodcock, C.E., Allen, R.G., Anderson, M.C., Helder, D., Irons, J.R., Johnson, D.M., Kennedy, R., Scambos, T.A., Schaaf, C.B., Schott, J.R., Sheng, Y., Vermote, E.F., Belward, A.S., Bindschadler, R., Cohen, W.B., Gao, F., Hipple, J.D., Hostert, P., Huntington, J., Justice, C.O., Kilic, A., Kovalskyy, V., Lee, Z.P., Lymburner, L., Masek, J.G., McCorkel, J., Shuai, Y., Trezza, R., Vogelmann, J., Wynne, R.H., and Zhu, Z., 2014, Landsat-8—science and product vision for terrestrial global change research: Remote Sensing of Environment, v. 145, p. 154–172, http://dx.doi.org/10.1016/j.rse.2014.02.001

Sabins, F.F., 1999, Remote sensing for mineral exploration: Ore Geology Reviews, v. 14, p. 157–183, https://doi.org/10.1016/S0169-1368(99)00007-4.

Simpson, M.P., and Rae, A.J., 2018, Short-wave infrared (SWIR) reflectance spectrometric characterization of clays from geothermal systems of the Taupō Volcanic Zone, New Zealand: Geothermics, v. 73, p. 74–90, https://doi.org/10.1016/j.geothermics.2018.01.006.

Tidwell, W.D., and Hebbert, N., 1992, Species of the Cretaceous tree fern *Tempskya* from Utah: International Journal of Plant Science, v. 153, no. 3, p. 513–528.

Ulmer-Scholle, D.S., Scholle, P.A., Schieber, J., and Raine, R.J., 2016, A color guide to the petrography of sandstones, siltstones, shales, and associated rocks: American Association of Petroleum Geologists Memoir 109, 526 p.